Monitoring Micro-Damage Accumulation Based on Reduction in Elastic Properties Using Fiber Bragg Grating Sensors, and Acoustic Emission and Thermography Methods in Fiber Reinforced Polymeric Composites

by

Çağatay Yılmaz

Submitted to
the Graduate School of Engineering and Natural Sciences
in partial fulfillment of the requirements for the degree of
Doctor of Philosophy

SABANCI UNIVERSITY

July 2018

APPROVED BY:

Mehmet Yıldız .....

(Thesis Supervisor)

Afzal Suleman .....

Bahattin Koç .....

Halit Türkmen .....

Yusuf Menceloğlu .....

DATE OF APPROVAL: .....

"The mystery of life is not a problem to be solved but a reality to be experienced.."

Art Van Der Leeuw

Monitoring Micro-Damage Accumulation Based on Reduction in Elastic Properties Using Fiber Bragg Grating Sensors, and Acoustic Emission and Thermography Methods in Fiber Reinforced Polymeric Composites

Çağatay Yılmaz

Ph.D. Dissertation, July 2018

Thesis Supervisor: Prof. Dr. Mehmet Yıldız

Keywords: laminated composite, damage accumulation, damage index, non-destructive evaluation

Abstract

Laminated Composite Structures (LCS) have been used increasingly in recent years in engineering applications such as aircraft and shipbuilding. However, it is important to note that despite the constant increase in the usage of LCSs, a number of certain aspects need to be investigated in detail. These aspects can be summarized in two different topics: the effect of different micro-damage types on LCSs and novel test methods for the measurement of certain mechanical properties. Here, to touch on these two issues, we investigate micro-damage accumulation and its effects on elastic constants of the laminated composite as well as we introduce a Finite Element Analysis (FEA) of a possible test method to calculate certain mechanical properties of thin-laminated composites.

Unlike metals, LCSs can develop different types of micro-damage under load. These different types of micro-damage play a critical role in the failure of LCSs. Once initiation and accumulation of different types of micro-damage are understood, an adequate understanding of LCSs under operational loads can be established. This understanding results in the prediction of possible failure time of LCSs and usage of a number of elastic constants as a micro-damage monitoring index. For that purpose, we present an experimental study on the monitoring of the reduction in Poisson's ratio coupled with micro-damage initiation and accumulation. Poisson's ratio is monitored with a novel an embedded-biaxial Fiber Bragg Grating (FBG) sensor during the static tensile test of composite coupons. Accumulation of different types of micro-damage are monitored with Acoustic Emission (AE) set-up. It is seen that as Poisson's ratio reduces under tensile loading, composite coupons emit a higher number of acoustic waves due to the micro-damage formation.

It is also demonstrated that reduction in in-plane shear modulus under in-plane shear loading is due to micro-damage accumulation. For this purpose, two different fiber reinforcement, S-glass and E-glass, are chosen to produce laminated

composites. The total amount of micro-damage incurred as well as the average temperature change measured by thermography are higher for the E-glass reinforced LCS. Under the applied in-plane shear load, a significant reduction in in-plane shear modulus is observed both for the E-glass and S-glass-reinforced LCS, where the E-glass reinforced LCS shows a greater reduction.

In addition, a FEA of Lamb wave propagation in thin-laminated composites is also performed. The performed FEA is a numerical simulation of a novel, non-time-consuming, non-destructive evaluation method for thin-laminated composite structures to calculate the components of stiffness matrix and laminate elastic properties. For that purpose, the group velocities of $A0$ and $S0$ modes of Lamb wave are measured on a transversely isotropic thin-laminate. Then, these group velocities are used in Christoffel's equation to calculate the components of stiffness matrix. In turn, the components of stiffness matrix are used in an inverse formulation to calculate thin-laminate elastic constants.

Fiber Takviyeli Polimerik Kompozitlerde Fiber Bragg Izgara Sensörleri, Akustik Yayılım ve Termografi Yöntemleri Kullanılarak Mikro-Hasar Birikiminin Elastik Özelliklerdeki Azalmaya Dayalı Olarak İzlenmesi

Çağatay Yılmaz

Ph.D Tezi, Temmuz 2018

Tez Danışmanı: Prof. Dr. Mehmet Yıldız

Anahtar Kelimeler: kompozit, mikro hasar, Poisson oranı, Lamb dalgası

Özet

Lamine Kompozit Yapılar (LKY) son yıllarda uçak ve gemi inşaatı gibi mühendislik uygulamalarında giderek daha fazla kullanılmaktadır. Bununla birlikte, LKY kullanımındaki sürekli artşa rağmen, birtakım özelliklerin ayrıntılı olarak araştırılması gerektiği unutulmamalıdır. Bu özellıkler iki ayrı konuda özetlenebilir: farklı mikro-hasar tiplerinin LKY'lere etkisi ve bazı mekanik özelliklerin ölçümü için yeni test yöntemlerininin geliştirilmesi. Burada bu iki konu, mikro-hasar birikiminin ve bu mikro-hasar birikiminin LKY'nin elastik sabitleri üzerindeki etkisi araştırılarak ve ayrıca ince tabakalı kompozitlerin belirli mekanik özelliklerini hesaplamak için yeni bir test yönteminin Sonlu Elemanlar Analizi (SEA) yapılarak işlenmiştir.

Metallardenden farklı olarak LKY'ler yük altında farklı mikro-hasar türleri geliştirebilir. Bu mikro hasar türleri LKY'lerin hasara uğrayıp kullanım dışı kalmasında kritik bir rol oynamaktadırlar. Farklı mikro hasar türlerinin ilk oluşumu ve birikmesi anlaşıldıktan sonra, operasyonel yükler altında LKY'lerin davranışı detaylı bir şekilde anlaşılabilir. Bu anlayışla beraber LKY'lerin muhtemel işlev dışı kalma süresinin tahmin edilmesine ve bazı esneklik sabitlerinin mikro hasar gösterge katsayısı olarak kullanılmasının yolu açılabilir. Bu amaçla, mikro-hasar başlaması ve birikmesiyle beraber Poisson oranı azalışının mikro-hasar birikim göstergesi olarak kullanılması üzerine deneysel bir çalışma sunulmuştur. Poisson oranının azalması, bu çalışma sırasında geliştirilmiş ve LKY'ya üretim sırasında gömülmüş, çift eksenli fiber Bragg ızgara (FBG) sensörler ile statik çekme testi sırasında izlenmiştir. Buna ek olarak, farklı mikro hasar türlerinin birikimi, Akustik Yayılım (AY) düzeneği ile izlenmiştir. Çekme yükü altnda Poisson oranı düştükçe, LKY'ler tarafından yayılan Akustik dalgalar artan mikro-hasar oluşumundan dolayı artış göstermiştir.

Yine düzlemsel kayma yükü altında düzlemsel kayma modülündeki azalmanın, mikro hasar birikimine bağlı olduğu gösterilmiştir. Bu amaçla, iki farklı fiber takviye, S-cam ve E-cam, LKY üretmek için seçilmiştir. Biriken toplam mikro-hasar miktarı ve termografi ile ölçülen ortalama sıcaklık değişimi E-cam takviyeli

LKY için daha yüksektir. Uygulanan düzlemsel kayma yükü altında, düzlemsel kayma modülü E-cam ve S-cam takviyeli LKY'nin ikisinde de önemli oranda düşüş göstersede, E-cam takviyeli LKY için bu düşüşün S-cam takviyeli LKY'ye göre daha yüksek olduğu gözlemlenmiştir.

Bunlara ek olarak, ince lamineli kompozitlerde Lamb dalgası yayılımı SEA ile gerçekleştirilmiştir. Gerçekleştirilen SEA, ince LKY için yeni, zaman alıcı olmayan, rijitlik matrisi bileşenlerini ve esneklik özelliklerini hesaplamak için kullanılabilecek tahribatsız bir test yönteminin hesaplamalı sayısal analizidir.Bu amaçla, Lamb dalgasının $A0$ ve $S0$ modlarının grup hızları, yanal izotropik simetreye sahip bir ince LKY üzerinde ölçülmüştür. Sonra, bu grup hızları Christoffel denkleminde kullanılan LKY'nin rijitlik matrisinin bileşenlerini hesaplamak için kullanılmıştır. Daha sonra ise, hesaplanan rijitlik matrisinin bileşenleri tersine denklemler içinde kullanılarak aynı ince LKY'nin esneklik sabitleri hesaplanmştır.

Acknowledgements

I would like to thank **Professor Mehmet Yıldız** as my advisor and his continuous support during the course of my studies in the Sabanci University. I am indebted to **Professor Mehmet Yıldız** for the valuable advice and guidance on the formation of this thesis.

I would like to thank **Professor Afzal Suleman** giving me an opportunity to complete my research in his laboratory, Center for Aerospace Research (CFAR), in the University of Victoria.

My reading committee members, Professors **Bahattin Koç**, **Yusuf Menceloğlu**, **Halit Türkmen**, for their helpful comments on the draft of this thesis.

I would like to gratefully acknowledge the funding provided by The Scientific and Technological Research Council of Turkey TÜBİTAK, and The Ministry of Science, Industry and Technology:

- Project Code 112M357: Monitoring Fatigue Behavior and Life of Fiber Reinforced Polymeric Composite Materials by Fiber Bragg Grating Sensors.
- Project Code 01307.STZ.2012-1:Development of Innovative Multi Axis Laminated Composites and Experimental & Numerical Analysis
- TÜBİTAK 22214-A International Research Fellowship Program for PhD Students.

I would like to thank many colleagues in the İleri Kompozit Malzemeler ve Polimer İşleme Laboratuvarı . Thanks a lot for all their helps in experiments, discussions, and friendship during the course of my PhD

My friends at Sabancı University

My brother Furkan Yılmaz and **My father** Önder Yılmaz

My family for their unending sport from the beginning of my life.

To all of you, Thank you!

Çağatay Yılmaz

Contents

List of Figures

List of Tables

Abbreviations

LCS	**L**aminated **C**omposite **S**tructure
FEM	**F**inite **E**lement **M**odel
FEA	**F**inite **E**lement **A**nalysis
WPF	**W**eighted **P**eak **F**requency
PP2	**P**artial **P**ower **T**wo

Physical Constants

Young's modulus of E-glass	E_E	=	72.3 GPa
Young's modulus of S-glass	E_S	=	87 GPa
The coefficient of thermal expansion of E-glass	α_E	=	54
The coefficient of thermal expansion of S-glass	α_S	=	16

Symbols

E_1	young modulus in the direction of 1	GPa
E_2	young modulus in the direction of 2	GPa
E_3	young modulus in the direction of 3	GPa
ϵ_1	strain in the direction of 1	
ϵ_2	strain in the direction of 2	
ϵ_3	strain in the direction of 3	
ν_{12}	Poisson's ratio $(-\epsilon_2/\epsilon_1)$	
ν_{13}	Poisson's ratio $(-\epsilon_3/\epsilon_1)$	
ν_{23}	Poisson's ratio $(-\epsilon_3/\epsilon_2)$	

To my grandmother Sultan and my grandfather Kahraman. . .

Chapter 1

Introduction

1.1 Motivation

Due to lightweight, high special strength and stiffness properties, Laminated Composites Structures (LCSs) find themselves a place in a number of applications. These applications include storage tanks, bridge parts, hockey sticks, baseball bats, airplanes, boats, and cars. Airplanes, boats, and cars have great significance for composite among these applications. Recently, German car manufacturer, BMW, has unveiled an electric car, BMW i3, and a hybrid car, BMW i8. The predominant materials for the body of these two types of cars are composite. The usage of composite compensates the weight of battery packs, and hence enable cars to travel greater distances. In addition, composite also leads to cars create fewer greenhouse gases.

In addition to cars, a certain number of boats and ships are also manufactured using composite. For instance, Yonca-Onuk shipyard offers dozens of military and commercial boats which are completely made from composite. Composite eliminates the corrosion issue for boats, as well as provides higher speed (than metallic boats) due to the reduction in total weight.

Boeing has recently increased the percentage of composite usage from 1% to 11%, and to 50% in its 747, 777, and 787 models, respectively. Boeing 787 is the first commercial airplane that uses composite as a primary structural material rather than metal. As the competition increases between airplanes manufacturer due to costumer-driven needs, Airbus has also unveiled a new model, A350, which is

composed of 52% composite. In addition to the commercial airplane, composite finds a place for itself in military aircraft. For instance, Lockheed F-22 and F-35 have in total 40% and 42% composite, respectively. The usage of composite reduces the total weight of both commercial and military airplanes and hence increases the total payload. This increase in payload results in more passenger or ammunition, as well as provide longer distances with the same amount of fuel. Not being limited to the payload, composite provides fewer scheduled maintenance time due to its non-corrosive structure compared to aluminum and steel for airplanes.

As the usage of Laminated Composite Structures (LCSs) increases in engineering applications, such as cars, airplanes, and boats, their characterization with destructive and non-destructive methods become more important than ever. This characterization involves many aspects such as failure behaviors, micro-damage evolution, measurement of elastic constant, and health monitoring. Although each of these aspects is the subjects of the research for metals, ceramics, and polymers for decades, little has been done so far for LCSs. For instance, thousands of hours of flying causes to micro-damage accumulation due to dynamic loads on airplanes. This micro-damage propagates and coalesces, hence creates macro-damage. Macro-damage can cause abrupt failure of the airplane, unless necessary precautions are taken. The reliability of airplanes can only be ensured if they are periodically inspected. If there is a damaged part, it needs to be replaced with a sound one.

Non-destructive evaluation methods, such as tap testing, x-ray, ultrasound, and thermography provides relatively easy maintenance for periodical inspection. Periodical inspection is a preventive maintenance which needs to be completed based on time or the number of flights for an airplane. It maintains the safety of airplanes, while brings operational cost due to its labor-intensive process. Sometimes, the whole structure may need to be disassembled in order to check certain parts. If the certain parts are found undamaged, it is waste of time, labor, and money. The reassembly of the whole structure might be also challenging. The periodical inspections can also cause accidental damages during the reassembly or repairing. For instance, according to International Aviation Safety Assessment (IASA) and Aviation Safety Network (ASN), the falling of China Airlines Flight 611 and Japan Airlines Flight 123 was due to improper repairing and reassembling of airplanes during the periodical inspections. In these two incidences, a total of 745 people have died.

In addition to preventive maintenance, airplanes can benefit from predictive maintenance. Predictive maintenance is a continues monitoring of the condition of the critical structural parts. Predictive maintenance is a Condition Based Maintenance (CBM) approach, which leads to the repair of the part when it is needed, hence it eliminates the drawbacks of preventive maintenance. Predictive maintenance contains a certain number of approaches and one of this approaches is Structural Health Monitoring (SHM). SHM uses embedded or attached sensors to the certain parts of the airplane to real-time condition monitoring of the parts. One of the strong candidates to monitor the condition of the parts is fiber Bragg grating (FBG) sensor. FBG sensors allow us to measure temperature and strain and can be attached or embedded the composite parts. Once it is embedded, it becomes the part of the composite structure and senses the local strains. These local strain can be used with a certain number of approaches to monitor the condition of the critical part.

Another critical issue for maintaining the safety of a composite airplane as well as composite car and boat is the understanding of the micro-damage initiation and accumulation. Micro-damage can leads to macro-damage by propagating and coalescing. A true understanding of micro-damage initiation and accumulation under the dynamic or static loads with Acoustic Emission (AE) method provides critical information on the evolution of micro-damage and possible failure time of the composite parts.

Another issue for composite made vehicles is its development cost. Development cost includes the 3-D design of the vehicle, an appropriate composite choice for certain parts and stress analysis of the 3-D model. Although 3-D design and stress analysis are computer-based works, choice of appropriate composite for the certain parts requires a number of experimental work to measure mechanical properties of the composite. Due to anisotropic nature of composite, carefully machined composite coupons need to be tested in different symmetry directions with different test fixtures and strain gauges. These tests can take months and cost a significant amount of resource based on the size and complexity of the vehicle.

In light of the above discussions, the motivation behind this work is to understand micro-damage initiation, accumulation, monitoring of micro-damage accumulation with embedded FBG sensor, and development of an inexpensive test method to measure mechanical properties for glass fiber reinforced laminated composite. In regard to the motivation, within the scope of the current Ph.D. study, three goals

were set. The first one is the usage of Poisson's ratio, monitored by embedded novel biaxial FBG sensor, as a damage index. The second one is to investigate the effect of the micro-damage initiation and accumulation on the reduction in Poisson's ratio and in-plane shear modulus by means of Acoustic Emission and Thermography. The third goal is to develop an inexpensive test method to measure stiffness matrix and elastic constants. Toward this end, these goals do not immediately aim to commercialize or solve the above-mentioned problems; on the contrary, project's target is to discuss possible solutions and develop know-how. In conclusion, these goals are hoped to open possibilities for decreasing the intervals of periodic inspection and reducing development costs.

1.2 Outline of Thesis

The rest of thesis is developed as follows. Chapter 2 briefly summarizes the LCSs, terms, and tools used in this study. In Chapter 3, a detailed procedure of the embedding of biaxial FBG sensor and its usage to monitor the condition of Poisson's ratio are presented. In Chapter 4, the micro-damage accumulation with AE and its relation with the reduction in Poisson's ratio are given. Chapter 5 evaluates the reduction in in-plane shear modulus as a result of micro-damage accumulation by applying the AE and thermography methods. In chapter 6, an FEA of a possible test method to inexpensively measure a number of mechanical properties of LCSs are presented. The present work concludes with a discussion of future studies, in the modeling of the reduction in elastic laminate constants and inexpensive measurement of the mechanical properties of LCSs, in Chapter 7.

Chapter 2

Background

2.1 Introduction

This chapter provides a reader with relatively comprehensive information on the damage types develop under load, micro-damage monitoring, micro-damage detection, sensors to benefit, and signal processing for laminated composites.

2.2 A Brief Summary of Laminated Composites Structures

The new structure, which is formed by combining at least two different components with physical methods, is called composite. A composite shows completely different physical properties than its constituent components. These differences are generally positive and compensate for the weak properties of their components. As a result, composite exhibits superior properties than its constituent components. Composites are used in a number of applications, such as boats, cars, sports goods, and airplanes. Although composites have a long history of in our civilization (i.e. adobe wall), they have been started to utilized in structural engineering applications in the beginning of the 1940s. When it comes to 1960s, Turkey first met the composites in a structural engineering application, Anadol. Anadol is Turkey's first domestic mass-production composite-bodied (fiberglass-bodied) passenger car. The composite body was composed of chopped strand mat reinforced polyester.

Composite might be divided three different groups in terms of the reinforcements used. These reinforcements are chopped strand, particle, and textile fabrics. Chopped strand can be in the mat form or particular form. Chopped strand is used in low-cost applications, such as liquid storage tanks or manholes. Particle reinforcements are usually metal particles which are mixed with a polymer matrix to reinforce to the polymer as well as to ensure thermal and electrical conductivity. Textile fabrics are stitched or weave carbon fiber, glass fiber, aramid fiber, or a hybrid of them. Textile fabrics are usually stacked, and are impregnated with resin to form a laminated composite. In the laminated composite, each layer which composed of cured resin and single fabric layer called lamina. These laminae (plural of the lamina) in laminated composite might have different mechanical properties in each layer through the thickness depend on the direction of fibers and fiber types. Under an applied load, each lamina might behave as independently. For instance, when a laminate is tensioned, a lamina in the bottom might contracts 500 $\mu\epsilon$ due to its fibers, aligned laterally, while lamina in the middle might contract 750 $\mu\epsilon$ due to its fibers, aligned in the loading direction. Since each lamina performs differently as part of a whole, it is also appropriate to call the whole as laminated composite structures (LCS) rather than a composite material (showed in Section 4.3.4 in detail). LCSs are usually used in structural applications such as boats, car, and airplanes, which have strict rules to ensure the safety of a vehicle. The safety of LCS-made vehicle can be ensured if the appropriate damage accumulation behavior and maintenance methods are established for laminated composite structures used in these applications.

In this thesis, we use a number of different sensors, tools, methodology to understand the damage accumulation behavior of LCS. For instance, laminate elastic constants, Poisson's ratio and shear modulus, are used to monitor the effect of damage accumulation on the laminate. Different tools, such as AE and thermography are concurrently utilized along with the monitoring of laminate elastic constants to reveal the interaction between laminate elastic constants and micro-damage accumulation. The following sections and subsections briefly explain the tools and methods used in this study.

2.3 Monitoring and Detection of Damage in LCSs

For a metal airplane, operators are generally concerned with damage in the form of corrosion, fatigue, stress corrosion, and creep. As the modern composite airplane replace their metal counterpart, different types of damage are needed to consider. Damage in a composite airplane initiates as different types of micro-damage due to repetitive loading. These different types of micro-damage are transverse cracks, delaminations, and fiber rupture. Transverse cracks appear in the matrix, fiber ruptures occur in the reinforcement, and delaminations run in the matrix or matrix-reinforcement interface. They can happen anytime and anywhere on the airplane. They sometimes propagate by themselves or coalescence to form one another.

2.3.1 Typical Damage Types

This section provides a brief summary of the damage types that are found on the laminated composite structures during their service. To reduce the complexity, the development of different types of micro-damage are defined under static loading.

2.3.1.1 Transverse Crack

Transverse cracks are usually first types of micro-damage that occur during the static loading of composite. Transverse cracks occur within the matrix of composite and are usually perpendicular to the load. Uneven stress distribution, caused by transverse cracks, lower the elastic modulus of LCS, and hence promote to the occurrence of delaminations and fiber ruptures. A composite airplane can continue to its service with a certain amount of transverse cracks but when transverse cracks reach a critical density, they present a danger to the safety of the airplane.

2.3.1.2 Delamination

Although different sources report different definitions for a delamination (for instance, Voluntary Product Standard PS1, Construction and Industrial Plywood, defines it: "a visible separation between plies that would normally receive glue at their interface and be firmly contacted in the pressing operation"), we will define

it as the separation of plies from each other or resin. Because in LCS there is no need for a visible separation, it can also be on a microscopic scale in which human eye can not detect. In LCS, a higher portion of the load is carried by fiber, and this causes an uneven stress distribution in LCS in micro-scale. Therefore, they usually tend to run resin rich areas due to local uneven stress distributions. They might occur spontaneously or as result of the coalescing of transverse cracks. If necessary measures are not taken, they can easily cause abrupt failure of the whole composite part.

2.3.1.3 Fiber Rupture

Although they might also be seen in the initial stage of a static loading due to manufacturing defects, they predominantly run in the final stage of a static loading of the LCS till the failure. They are the breakage of individual fibers (approx. 6 μm). Fibers are the load-bearing constituent of the LCS, once their breakage accelerates, failure of the composite is only a matter of time.

2.3.2 Damage Detection

Basically, damage detection techniques can be grouped into two sub-categories: active and passive techniques. Active techniques use external sources to detect the damage. For instance, ultrasonic damage detection is an active technique, which use a transmitter to trigger an sinusoidal stress wave on LCS. Stress wave travels through the LCS and hits the receiver. A number of certain features (ie. frequency, amplitude) of captures stress are calculated, then compared with a sound stress wave (the stress traveled when LCS was sound) to check the condition of LCS. However, a passive detection technique does not require an external stimulus, such as a transmitter. In passive techniques, sensors are only used in the recording mode, such as acoustic emission and passive thermography. The stress waves or infra-red radion, released by LCS, due to occurence of micro-damage are captured and converted into a meaningful data to monitor the condition of the LCS. In the following sections, the damage detection techniques, used in this study, are described.

2.3.2.1 Acoustic Emission

Acoustic Emission (AE) is a passive technique based on the detection of the stored elastic and plastic energy before failure of LCS. For instance, when LCS is loaded statically under tensile load, transverse cracks, delaminations, and fiber ruptures occur. These different types of micro-damage release certain amount of elastic energy as a result of sudden local relaxation (or local stress change). This elastic energy propagates through composite as a stress wave. If an AE sensor (piezo electric sensor) is attached to composite, stress wave hits the sensor. The piezo electric sensors, used in this thesis, are wide-band (WD) sensors (PICO - 200-750 kHz Lightweight Miniature AE Sensor, Mistras). The sensor produce a voltage output. That voltage output is amplified by Mistras 0/2/4 pre-amplifier with a gain of 20 dB before sending to signal acquisition box. 20 dB gain produce an output signal, which is 10 times higher than the input signal. In signal acquisition box, the analogue signals (the voltage output, produces by sensor) are recorded and then converted into digital (A/D) signals (ie. signal- based AE [3]) till the fracture of LCS. An acquisition threshold of 40 dB is utilized in AEwinPCI2-4 software such that if the received signal exceeds this pre-set threshold, the signal is recorded as a hit. Acoustic emission signals are collected using a Mistras PCI-2 acoustic emission (AE) hardware with a sampling rate of 2 MHz. It should be noted that hereafter, elastic waves detected by AE sensors and converted into a useful signal can be referred to as hit as well. Once, experiments are finished, signals are post-processed with appropriate software. Post-processed signals are examined to reveal underlying damage damage mechanism, as well as damage accumulation behavior of LCS.

2.3.2.2 Passive Thermography

Passive thermograpy uses only an infra-red camera to measure infra-red radiation to form a thermal image of a LCS under load. As the temperature of the specimen increases under the loading due to released energy, caused by occurence of transverse cracks, delaminations, and fiber rupture, the wavelength of the infra-red radiation, emitted by the specimen, gets smaller. The sensor inside the infra-red camera measure the change in wavelength of the infra-red radiation, and with appropriate software, infra-red camera produces thermal map of the specimen. Equation 2.1 reveals the calculation of a specimen's temperature ((T_{obj})) by an

infra-red camera.

$$T_{obj} = \sqrt[n]{(U - CT_{amb}^n + C\epsilon T_{amb}^n + CT_{pyr}^n)/C\epsilon} \tag{2.1}$$

where U is the output signal of the infrared sensor, C is the camera constant (it is a calibration constant measured by manufacturer), T_{amb} is the temperature of ambient, ϵ is the emissivity constant of specimen, T_{pyr} is the temperature of camera, and n is the power constant of temperature (for higher wavelength, n takes values between 2 and 3, and for smaller wavelength, n takes values between 15 and 17).

2.3.3 Damage Monitoring

The damage in laminates can be monitored directly or indirectly. Direct methods can be visual inspection or x-ray. These two methods directly reveal the damage without using a third quantity. For the indirect methods, damage can be monitored by measuring the change in certain laminate elastic constants, which is caused by different types of micro-damage. These different types of micro-damage can be due to the environmental condition (ie. humidity, temperature change) or loading. In this study, the damage is indirectly monitored by continuously evaluating two different laminate elastic constants, Poisson's ratio, and in-plane shear modulus. Under static loading, both laminate elastic constants indicate a continuous change, as the laminates get damaged due to the increasing load.

2.4 Sensors

Sensors are devices which help us to quantitatively measure changes in the certain environment. The changes in the environment can be an increase in temperature, strain, pressure, or acceleration. Sensors are connected to data acquisition system to record these changes. In this project, four different sensors, namely FBG, strain gage, extensometer, and piezo-electric sensors are used. These sensors are briefly introduced in the following sections.

2.4.1 Fiber Bragg Grating

Fiber optic cables are commonly used in the telecommunication due to their high-speed data transfer property. As the technology advances, fiber optic cables are started to utilized in sensing applications such as strain, temperature, vibration or pressure. Fiber optic cables consist of three different parts. The first part is the core where the light travels. The second part is the cladding which has lower refractive index than the core. This lower refractive index of the cladding guides the light by total internal reflections inside the core. The third part is the coating which affects neither total internal reflections nor guiding of the light. It saves the core and cladding from the harsh environment and provides flexibility to fiber optic cable. FBG is a part of a single mode fiber optic cable, which operates as a pass-band filter for the certain wavelength of the light in reaction to change in temperature and strain. FBG sensor can be multiplexed on a single fiber optic cable. Therefore, from one fiber optic cable, tens of FBG sensors can be accessed via single data acquisition channel. This reduces the cost of each data acquisition per sensor. The accessibility of multi-sensors from single data acquisition channel is impossible for electricity based sensors, such as strain gage. Since data is transferred by light, FBG sensors are immune to electromagnetic interference, as well the data does not get lost due to the long cabling. Typical basics of FBG sensor can be seen in Figure 2.1.

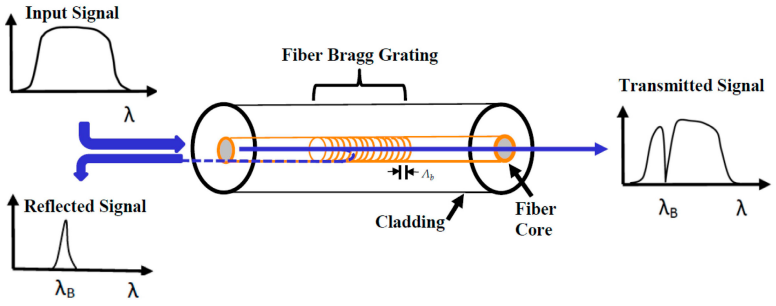

FIGURE 2.1: Typical basics of an FBG sensor [1].

2.4.2 Strain Gage

Strain gage is an electrical device which reacts the change in strain by changing its resistance. The strain measured by strain gage is given by the following formula:

$$\epsilon = \frac{\Delta R}{R}\frac{1}{\kappa_s} \tag{2.2}$$

where ϵ is the strain, ΔR is the change in resistance, R is the original resistance, and κ_s is the gage factor. R and κ_s are predetermined constants by the manufacturer. With an appropriate measurement device ΔR can be continuously measured to calculate ϵ. A biaxial strain gage, used in this thesis, can be seen in Figure 2.2. The right part where metallic foil pattern lies along the long side of the page measures axial strain and left part measures transverse strain if the load is applied on the direction of the long side of the page.

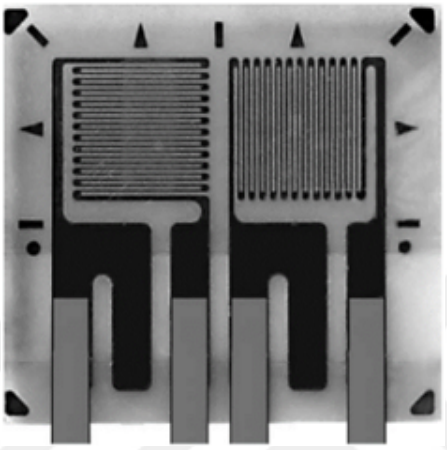

FIGURE 2.2: A biaxial strain gage used in this thesis.

2.4.3 Extensomer

Extensometer is an electro mechanical device which use strain gage to measure the strain on the specimen. Nevertheless, extensomers usually have much bigger gage length than that of strain gages. The distance between the open end of the upper and lower rods constitutes the gage length of an extensometer. These upper and lower rods are connected to a strain gage from the other ends within the its metal box. While lower rod is stationary, upper rod can pivot around a pin. When a tensile strain is applied, the open end of the tip of the upper rod, placed on the specimen's surface, moves upward while the other end of the upper rod which connected to the strain gage moves downward, and hence changes the resistance of the strain gage. Now the strain on the strain gage is known. Due to the pivoting angle, two similar triangles occur on the left and right side of the pin. By using triangle similarity, and the known strain on the strain gage, strain on the specimen is calculated.

Extensometers are lab-scale devices devices and can not be used on-site applications due to their size. On the lab scale, they perform better than strain gage due to its larger gage length. The larger gage length consider more area, hence it perform an overall measurement than local measurement. Extensometers are also reusable devices, whereas strain gages are not. In lab scale, extensometers provide cost advantage compared to strain gages in long term.

2.4.4 Piezoelectric Sensor

Piezoelectric sensors are coupled devices. They generate voltages, when they are tensioned or contracted, which is called generator action. They contract or elongate when they are subjected to voltages, which is called motor action. Due to their coupled property, they can be used as a transmitter or receiver modes. Their small size and weight make them suitable for use in many engineering applications. These applications cover a broad range, such as fuel-igniting devices, solid state batteries, piezoelectric motors, and sound and ultrasound generator and receiver devices. In this study, piezoelectric sensors are used in AE setup to capture the stress waves (stress waves are ultrasound waves because they travel with the velocity of sound) in generator mode. Piezoelectric sensors, used in this study, can be seen in Figure 2.3 as attached to a composite plate.

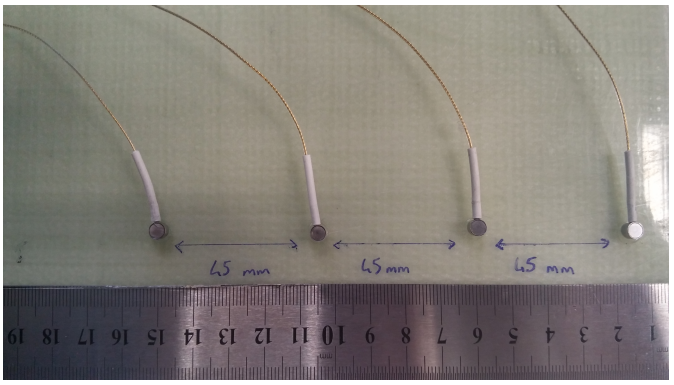

FIGURE 2.3: Piezoelectric sensors, used in this study.

2.5 Signal Processing

Signal processing is an important tool when sensors are involved in a study. Sensors produce raw data on the unit that they measure. For instance, this raw data

for FBG sensor is wavelength (nm) and for piezoelectric sensor, extensometer, and strain gage is voltage (V). The raw data is processed into meaningful data by passing through several steps. The first step is noise filtering. Due to the signal recording electrical devices or sensors itself, raw data always contains a certain amount of noise. This noise should be filtered. For example, raw data of FBG sensor, extensometer, and strain gage is filtered using moving average and exponential moving average filter. These filters can be found in Matlab libraries as ready-to-use functions. Once data is filtered, by using conversion equations, such as from wavelength to strain or from voltage to strain, final meaningful results are produced to use in different approaches such as damage monitoring with Poisson's ratio.

Signal processing of the output of peizoelectric sensor is complicated than FBG sensor, straingage, and extensometer. For instance, Figure 2.4(a) yields a representative portion of an AE signal pocket which is given as an inset in the right upper corner of the same figure. The inset in the right bottom corner indicates the noise on the signal. Figure 2.4(b) gives power spectra obtained through performing Fast Fourier Transform on a waveform such as the one given in Figure 2.4(a). To eliminate the noise on the acquired AE signals, a comprehensive noise removal capability of Noesis software are employed. Bessel band-pass filter of 10th order is applied to all the acquired waveforms. Band-pass filter range is set to 20-800 kHz to eliminate the signals with frequencies below 20 kHz and above 800 kHz. If the Bessel band-pass filter was not applied, the Noesis software would find 1 kHz as the peak frequency at which the signal power is maximum due to the high noise to signal ratio in the AE signal, as seen from the red colored non-filtered power spectra graph in Figure 2.4(b). The blue colored graph is the filtered signal which does not include a high signal power at 1 kHz.

Figure 2.4(a) also gives an AE signal together with its some well-known features in the time-domain, such as duration, rise time, and amplitude. The duration is the total time of an AE signal above the pre-set threshold value, the rise time is the time of rising for the AE signal from a pre-set threshold amplitude to its highest amplitude value, and the amplitude is the magnitude of the acquired signal which determines how loud an AE event is. The maximum amplitude of an AE signal in time domain is given by the following formula:

$$A_{max}[dB] = 20log(V_{max} * 10^6[\mu volt]) - G \tag{2.3}$$

where the voltage is V and G is the preamplifier gain which is 20 dB for this study.

In addition to the AE signal features in time-domain, the Noesis software is also used to obtain relevant AE signal features in frequency domain, such as peak frequency (f_p), frequency centroid (f_c), partial powers (ie., PP1, PP2, PP3, and PP4), and weighted peak frequency (f_{wp}), among others, once the noise removal is completed f_{wp} is calculated using the relation,

$$f_{wp} = \sqrt{f_p * f_c} \tag{2.4}$$

where peak frequency (f_p), defined as the point in the power spectra at which magnitude is maximum, and frequency centroid (f_c), calculated as,

$$f_c = \sum f * A(f) / \sum A(f) \tag{2.5}$$

in which $A(f)$ is the amplitude of power spectrum at frequency f.

Partial power is defined as the percentage of energy available at a given frequency range in the power spectrum of the waveform. Here partial power 2 ($PP2$) is determined by summing the power spectrum (it spans between 20 and 800 kHz for this thesis) in the range of $250 - 450$ kHz, which is divided by total power, and multiplied by 100.

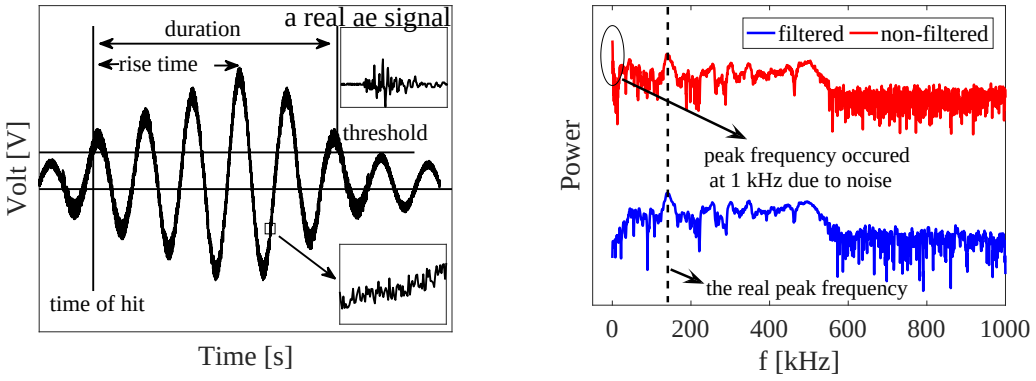

(a) (b)

FIGURE 2.4: (a) A representative waveform of an AE signal in the time domain where the inset in the right bottom corner shows the noise while the one in the top right corner indicates a real AE signal, and (b) filtered and non-filtered power spectra of an AE signal in frequency domain.

Chapter 3

Monitoring Poisson's Ratio of Glass Fiber Reinforced Composites as Damage Index Using Biaxial Fiber Bragg Grating Sensors*

Abstract:

Damage accumulation in Glass Fiber Reinforced Polymer (GFRP) composites is monitored based on Poissons ratio measurements for three different fiber stacking sequences subjected to both quasi-static and quasi-static cyclic tensile loadings. The sensor systems utilized include a dual-extensometer, a biaxial strain gage and a novel embedded-biaxial Fiber Bragg Grating (FBG) sensor. These sensors are used concurrently to measure biaxial strain whereby the evolution of Poissons ratio as a function of the applied axial strain is evaluated. It is observed that each sensor system indicates a non-constant Poissons ratio, which is a sign of damage accumulation under the applied tensile loading. As the number of off-axis plies increases, transverse strain indicates a notable deviation from linearity due to the formation of transverse cracking, thereby leading to a larger reduction in Poissons ratio as a function of applied axial strain. Here, it is demonstrated that biaxially

*Appears in: C. Yilmaz, C. Akalin, E.S. Kocaman, A. Suleman, M. Yildiz, Monitoring Poissons ratio of glass fiber reinforced composites as damage index using biaxial Fiber Bragg Grating sensors, Polymer Testing, Volume 53, August 2016, Pages 98-107

embedded FBG sensors are reliable to monitor the evolution of Poissons ratio, unlike biaxial strain gages which record strain values that can be significantly influenced by the cracks formed on the surface of the specimen.

Keywords: Poissons ratio; Transverse cracking; Stress transfer; Glass fibers; Fiber Bragg Grating

3.1 Introduction

Glass or carbon fiber reinforced polymeric composites have received a great deal of attention due to their high specific strength and stiffness for structural applications. The relatively high specific strength of composite materials makes them suitable for applications where the weight and operating costs are intimately coupled. In comparison to metallic materials, where the failure is usually triggered by a single crack during their service life, composite materials exhibit poorly characterized damage mechanisms due to the existence of multiple cracks, which makes the prediction of service life rather complex and difficult. Therefore, in literature, there are several approaches developed and investigated to understand the accumulation of damage and damage state of composite structures under static and dynamic loading conditions. For example, [4] studied stiffness reduction as a damage indicator in composite materials. Several researchers examined the reduction of Poisson's ratio as a damage indicator ([5], [6], [7], [8]) since Poisson's ratio ($\nu_{xy} = -\epsilon_y/\epsilon_x$) embodies both axial and transversal strain (ϵ_x and ϵ_y, respectively) information and is affected by the transverse cracks formed as a result of applied longitudinal strain ([9], [10], [11]). [9] investigated the evolution of Poisson's ratio of composite materials as a function of applied longitudinal strain, and showed that Poisson's ratio decreases by the applied strain. [11] modelled the evolution of Poisson's ratio using a shear-lag theory under static loading conditions, correlated their analytic model with experimental results, and indicated that Poisson's ratio decreases as the transverse crack density increases.

The measurement of Poisson's ratio of composites subjected to dynamic and static loading has mainly been performed using strain gages and extensometers. Due to their size, these sensors cannot be embedded in composite structures, and thus measure the strain from the surface. Additionally, surface mounted strain gages detach easily under cyclic loading, even at relatively few cycles. Moreover, strain

gage and extensometer are sensitive to electromagnetic interference, and hence cannot be used in environments with high electromagnetic interference. To circumvent the drawbacks of strain measurements with surface mounted electrical strain sensor systems, one promising approach is the utilization of embedded Fiber Bragg Grating (FBG) based sensor systems [12]. FBG is a section of a single mode optical fiber which contains a periodic variation of refractive index formed holographically on the core of the optical fiber along the fiber direction, and acts like a stop-band filter [13–15]. An FBG sensor reflects a small portion of the incoming electromagnetic spectrum while enabling the passage of the others. The center wavelength of the reflected portion of the incident electromagnetic spectrum is referred to as the Bragg wavelength, $\lambda_B = 2n_{eff}\Lambda$ where Λ is grating period and n_{eff} is the effective refractive index of the FBG sensor. When subjected to strain or temperature variations, the grating period and the effective refractive index of the FBG sensor change, thereby causing a shift in the Bragg wavelength λ_B. The change in the Bragg wavelength can be coupled to external effects, namely, temperature and strain through the following equation $\Delta\lambda_B/\lambda_B = (\alpha + \xi)\Delta T + (1 - \rho_e)\epsilon$ where α and ξ are the thermal expansion and thermo-optic coefficients of the fiber core, respectively. Here, $\Delta\lambda_B$ is the shift in the Bragg wavelength, ΔT is the change in the temperature of the grating region and ρ_e denotes effective photo-elastic constant of the fiber core, which is taken as 0.22 in this work, and ϵ is the axial strain of the grating region. For a constant temperature, one can write the previous relation as $\Delta\lambda_B/\lambda_B = (1 - \rho_e)\epsilon$.

In this study, we have investigated the effect of transverse cracking on the reduction of Poisson's ratio as a function of imposed axial strain. To this end, composite specimens with three different ply stacking sequences (i.e., uniaxial laminates, and laminates with two and four 90° off-axis plies) are instrumented with a biaxial extensometer and strain gage and then subjected to a quasi-static loading, thereby shedding light on the intimate relation between the reduction in Poisson's ratio and the off-axis/transverse ply cracking. Given that, in angle ply composites, the deformation in the lateral direction is enhanced, which can easily obscure the effect of transverse cracks on the lateral deformation, we limit our study to laminates with 0° and 90° stacking orientations. A novel approach for embedding biaxial FBG sensor into a composite laminate is proposed and utilized for multi-axis strain acquisition as well as for structural health monitoring of composites through referring to the reduction in Poisson's ratio. Specimens with extensometer, strain gage and embedded biaxial FBG sensor are subjected to quasi-static

cyclic loading to study the reduction in Poisson's ratio under cyclic loading. It is shown that there can be notable variation in the values of lateral strain recorded by extensometer, strain gage and FBG sensor due to the difference in the gage length of these strain sensors. Referring to the reduction in Poisson's ratio, it is shown that composite specimens with a higher number of off-axis plies are more prone to the formation of transverse cracks. This study contributes to the state of the art in the field of composites materials testing and it is the first reported study on the measurement of decline in Poisson's ratio for composites with different fiber stacking sequences using embedded biaxial FBG sensors.

3.2 Methodology

The fiber reinforcement consists of 330 gsm uni-directional (0°) E-glass stitched fabric (Metyx, Turkey) with the trade code of L300 E10B-0. The properties of the glass fibers used here are provided in Table 3.1. The matrix material is Araldite LY 564 epoxy and XB3403 hardener system purchased from Huntsman. Glass fibers were impregnated with resin by using vacuum infusion and then cured at 75 °C for 15 hours. In this study, three composites laminates with the fiber stacking configurations of $[90/90/0]_s$, $[90/0/0]_s$, $[0]_6$ were manufactured, which are respectively denoted by G6B1, G6B2, and G6U1 for convenience. Figure 3.1(a) shows a composite specimen mounted on the wedge grips of the universal testing machine system with dual-extensometer system utilized in this study, while Figures 3.1(c)-3.1(d) presents the geometry of a test specimen with and without FBG sensors. In this study, we have used dual FBG sensors (purchased from Technesa with $\lambda_B = 1540$ nm (transversal) and $\lambda_B = 1550$ nm (axial) and a gage length of 1 mm written holographically within the core of a polyimide coated single mode fiber such that the distance between both FBG sensors is nearly 21 cm. The optical cable with dual FBG sensors is fixed to the dry ply before composite manufacturing by interlacing it through stitching fibers of the ply in a configuration shown in Figure 3.1(c). The ply with FBG sensors is stacked such that FBG sensors are embedded into the symmetry axis of laminates during the manufacturing stage. It can be seen from Figure 3.1(b) that the section of the panel including the FBG sensor is cut into a L-shape so that the specimen can be clamped by the wedge grips of the universal machine without damaging the

egress region of the FBG sensor. The egress/ingress of the optical cable into the composite was described in our previous study [15].

TABLE 3.1: Properties of fiber reinforcement.

0	600 Tex	283 gr/m^2
90	68 Tex	37 gr/m^2
Stitch	76 Dtex	10 gr/m^2

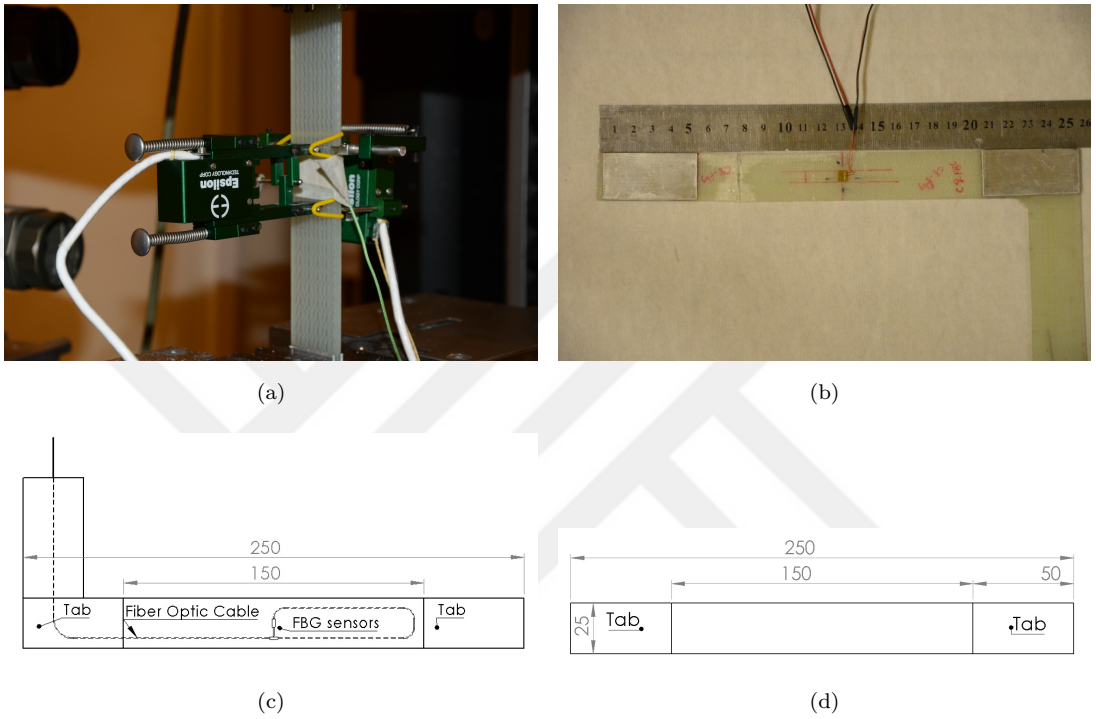

FIGURE 3.1: A tensile test specimen mounted on the test machine with dual extensometer system, (b) L-shaped test specimen with embedded biaxial FBG sensors, and (c) the schematic drawing of test specimens with, and (d) without FBG sensor

All static tensile tests were performed using a Zwick Z100 universal testing machine with a ± 100 kN load cell. Static tensile tests on composite specimens with or without embedded biaxial FBG sensors were conducted under the displacement control of 2 mm/min according to ISO 527 (ASTM 3039) standard. A Micron Optics SM230 model interrogator was used to acquire the FBG signals with a sampling frequency of 1000 Hz during the experiments with Micron Optics Enlight Software. General purpose biaxial strain gages purchased from Micro-Measurements are used as axial and biaxial sensors with the code of C2A-06-062LW-350 and C2A-06-062LT-350, respectively. All the strain gages have a gage length of ∼1.57 mm (0.062 inche) and a resistivity of 350 ohms. An Epsilon 3542 axial extensometer with a fixed gage length of 25 mm and an Epsilon

3575 transverse extensometer with a controllable gage length were utilized during tensile tests. Extensometer and strain gage data were collected concurrently by a National Instruments NI SCXI-1000 main chassis with a NI SCXI-1520 card at a sampling frequency of 1000 Hz. After tensile tests, small samples were cut from tested specimens with different stacking sequences using a water cooled diamond saw and then polished on their thickness side to visualize transverse cracking with an optic camera (Nikon ECLIPSE ME600).

3.3 Results and Discussion

3.3.1 Quasi Static Tensile Test

3.3.1.1 The Effect of Stacking Sequence on the Evolution of Poisson's Ratio

In order to assess the evolution of Poisson's ratio of composite plates with different stacking sequences, test specimens were subjected to quasi-static tensile loading until failure and all the data collected during the tests were processed and tabulated in Table 3.2 along with the fiber volume fractions. During the quasi-static tensile tests of all composite coupons, both axial and transversal strains were recorded by extensometers. Biaxial strain gages were attached only to a single coupon for each plate to investigate the effect of sensor type (i.e., gage length, measurement location) on the strain measurement. Figure 3.2(a) yields stress-strain curves for composite coupons having different stacking sequences. One can see from Table 3.2 that, as the number of 0° layer increases, so do the strength and elastic modulus of composites, as expected. It is observed that the axial strain at failure does not differ significantly for composites with three different stacking sequences. Considering the iso-strain condition, strain of fibers, composite and matrix must be same at break, namely, $\epsilon_c = \epsilon_f = \epsilon_m$. The fact that the failure of the composite takes place at the ultimate strain of the fibers parallel to the loading direction explains why composites with different stacking orientations have nearly the same axial strain. On the other hand, as seen in both Figure 3.2(b) and Table 3.2, on increasing the amount of 90° fibers (perpendicular to loading), the ultimate transverse strain of the composite decreases due to the fact that 90° fibers increase the elastic modulus of the composite in the transversal direction.

TABLE 3.2: Mechanical properties of composites with three different stacking configurations (strain measurements are based on extensometer).

	G6U1 $[0]_6$	G6B2 $[90/0/0]_s$	G6B2 $[90/90/0]_s$
Strength (σ_u)	716	508	310
Elastic Modulus (GPa)	28	20	15
Axial Strain (ϵ_x) ($\mu\epsilon$)	26175	26500	25739
Transverse Strain (ϵ_y) ($\mu\epsilon$)	5363	2578	1334
Fiber Volume Fraction (v_f) (%)	41.3	38.1	42
Maximum Poisson's ratio	0.253	0.167	0.113
Minimum Poisson's ratio	0.203	0.095	0.051
Percent change (%) in Poisson's ratio	19	41	54

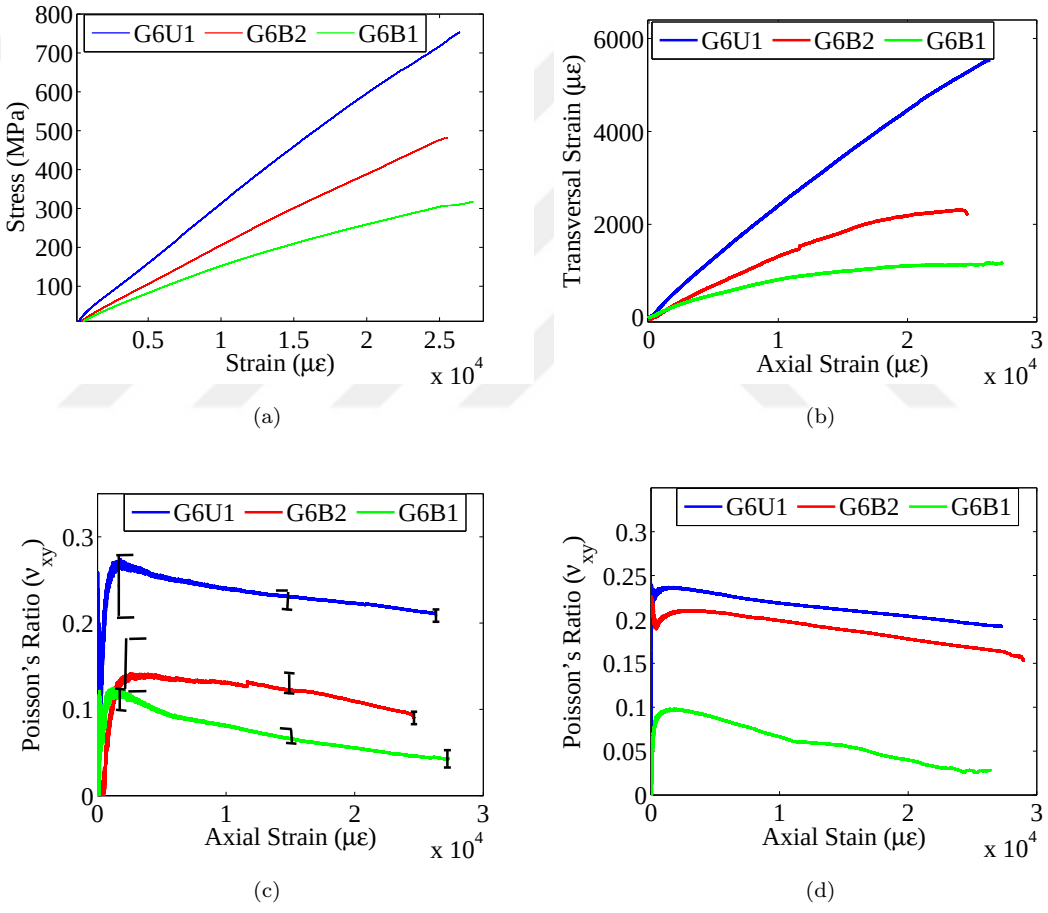

FIGURE 3.2: A representative stress-strain (extensometer) curve (a), the variation of extensometer based transverse strain as a function of axial strain for composite with three different stacking sequences (b), and the evolution of Poissons ratios with respect to axial strain measured by extensometers and strain gages, respectively (c)-(d).

Poisson's ratios for three different stacking sequences are calculated using experimental data collected by dual extensometers during quasi-static tensile tests and

are also given in Table 3.2. Figure 3.2(c)-(d) presents the variation of extensometer and strain gage based Poisson's ratio as a function of the axial strain for three different stacking configurations. Here, the plot for each stacking sequence is associated with the result of one of the five tests performed for a given stacking orientation. It is observed that the Poisson's ratio sharply increases with rise in the axial strain and reaches a maximum point, which will be hereafter referred to as the maximum Poisson's ratio. Thereafter, it decreases continuously until failure of the specimen. The Poisson's ratio at failure point is termed the minimum Poisson's ratio. The initial increase in the Poisson's ratio can be explained such that, at the early stages of the experiment, the transversal strain varies nonlinearly with respect to the axial strain, as can be seen in Figure 3.2(b). Hence, the increase in the axial strain as the test continues generates a larger increase in the lateral strain whereby the Poisson's ratio increases and reaches a maximum. Referring to Figure 3.2(c)-(d), one can immediately note that, as the number of 90° plies increases, the composite specimen has smaller maximum and minimum Poisson's ratio, which is due to the higher elastic modules of off-axis plies than the matrix.

In reference [8], the decrease in the Poisson's ratio was associated with the enhancement of the elongation of the composite specimen due to the formation of transverse cracks under tensile loading, such that the specimen elongates further in the loading direction, hence causing a continuous decrease in the Poisson's ratio. If the axial elongation was notably influenced by the transverse crack density, one would expect higher elongation as the number of 90° plies increased given that, the higher the number of off-axis plies, the bigger the transverse crack density. However, as seen from Table 3.2, all three different stacking configurations have nearly the same axial strain at the failure. We suggest that the decreasing trend in Poisson's ratio is associated with the reduction in the rate of increase of the lateral strain due to transverse cracking. Knowing that transverse cracking will reduce the transfer of axial stress to the lateral direction, the specimen should experience a progressively smaller increase in the lateral strain with applied load as the test continues. It would be prudent to expect that, the larger the number of 90° plies, the bigger would be the drop in the Poisson's ratio, as can be seen from Table 3.2. This bespeaks that the nearly linear decrease in the Poisson's ratio as a function of applied axial strain is directly controlled by the density of transverse cracking.

3.3.1.2 The Effect of Sensor Type on the Lateral Strain Reading and the Evolution of Poisson's Ratio

To be able to investigate if the apparent decreasing pattern in Poisson's ratio was an experimental artifact of the strain measurement using a dual extensometer system for three different stacking sequences, biaxial strain gages were mounted on a composite specimen for each stacking sequence. Subsequently, specimens were subjected to the quasi-static tensile test and the strain gage data were processed and then plotted as Poisson's ratio versus axial strain, as seen in Figure 3.2(d). Poisson's ratio calculated based strain gage data shows exactly the same behavior as that calculated using dual extensometer, such that the maximum value of the Poisson's ratio decreases as the number of 90° plies increases, and also Poisson's ratio reveals increasing and decreasing pattern as a function of axial strain. However, numerical values of Poisson's ratios calculated with the strain gage data are different from those with the extensometer for corresponding stacking configurations. Observed in the experimental data plotted in Figure 3.2(d), the change in the Poisson's ratio is around %18 for the G6U1, %27 for G6B2 and %97 for the G6B1. The significant difference in the variation of Poisson's ratio based on the strain values measured by strain gage and extensometer (refer to 3.2) for G6B1 can be attributed to the strain measurement location and the sensitivity of the lateral strain gage to transverse cracks. One can see from Figure 3.3(a) that the difference in axial strains measured by strain gage and extensometer are very small. However, the transversal strains measured by both types of sensor have a considerable difference, as shown in Figure 3.3(b). This difference is obviously due to the place of measurement such that lateral strain gage measures the strain locally due to its small gage length, and is hence rather sensitive to the occurrence of transverse cracks.

During the curing of resin, the composite shrinks whereby residual compressive strains are built in the cured composite structure. To quantify the amount of compressive residual strain, the manufacturing process was fully monitored by acquiring the signals of embedded FBG sensors. To this end, the center wavelengths of two FBG sensors were collected before, during and after the manufacturing process continuously. The changes in the center wavelength of axial and transversal FBG sensor were observed to be -1.1 nm and -0.43 nm, corresponding to -920 $\mu\epsilon$ and -325 $\mu\epsilon$, respectively, which points to the compressive residual strain on FBG sensors due to the shrinkage of the epoxy matrix during the cooling of composite.

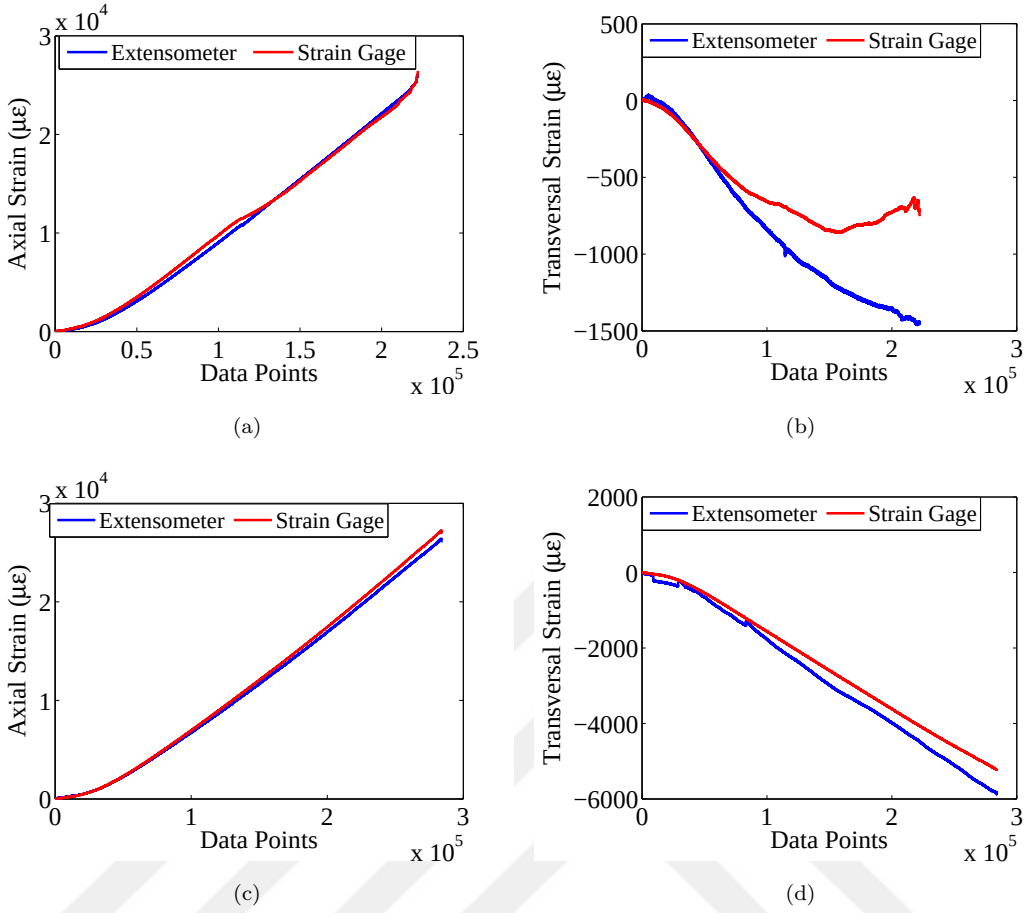

FIGURE 3.3: The variations of strain gage and extensometer based axial and transversal strains versus data point for G6B1 (a-b), and G6U1 (c-d)

On the application of axial loading on the composite specimen, transverse cracks form whereby the compressive residual strain on the off-axis fibers are relaxed, thus enabling these fibers to spring back in the transversal direction and, in turn, lessening the lateral strain due to the application of the axial loading. Since the transverse extensometer measures global average strain within its gage length, it is not able to detect the local variation in transversal strain due to the changes within the composite. On the other hand, the transversal strain gage measures the strain locally from the surface of the laminate, unlike the transversal extensometers which evaluate the strain from the edges of the specimen. Given that the laminate G6B1 has the higher number of 90° fibers of the three laminates, it should have a higher density of transverse crack when subjected to the axial loading, whereby its transversal strain measured by the strain gage will notably deviate from the extensometer based strain due to the relaxation of the compressive residual strain with crack formation. For G6U1 which has no 90° fibers, the

deviation of axial and transversal strains measured by the biaxial strain gage from those acquired by the axial and transversal extensometers is negligibly small, as seen in Figure 3.3(c)-(d). Therefore, there is a negligible difference in the percent change of Poisson's ratio based on the transversal strain gage and extensometer for G6U1. This observation and the associated conclusion is strong evidence of the effect of transverse crack density on transverse strain measurement and, in turn, on the calculated Poisson's ratio. In order to further substantiate the conclusion drawn that the transversal crack density significantly affects the measured transversal strain and Poisson's ratio, the thickness-wise surface of the fractured specimens with three different stacking configurations was examined under an optical microscope after the surface preparation, and the results are presented in Figure 3.4(a)-(c). One can see that, as the number of off-axis plies increases, more transverse cracks are created in the test samples.

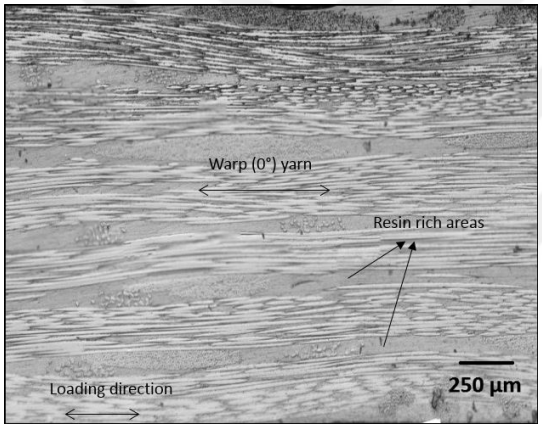

(a)

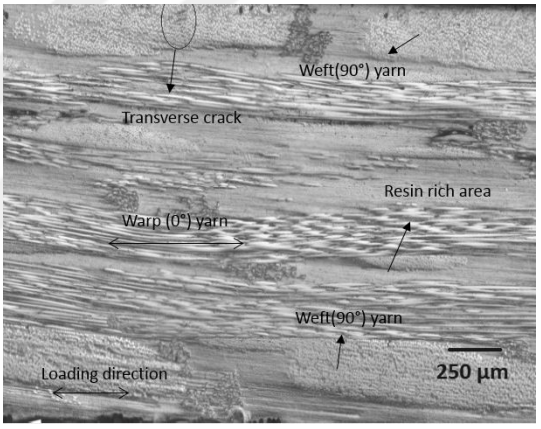

(b)

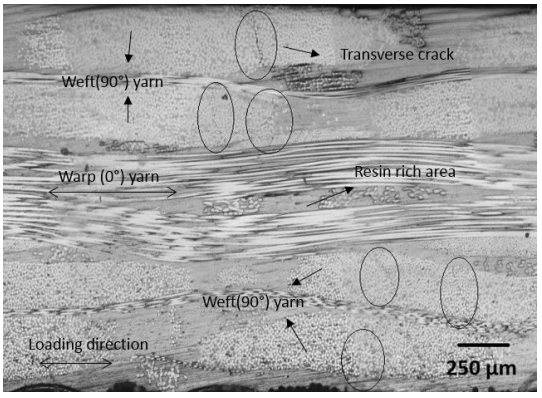

(c)

FIGURE 3.4: The variations of strain gage and extensometer based axial and transversal strains versus data point for G6B1 (a-b), and G6U1 (c-d).

3.3.2 Quasi Static Cyclic Tensile Test

3.3.2.1 Damage Accumulation.

Three composite laminates with three different stacking sequences (i.e., G6U1, G6B2, and G6B1) were manufactured with embedded biaxial FBG sensors and then cut into tensile specimens. These specimens were instrumented with a biaxial strain gage, biaxial FBG sensor, and axial and transversal-extensometer, and then subjected to quasi-static cyclic tensile testing with a load increment of 50 MPa after each complete cycle until failure. During the initial loading cycle, certain damage modes such as transverse cracking, delamination and splitting occur. In the subsequent loading cycles, the damage created in previous cycles accumulates. Therefore, the quasi-static cyclic test enabled us to examine the effect of axial strain level on the damage state and accumulation in composites, thereby revealing the efficacy of monitoring Poisson's ratio for following the damage state of composite materials. The loading history of a test specimen as a function of displacement and time is given in Figure 3.5(a) and (b), respectively, for G6B1.

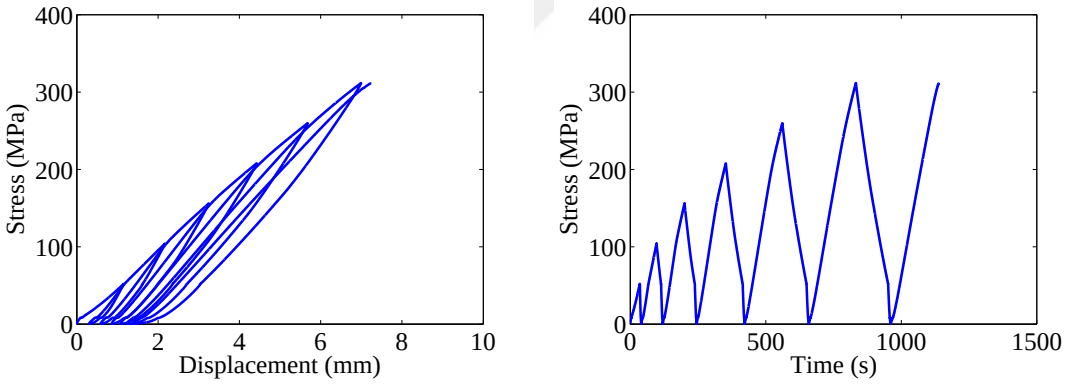

FIGURE 3.5: The loading history of a test specimen instrumented with surface mounted bi-axial strain gage, dual extensometer, and embedded biaxial FBG sensor for G6B1.

To show the formation of transverse cracks during the quasi-static cyclic tension test, the tensile experiment on G6B1 specimen was recorded in a video using a Nikon D7100 camera with a macro lens while the specimen with a black background was subjected to a white light source. Figure 3.6(a)-(h) presents image frames extracted from the video for different stress levels. At lower stress levels up to 100 MPa, transverse cracks are not visible, but the color of the specimen

changes gradually to blurry white since micron or submicron cracks alter the refractive index of the specimen. When the stress increases up to 150 MPa, cracks become visible and the color of the specimen completely turns to milky white since the rise in crack density scatters the light more thereby causing a color shift in the specimen. As the stress continues to increase further, transverse cracks become more visible, and the color of the specimen gets milkier due to scattering of light by small cracks. After the failure of the specimen, there is a noticeable reduction in the white contrast and visibility of the cracks with respect to the previous frame, which can be attributed to the removal of the load from the sample due to breaking, resulting in the closure of some open cracks.

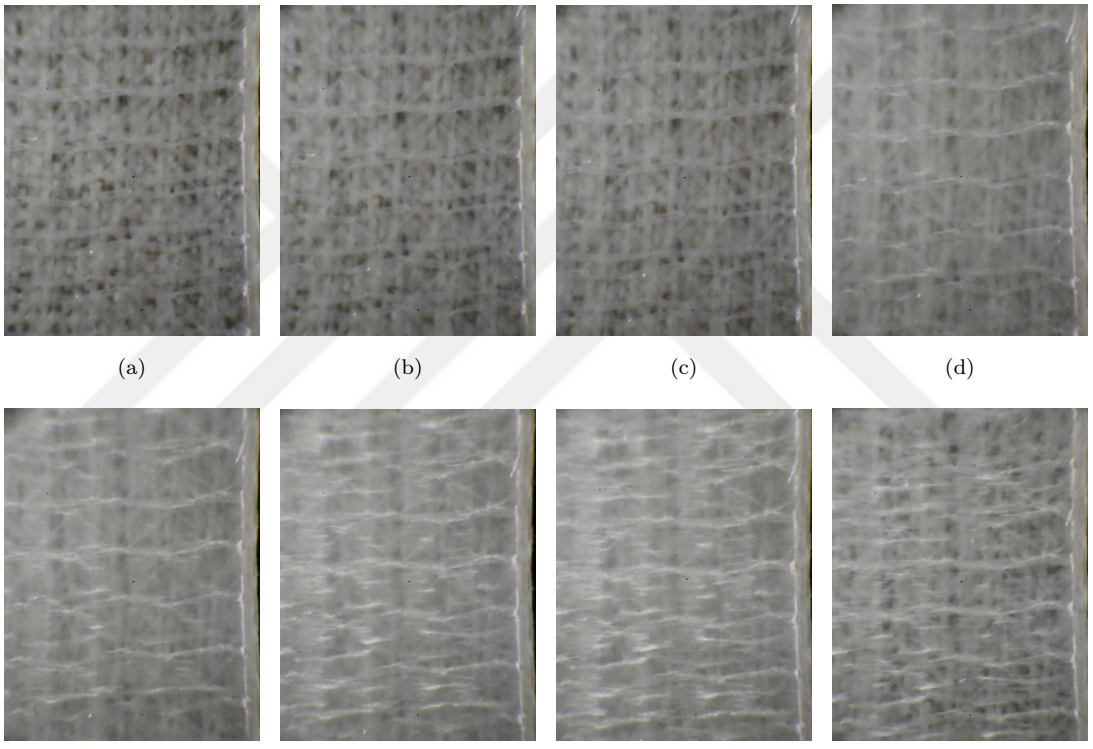

FIGURE 3.6: The deformation of a test specimen from the G6B1 laminate which was recorded by a macro lens attached to a camera; a) 0 MPa load, b) 50 MPa, c) 100 MPa, d) 150 MPa, e) 200 MPa, f) 250 MPa, g) 280 MPa (just before failure), and h) just after breakage.

The variations of axial and transverse strains measured simultaneously by extensometer, strain gage and FBG sensor during the quasi-static cyclic tensile tests are provided in Figure 3.7(a)-(f). As one can note from Figure 3.7(a)-(c), in the first loading cycle, all three sensors measure nearly the same axial strain values for three stacking sequences, albeit with minor differences. It is interesting to note that the axial strain values recorded by three different sensor systems for specimens with

off-axis plies start deviating from each other as the cycle number increases. These deviations start at earlier cycles for the specimen with four off-axis plies in comparison to that with two off-axis plies. As for the specimen without off-axis plies, all three sensors have a negligible difference in the acquired axial strains during the entire loading history. This indicates that composites with off-axis plies are quite prone to the formation of transverse cracks which are known to alter the strain state within specimens, whereby different sensors read slightly dissimilar values. In other words, locally and globally measured strains can differ from each other owing to the difference in the gage length of the sensors used and the crack density and the orientations in the proximity of these sensors. The upward shift in the trough of the axial strains of all sensors under zero loading in Figure 3.7(a)-(c) is due to the permanent damage in the composite specimen.

Figures 3.7(d)-(f) show that three different sensors measure nearly the same maximum lateral strain for the very early cycles, even in the composites with different stacking sequences. On the formation of transverse cracks, the lateral strain state in the composite changes significantly. So far, it has been understood that the density of transverse cracks is larger in composites with 90° plies than with 0° plies, and thus the local permanent deformation due to the transverse cracking is expected to be smaller in G6U1. Hence, the local lateral strain measured by the FBG sensor is very much the same as that collected by surface mounted extensometer, as seen in Figure 3.7(d). One can see from Figure 3.7(e)-(f) that the strain readings of sensors with smaller gage length notably deviate from the extensometer in composites with off-axis plies. This is not due to the malfunctioning of any sensors; it is rather related to the damage state in the vicinity of the sensors and their gage length. Extensometers, due to their larger gage length, measure average strain in comparison to strain gage and FBG sensors and, therefore, in the structures prone to local damage formation, the readings of sensors with smaller gage length can be different, and also this difference is further enhanced depending on whether if the strain reading is obtained from the surface or the internal part of the specimen. To recapitulate, stacking configuration affects damage state in the structures, and hence the strain readings of different sensors.

To substantiate that stacking configuration affects damage state in composite structure, thereby leading to difference in the strain fields measured by sensors with different placement and gage length, damage events for G6U1 and G6B2 specimens were monitored using a Mistras PCI- 2 acoustic emission (AE) system

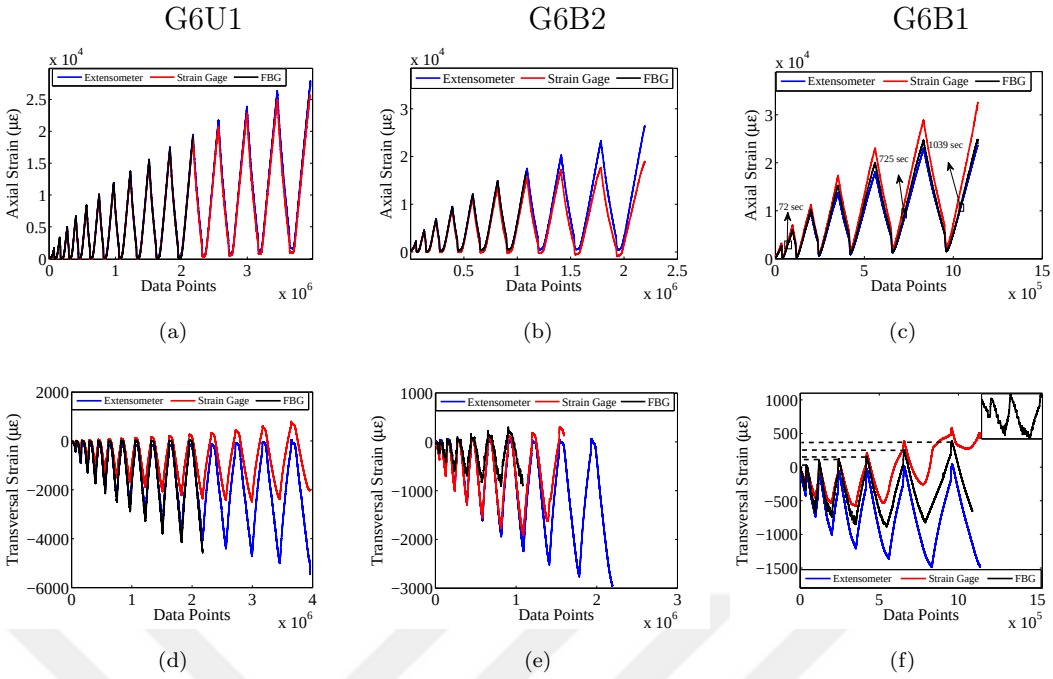

FIGURE 3.7: The variation of axial strains for a) G6U1, b) G6B2, c)G6B1 and transversal strains for d) G6U1, e) G6B2, f) G6B1 recorded by three different sensor systems.

where AE hits were collected by two wideband piezo electric sensors. Centroid frequency and peak frequency were determined to calculate weighted peak frequency (WPF), as described in [16] using Noesis software. WPF versus amplitude for G6U1 and G6B2 stacking sequence is provided in Figure 8 where one can identify three different well-separated cluster regions around 90, 190 and 400kHz, which can be associated with transverse cracking, fiber-matrix debonding and fiber fracture, respectively [17]. It is straightforward to conclude that, when the number

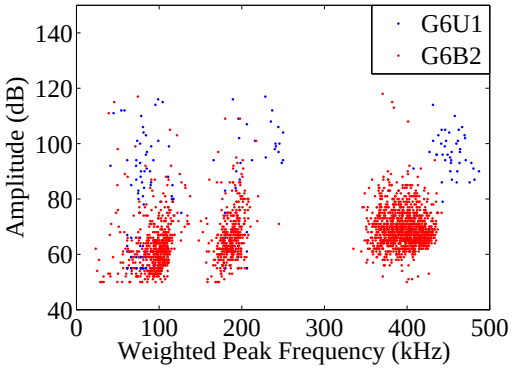

FIGURE 3.8: Weighted peak Frequency versus amplitude for G6U1 and G6B2.

of off-axis plies increases, there is a notable increase in the number of hits in the

transverse crack region, as seen in Figure 3.8. Therefore, it is natural that the difference in lateral strain readings of the sensor with quite different gage lengths will be larger as the off-axis plies in composite specimens increase, as seen in Figure 3.6(d)-(f).

3.3.2.2 Relaxation of Compressive Residual Strain.

Another interesting point that can be noted particularly from Figure 3.7(d)-(f) is that the lateral strains measured by the strain gage and FBG sensor acquire positive values under zero loading, which was also reported in [8, 9] without any discussion on possible physical reason, and considered to be a peculiar behavior in sensor reading. It is inferred that this is due to the relaxation of the curing induced compressive strain in both axial and lateral directions due to the transversal crack formation discussed in the previous section. The magnitude of the positive lateral strain increases with the cycle number. Specifically, as seen from Figure 3.7(f) belonging to the specimen with four off-axis plies, the lateral FBG strains under zero loading condition for the third, fourth and fifth and last cycles are 95, 110 and 145 and 384 $\mu\epsilon$ respectively. Figure 3.7(f) also reveals that, after the fourth cycle, lateral strain of strain gage decreases with respect to the previous cycle, although the corresponding axial strain increases. One may argue that this can be due to the malfunctioning or debonding of the strain gage. However, given that the strain gage utilized is a rosette type biaxial strain gage, if there were such debonding, the axial strain would have indicated an off-track trend. The notable deviation in the strain gage recorded lateral strain after the 4th cycle might be attributed to the extensive transversal cracks. It is noted that the extensometer due to its larger gage length is not as sensitive to the relaxation of the curing induced compressive strain as the other two local sensors.

One can clearly observe that the variation of lateral FBG strain in the loading cycles is irregular for composites with off-axis plies. It is considered that transverse cracks formed in the loading cycles are the source of this irregular strain field since the lateral FBG sensor, due to its small gage length, is sensitive to the variation of local strain associated with the cracks and damages formed in its vicinity. As can be seen from Figure 3.7(d)-(f), the variation of strain in the unloading cycles is rather smooth compared to the loading cycle since no new damage is inflicted during the unloading cycle. To prove that the wavy nature of the lateral strain

is not due to splitting of the reflected spectrum of the FBG sensor, the spectrum of the FBG sensor peaks was monitored and illustrated in Figure 3.9 as a plot of peak intensity versus data points, from which one can identify a very clear single peak with a well-defined Bragg wavelength [14].

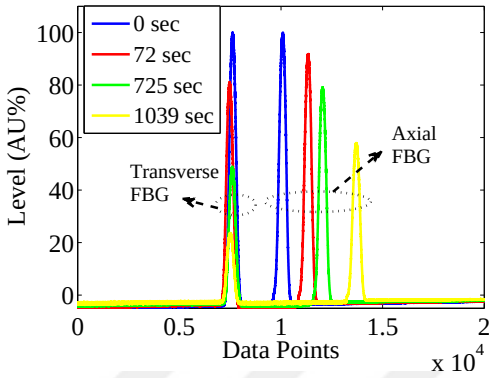

FIGURE 3.9: Spectrum of axial and transversal FBG sensor.

3.3.2.3 The Variation of the Poisson's Ratio under Quasi-Static Cyclic Loading.

Figure 3.10(a)-(c) presents the evolution of Poisson's ratio under quasi-static cyclic loading determined using the strain readings of three different sensor systems for specimens with three different ply stacking configurations in a matrix form with the row for the sensor type and the column for the stacking sequence. For the G6B1 plate in Figure 3.10(a), each sensor system indicates the same decreasing trend in Poisson's ratio. It is worth noting that the Poisson's ratio of each subsequent cycle follows a different path from the previous cycle, except the first two cycles because the applied load has not induced sufficient damage to cause a change in the path of Poisson's ratio. After the second cycle, the applied axial strain can create sufficient transverse cracks and damage in composite materials, and thus Poisson's ratio follows a dissimilar path to the previous cycles. As the axial load is incremented, the Poisson's ratio gets a smaller maximum value, and also the difference between maximum and minimum values of Poisson's ratio decreases. This is attributed to the fact that, on the formation and accumulation of transverse cracks, the axial strain cannot be transferred in the lateral direction and, therefore, the lateral strain for a given axial strain decreases with respect to the previous cycle.

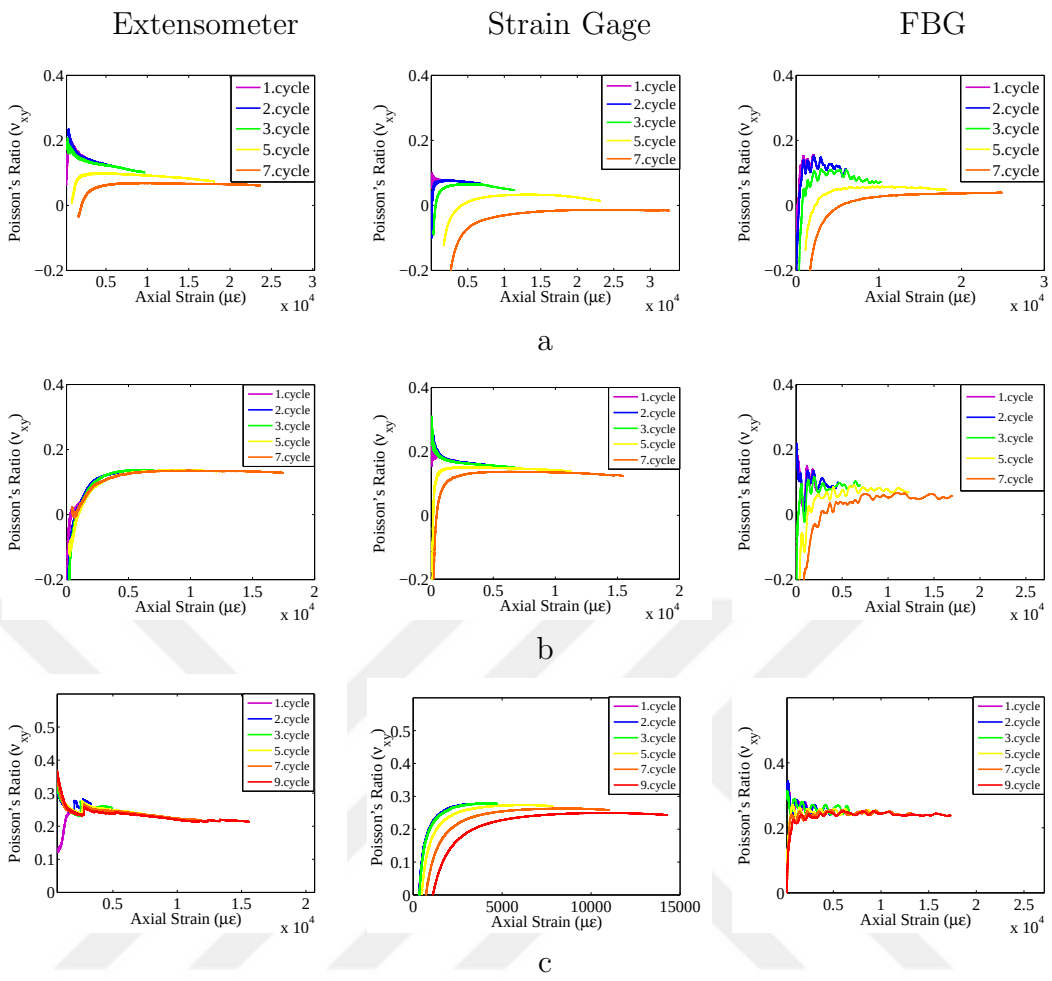

FIGURE 3.10: The evolution of Poissons ratio under cyclic loading monitored based on the strain fields acquired by three different sensor systems for three different stacking sequences, namely, a) G6B1, b) G6B2, and c) G6U1, given row-wise ordering.

Unlike strain gage or extensometer, which measures average strain fields across their gage length, thus not being notably influenced by local strain variations, the Poisson's ratio based on the strain field of the embedded biaxial FBG sensor is wavier. This stems from the irregular nature of the lateral FBG strain, as discussed previously. The waviness is more observable in the initial loading cycles since the damage generation rate is faster in these cycles. In later cycles, the rate of new damage formation decreases and the strain state of the structure does not change considerably, thereby leading to less momentous variation in the Poisson's ratio. At subsequent cycles, for lower axial strain levels, Poisson's ratio calculated using strain values of strain gage and FBG sensor possesses negative value due to positive lateral strain under the zero load due to the relaxed compressive strain.

Comparing the results in Figure 3.10(a)-(c) in terms of stacking sequences, one can

easily note that the Poisson's ratio increases as the number of 90° plies decreases, as expected. The drop in the Poisson's ratio between the first and the final loading increases as the number of 90° plies increases, indicating that 90° plies are contributing to the formation of transverse cracks. Recalling that the specimens of the G6U1 plate are composed of completely unidirectional fibers, they do not allow for the formation of transverse cracking as much as the other two configurations, G6B1, and G6B2. Therefore, there is no significant change in the Poisson's ratio of each loading cycle for the specimen from the G6U1 plate, as seen in Figure 3.10(c). Figure 3.10(b) presents the Poisson's ratio of the specimen from G6B2 plate which has two off-axis plies. It is clear that, when off-axis plies are added to glass fiber reinforced composite, there is more deviation in the Poisson's ratio between subsequent cycles. The specimen from the G6B1 plate is more prone to transverse cracking and, therefore, it is expected that the difference between the Poisson's ratios of subsequent cycles should be largest for the specimen of G6B1 in comparison to the specimens from G6U1 and G6B2, as can be seen in Figure 3.10(a).

3.4 Concluding Remarks.

The measurement of Poisson's ratio of composite materials using different types of surface-mounted strain sensors has been reported in the open literature. There are also several studies that describe the embedding of FBG sensors into composite materials for the measurement of axial strains [13]. However, there is no systematic study that addresses the effect of stacking sequence on the extent of lowering of Poisson's ratio. The work presented in this paper presents a new sensing approach to monitoring the evolution of Poisson's ratio based on strain data acquired using embedded multi-axis fiber optic sensors with the capability to measure both axial and transversal strains at the very same location from single fiber optic cable simultaneously. To this end, composites specimens with three different stacking sequences were mechanically tested under both static and quasi-static tensile loading. For comparison and validation, the decreasing trend in Poisson's ratio as a function of the axial strain was monitored using embedded biaxial FBG sensor, biaxial strain gage and dual extensometer. The following conclusions were can be drawn from this study:

a) When changing the layer number of off-axis plies, the Poisson's ratio indicates a different evolution trend with respect to the applied strain. As the number of off-axis plies increases, a greater decline in the point by point evolution of Poisson's ratio is obtained;

b) Due to the formation of transverse cracks that hinder the effective transfer of axial load to the lateral direction and help the release of compressive strain, the transverse strain raises at a progressively smaller amount with increase in the applied load. This is the reason behind the decreasing trend in Poisson's ratio during the quasi-static tensile and quasi-static cyclic tension tests.

c) The embedded biaxial FBG sensors allow for tracking the variation of Poisson's ratio reliably and accurately;

d) The embedded biaxial FBG sensors are capable of capturing the damage state of composites through using reduction of Poisson's ratio as a damage index;

e) The embedded transverse FBG sensors are able to detect the effect of residual compressive strain relaxation on the measured lateral strain ;

f) The strain field in composite structures is sensitive to cracks, and the measured strain level is greatly influenced by the location, the gage length, and the type of the sensor;

g) Regardless of the difference in strain field acquired by three different sensor systems, it is shown that Poisson's ratio can be used as a reliable damage index since it is not based on the absolute value of the strain fields.

Acknowledgments

The authors gratefully acknowledge the funding provided by The Scientific and Technological Research Council of Turkey (TUBITAK) and Ministry of Science, Industry and Technology of Turkey for the projects 112M357 and 01307.STZ.2012-1, respectively.

Chapter 4

A Study on Correlating Reduction in Poisson's Ratio with Transverse Crack and Delamination Through Acoustic Emission Signals*

Abstract

During the uniaxial loading of fiber reinforced polymer (FRP) composites, Poissons ratio (ν_{xy}), which is a constant elastic property for isotropic materials, decreases significantly. Micro-damage created within FRP composites as a result of an applied stress causes this decrease. As the level of micro-damage increases, a greater level of reduction in Poissons ratio occurs. FRP composites, in general, 'show three main micro-damage types under uniaxial tensile loading, namely, transverse crack, delamination and fiber rupture. To determine micro-damage types which dominantly affects the relevant reduction in Poissons ratio, glass fiber reinforced cross-ply laminates with three different off-axis ply content are produced and then tested under a uniaxial tensile loading. The Acoustic Emission (AE) signals are concurrently recorded and grouped into three clusters in accordance with their frequency, which is either associated with transverse crack, delamination or fiber

*Appears in: C. Yilmaz, M. Yildiz, A study on correlating reduction in Poissons ratio with transverse crack and delamination through acoustic emission signals, Polymer Testing, Volume 63, 2017, Pages 47-53

rupture. The frequency based clustering of AE signal facilitates detailed investigation of delamination onset and effect of different micro-damage types on Poissons ratio. It is proven that stacking sequences with a higher number of transverse cracks and delaminations, quantified based on AE signals, show a greater reduction in Poissons ratio.

Keywords: Composite materials; Micro-damage formation; Poissons ratio; Acoustic emission;

4.1 Introduction

FRP composites show a significant decrease in their elastic properties (axial elastic modulus $E_{xx} = \sigma_{xx}/\epsilon_x x$ and Poissons ratio, $\nu_{xy} = \epsilon_{yy}/\epsilon_{xx}$, among others) when subjected to an axial strain until the fracture [5, 9]. Therefore, axial elastic modulus and Poisson's ratio which are measurable quantities using conventional sensor systems, lend themselves to monitoring the micro-damage state of composite materials. The reduction in these quantities is known to be associated with the accumulation of micro-damage created such as transverse crack, delamination and fiber rupture during the tensile loading of composite samples since these micro-damage types could significantly alter the elastic properties of the composite samples. In comparison to the elastic modulus, Poisson's ratio of composite materials reveals a greater level of reduction under uniaxial loading conditions [11]. This is related to the fact that during uniaxial loading, Poisson's ratio remains as a function of two-dimensional strain field which makes Poisson's ratio more sensitive to the accumulation of micro-damage within FRP composites in comparison with unidirectional elastic modulus which is only dependent on one dimensional strain field.

In this study, we endeavor to answer two questions by using the principle of Acoustic Emission (AE). First, which micro-damage type(s) are more dominant in the reduction of Poisson's ratio. Second, how a stacking sequence affects the delamination onset. The effects of thickness of laminate and thickness to width ratio on delamination onset, have been investigated in a series of papers for angle-ply laminates [18–20]. To the extent of our knowledge, there are not many studies on delamination onset in cross-ply laminates. AE has been used as a reliable method

to determine micro-damage types in FRP composites [16, 17, 21]. The micro-damage formation inside the composite materials causes initiation and propagation of transient elastic waves, which have been used to characterize the type and level of micro-damage in composite materials by using the features of transient elastic wave. The analysis of AE signals reveals broad range of information about micro and macro damage behavior of FRP composites as well as the damage types. In literature, several studies have been conducted to classify the micro-damage types and micro-damage initiation and progress for FRP composites using the AE method. For example, for glass fiber reinforced materials, crack propagation [22], and micro-damage mechanism [23] process have been investigated through analyzing AE signals. The initiation and propagation of transverse crack for carbon fiber reinforced polymer have been investigated by modal decomposition of AE signals [24]. Micro-damage types have also been classified by conducting spectral analysis on the acquired AE signals [16, 25].

In AE method, the piezoelectric resonant transducer sensors convert the detected transient elastic wave into the voltage output. The voltage output is affected by micro-damage source and material properties whereby micro-damage can be classified according to the features of the output signal. For example, it is a common practice to process the acquired AE signals in frequency domain, thereby enabling frequency based micro-damage classification such that transverse cracks, delaminations and fiber ruptures have low, intermediate and high frequency spectrum, respectively [17, 21]. To be able to associate the reduction in Poisson's ratio with the extent and types of micro-damage, we have designed and produced composite laminates with three different stacking sequences, namely, $[90/90/0]_s$, $[90/0/0]_s$, and $[0]_6$. We have mechanically tested the samples while concurrently recording AE signals, and axial and transversal strain fields. The reading of strains used in Poisson's ratio monitoring is achieved with an extensometer system. The effect of sensors on the strain reading has been already investigated in our previous study [26], which demonstrates that reduction in Poisson's ratio is equivalently well captured by extensometer, strain gage, and fiber Bragg grating (FBG) sensors. Each of these laminates under uniaxial tensile loading is expected to produce dissimilar level of micro-damage, to show different level of reduction in Poisson's ratio, and to possess dissimilar delamination onsets. In this study, AE signals are classified according to their weighted peak frequency (f_{wp}) feature to elucidate the micro-damage types that cause a reduction in Poisson's ratio. The micro-damage types are classified as transverse crack, delamination and fiber rupture, which are defined

as follows. Transverse cracks are created within off-axis plies which are perpendicular to loading direction, delamination is the separation of composite lamina from each other or resin, and fiber rupture is the fracture of individual/bundle of fibers parallel to loading direction. The experimental findings reveal that the level of reduction in Poisson's ratio and AE signals belonging to the transverse crack and delamination are well correlated for the three different lay-ups. It is shown that the level of reduction in Poisson's ratio increases with an increase in the number of AE signals associated with transverse crack and delamination. Moreover, delamination onset for different stacking sequences is investigated and results are presented and a relation between the delamination onset and number of off-axis plies observed. This study sheds light on micro-damage evolution and its corresponding effects on Poissons ratio through inspecting AE signals.

4.2 Experimental

4.2.1 Materials and Sample Preparation

Glass fiber reinforcement (E-glass stitched fabric) purchased from Metyx (Turkey) with a trade code of L300 E10B-0 consists of 283 gsm warp fibers (600 Tex), 37 gsm weft fibers (68 Tex) and 10 gsm stich (76 DTex). The glass fiber reinforcement is a unidirectional fiber where weft fiber acts as a base for stitching to preserve the orientation of longitudinal fibers during the knitting and makes the handling process easier. As a matrix material, Araldite LY 564 epoxy/XB3403 hardener system purchased from Hunstman (USA) is used. Vacuum-infusion method is employed to produce composite plates, which are then cured at 80°C for 15 hours. Three different composite plates with the stacking sequences of $[90/90/0]_s$, $[90/0/0]_s$, $[0]_6$ are manufactured and coded referring to the number of off axis fiber ply in each laminate, namely, S2, S1 and S0, respectively. All laminates have a thickness of between 1.7 and 1.8 mm. Tensile test coupons are cut and prepared out of these composite plates in accordance with ISO 527 standard and have a width of 25 mm, and other dimensions are shown in Figure 4.1.

4.2.2 Static Tensile Testing

Zwick Z100 universal testing machine with a load cell of ± 100 kN is used as a mechanical testing station. All static tensile tests are performed under displacement control with a constant crosshead speed of 2 mm/min. Longitudinal and transverse strains are measured by using Epsilon 3542 axial extensometer with a fixed gage length of 25 mm, and Epsilon 3575 transverse extensometer with a controllable gage length, respectively. Extensometers are excited with 10 V external voltages by National Instruments NI SCXI-1000 main chassis with NI SCXI-1520 card, and sampled at 100 Hz.

4.2.3 Acoustic Emission Setup

Two wide band (WD) piezo-electric sensors (Pico Miniature AE sensor, Physical Acoustics) are attached to each specimen with a hot silicon gun as shown in Figure 4.1 with a total 150 mm separation distance.

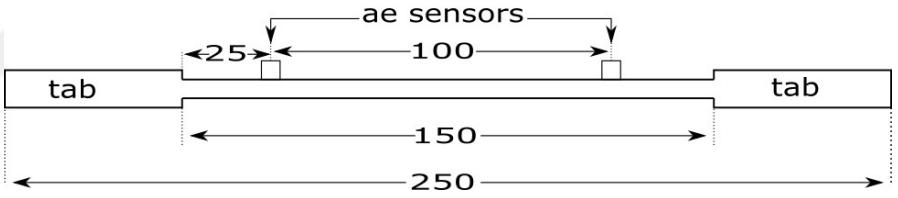

FIGURE 4.1: The schematic for the configuration of AE sensors on a tensile test specimen where dimensions are given in millimeters.

AE signals are recorded and post-processed according to the procedures given in Section 2.3.2.1 and Section 2.5, respectively. For this part of thesis, AE signals are correlated with micro-damage types using their f_{wp} feature in the frequency domain and amplitude in the time-domain. For the correlation of AE signals with micro-damage types, a second post-processing is not considered.

4.3 Results and Discussions

4.3.1 Clustering and Localization of AE Data

Figure4.2(a) yields a representative scatter plot of amplitude versus f_{wp} for cured epoxy resin. The signal cluster in the frequency range of 30-160 kHz is associated with the transverse cracks formed in the epoxy matrix. Figure 4.2(b) gives the scatter plot of amplitude versus f_{wp} for the composite material with the stacking sequence of $[90/90/0]_s$ wherein one can observe three different cluster regions corresponding to the frequency ranges of 30-160 kHz, 160-350 kHz, and 350-550 kHz, related to transverse crack, delamination, and fiber rupture, respectively.

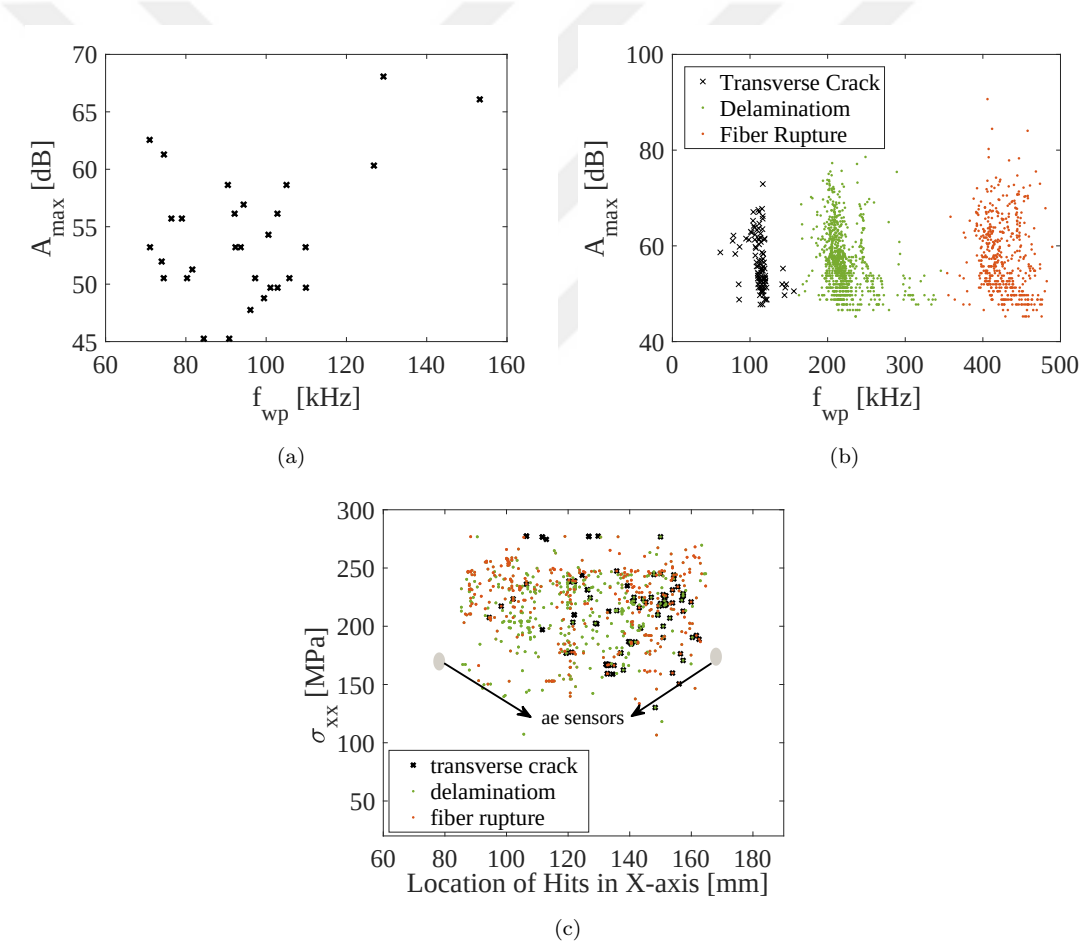

FIGURE 4.2: Representative plots of amplitude versus weighted peak frequency for cured neat epoxy resin (a), and composite sample (b), and the stress versus hit locations in x-direction (c).

Before the mechanical testing, the speed of sound (v_s) of S0, S1, S2 stacking sequences as well as the epoxy matrix is calculated for determining AE hits that

participate in events between two sensors using the pencil-lead breakage or the so-called Hsu-Nielsen source method [27]. The source locations of hits are determined using a linear location analysis based on known quantities; the speed of sound and arrival time of hits. For the analysis presented in this study, only the hits located between two sensors are considered, as shown in Figure 4.2(c). The of S0, S1, S2, and epoxy matrix are found to be 4257, 3807, 3449 and 1628 m/s, respectively. The decrease in the content of E-glass fibers in the direction of speed of sound measurement leads to a descent in the speed of sound, which can be associated with the higher value of elastic modulus of fibers in comparison to epoxy matrix, recalling that elastic modulus ($E = \rho * v_s^2$) is related to the speed of sound and density through a relation. Therefore, assuming a nearly constant density of composites with different stacking sequences referring to their fiber volume fractions tabulated in Table 4.1, the increase in the elastic modulus results in an increase in the speed of sound. Figure 4.2(c) also reveals that, the fiber rupture occurs more dominantly at higher stress levels. On the other hand, transverse crack and delamination spread over the whole stress domain.

4.3.2 Mechanical Response of Laminates

During the execution of quasi-static tensile tests, the applied load, the axial and transverse strains, and acoustic emission signals are simultaneously recorded. By using the recorded load and strains data, mechanical properties of each lay-up are calculated and tabulated in Table 4.1. Burn-out test is carried out to determine fiber volume fraction of composite plates and results are also given in Table 4.1. Table 4.1 shows the strength and elastic modulus of the specimens increase with the increase in the amount of 0° fibers along the loading direction, as expected. Figure 4.3(a) and (b) in the given order illustrate representative graphs for stress versus strain and Poisson's ratio versus axial strain. It is observed that specimens with higher number of off-axis ply experience larger level of reduction in Poisson's ratio.

In literature, transverse cracks are considered to be the main micro-damage type that is responsible for the reduction of elastic properties (i.e., Poisson's ratio and elastic modulus) [28], excluding other possible effects such as delamination and fiber rupture. We think that this assumption stems from the fact that transverse cracks are easy to visualize and track with microscopic and imaging methods in

TABLE 4.1: Mean (standard deviation) of mechanical properties.

	S0 $[0]_6$	S1 $[90/0/0]_s$	S2 $[90/90/0]_s$
Strength (σ_u)	666(50.6)	480(37)	273(4.9)
Elastic Modulus(E_{xx}) (GPa)	29.44(0.75)	20.9(0.67)	16.21(0.62)
Fiber Volume Fraction (v_f) (%)	42.5	41.9.1	44.1
Maximum Poisson's ratio	0.268(0.03)	0.140(0.03)	0.116(0.02)
Minimum Poisson's ratio	0.217(0.02)	0.082(0.02)	0.052(0.01)
Percent change (%) in Poisson's ratio	19(10.2)	41.5(6.18)	53.5(16.34)
Weight percentage of off axis plies	11	36	61

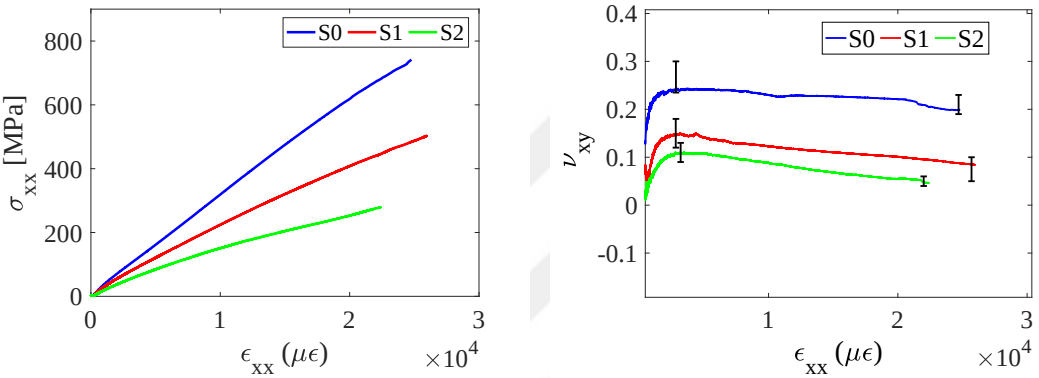

FIGURE 4.3: Representative curves, (a) Stress-strain curves, and (b) Poisson's ratio-strain curves.

comparison to delamination and fiber ruptures. However, with the concurrent usage of non-destructive testing methodologies such as AE technique (that enables the concurrent monitoring of the micro-damage and discrimination of micro-damage by their frequency content in composites subjected to mechanical loading) with the variation of elastic properties, one can also scrutinize the effect of delamination and fiber rupture on the reduction of elastic properties in addition to transverse cracks.

The S0 stacking sequence is predominantly composed of unidirectional fibers, but has 11 % off-axis fibers in the reinforcement as previously stated in part 4.2.1. S1 and S2 laminates have two and four off-axis plies corresponding to 36 % and 61 % of the total weight of the reinforcement, respectively. As can be seen from Table 4.1, there is a direct correlation between the amount of off axis plies and the percentage reduction in Poisson's ratio such that as the number of off-axis plies increases, so does the reduction in Poisson's ratio. The off axis plies promotes the

formation and propagation of micro-damage within the matrix, which hinders the axial load to be transferred effectively along the lateral direction, resulting in a decrease in the lateral strain [26].

4.3.3 Number of Hits for Different Micro-Damage Types

As stated previously, AE signals are classified according to their relevant f_wp that are associated with transverse crack, delamination, and fiber rupture as shown in Figure 4.2(b). AE signals with lower f_{wp} (30-160 kHz), middle f_{wp} (160-350 kHz), and higher f_{wp} (350-550 kHz) are considered to be transverse cracks, delamination and fiber rupture. AE signals corresponding to these (referred to as clusters) were analyzed in terms of the number of AE hits to examine which micro-damage type dominantly affect the level of reduction in Poisson's ratio.

The average numbers of hits (summation of number of hits for each specimen divided by the total specimen number) in each cluster (equivalently micro-damage type) for three different stacking sequences are calculated as,

$$\hat{H}_t^s = \sum_{j=1}^{j=N} H_{t,j}^s / N \tag{4.1}$$

where $\hat{H}_t^s$ of th specimen is the cumulative hit number which is calculated through summing all hits for the th micro-damage type (micro-damage types are transverse crack, $t = tr$, delamination, $t = d$ and fiber rupture, $t = fr$) and for each specimen and N is the total number of specimens tested. The total number of specimens (N) for $S0$, $S1$ and $S2$ are 3, 5, and 3, respectively. Here, the superscript s corresponds to stacking sequence such that $s = S0$, $S1$ and $S2$. Figure 4.4(a) demonstrates the average numbers of hits for all stacking sequences and micro-damage types ($\hat{H}_t^s$). The S0 plate yields the largest number of signals for fiber rupture ($\hat{H}_{fr}^{S0}$) and the least number of signals for transverse crack ($\hat{H}_{tr}^{S0}$). Additionally, for S0 stacking, both $\hat{H}_{tr}^{S0}$ and $\hat{H}_d^{S0}$ are the smallest of all the stacking sequences due to its highest amount of uni-directional fibers.

The relationship among the hits of all stacking sequences for transverse crack is as follows: $\hat{H}_{tr}^{S2} > \hat{H}_{tr}^{S1} > \hat{H}_{tr}^{S0}$. It is clearly seen that as the number of off-axis plies increase, there is a discernible rise in the AE hits of the cluster corresponding to transverse cracks. For the stacking sequence having the largest number of AE

hits for the cluster corresponding to the transverse crack, there is a greater level of reduction in Poisson's ratio, which accounts for the effect of transverse cracks on the reduction in Poisson's ratio. The number of signals for delamination has the following ordering: $\hat{H}_d^{S2} > \hat{H}_d^{S1} > \hat{H}_d^{S0}$. It is worth noting that increasing the number of off-axis plies brings about a rise in the number of delamination signals, revealing that the reduction in Poission's ratio becomes larger in laminates with stacking sequence prone to the formation of delamination.

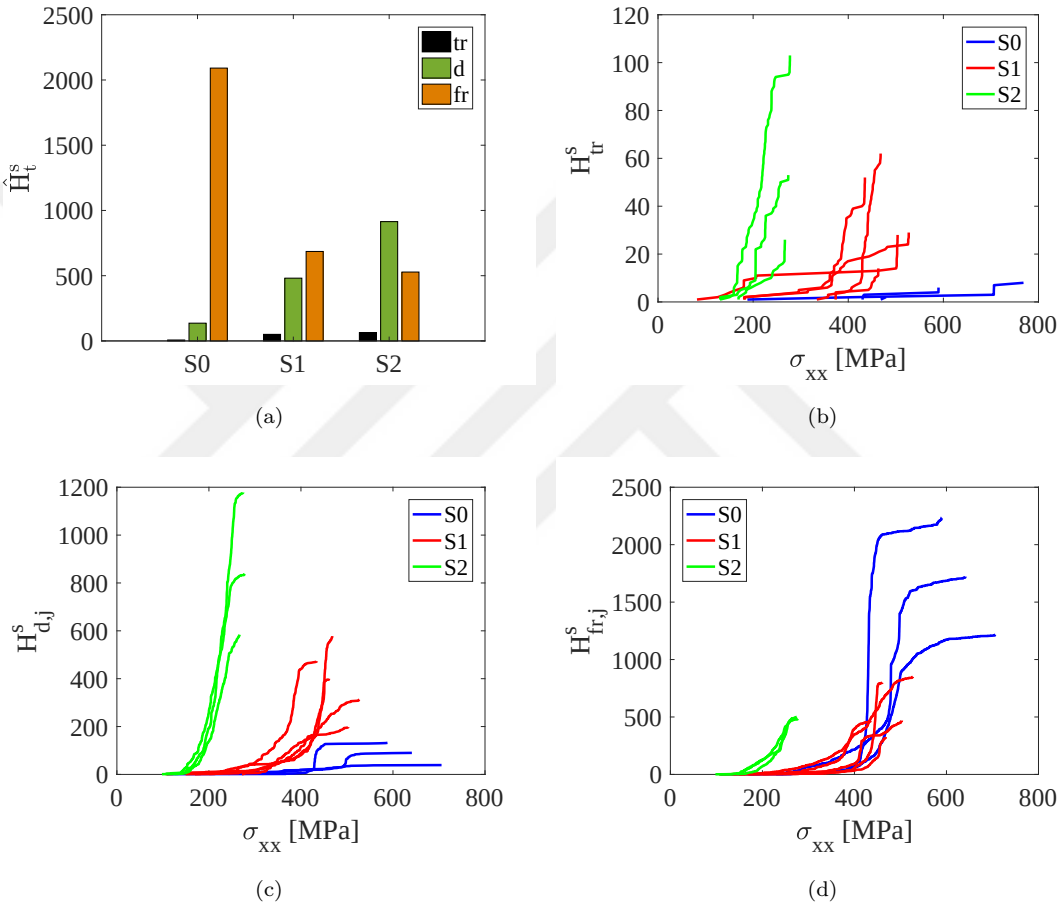

FIGURE 4.4: The average hits for three micro-damage types and stacking sequences ($\hat{H}_t^s$), and (b-d) cumulative hits of transverse crack ($H_{tr,j}^s$), delamination ($H_{d,j}^s$), and fiber rupture ($H_{fr,j}^s$), respectively for stacking different sequences and test specimens.

It is noted that the level of reduction in Poisson's ratio also follows the same ordering. For the fiber rupture signals, the following ordering $\hat{H}_{fr}^{S0} > \hat{H}_{fr}^{S1} > \hat{H}_{fr}^{S2}$ can be seen in Figure 4.4(a). As the amount of unidirectional fiber content decreases in a given order of $S0$, $S1$ and $S2$, a lower number of fiber rupture signals was acquired as AE signal hits (Figure 4.4(a)). The order in fiber rupture signals is inversely related to reduction in Poisson's ratio. Since the decrease in

the Poisson's ratio is related to micro-damage accumulation, fiber ruptures can not affect the reduction in Poisson's ratio. These results clearly indicate that when the number of off axis plies increase, the number of transverse cracks and delamination signal increases, and so does the level of reduction in Poisson's ratio.

Cumulative number of transverse cracks ($H^s_{tr,j}$), delamination ($H^s_{d,j}$), and fiber rupture ($H^s_{fr,j}$) AE hits with respect to applied stress for the individual test coupons that were extracted from three stacking sequences can be seen in Figure 4.4(b), (c), and (d), respectively. Although the test coupons from S0 plate has the highest strength, it indicates the lowest $H^{S0}_{tr,j}$ and $H^{S0}_{d,j}$ as seen in Figure 4.4(b), and (c), respectively. This result indicates that the number of transverse cracks and delamination is not dependent on the strength, and instead relies on the fiber orientation. Moreover, S0 plate is the richest in terms of on-axis plies which therefore reveals highest $H^{S0}_{fr,j}$ among all fiber stacking architecture as seen in Figure 4.4(d). The comparison of Figure 4.4(b), (b) and (d) also indicates that transverse cracks, delamination and fiber rupture can be formed concurrently during the loading of test specimens.

4.3.4 Delamination Susceptibility

To be able to address the effect of free edge delamination and transverse crack induced internal delaminations on the reduction in Poissons ratio, we have also looked into the free edge delamination tendency of the studied stacking sequences. Free edge delamination is a well-known phenomenon for FRP laminates [29]. In-plane normal strain results in interlaminar normal stresses (σ_{zz}) at the free edges in cross-ply laminates due to mismatch in Poissons ratio between the 90° plies and 0° plies. If 90° plies are on the surface and 0° plies constitute the inner layers, interlaminar compression stress ($-\sigma_{zz}$) at the free edges is to be seen, as depicted in Figure 4.5. On the contrary, 0° layering plies on the surface and 90° plies on the inside generates interlaminar tensile stress (σ_{zz}). Free edge delamination is initiated at lower stress values when interlaminar tensile stress is present while interlaminar compression stress postpones delamination [30]. Naturally, it is expected that stress level for the onset of the edge delamination should be the highest for S2, moderate for S1 and the lowest for S0. Among the stacking sequences analyzed in this study, the relative stress level ($\sigma_r = \sigma_o/\sigma_u$) for the onset of delamination for S2

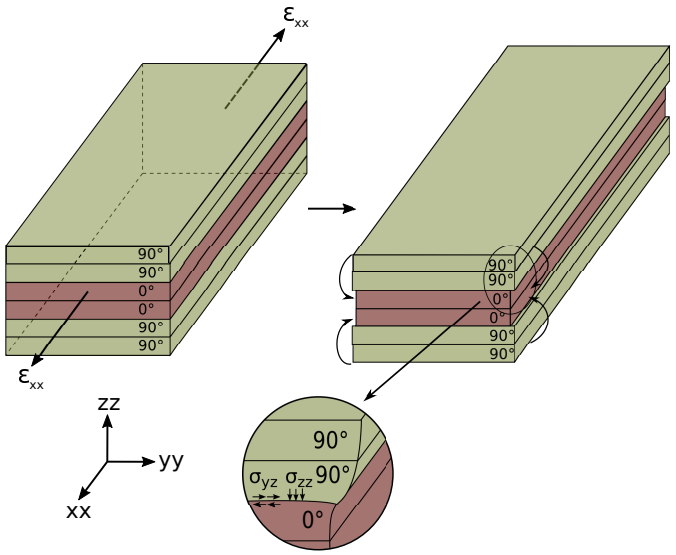

FIGURE 4.5: Interlaminar compression stress for surface 90° dominated laminate on the free edge.

is calculated to be highest σ_o where is the stress level at which the first delamination signal is recorded and σ_u is the ultimate tensile strength of the laminate such that σ_r for S2, S1, S0 are respectively 0.37, 0.158, and 0.155. Although S2 laminate has comparatively the largest resistance to edge delamination and the highest delamination onset ratio, σ_r, it includes the greatest amount of delamination hits detected by AE as seen in Figure 4.4(a) among all laminates. The results clearly reveal that transverse cracks trigger and facilitate the formation of delamination since S2 stacking sequence is more prone to transverse crack generation due to its higher content of off axis plies. In summary, transverse cracks and delaminations are highly coupled micro-damage types which cause notable reduction in Poisson's ratio through combined and synergetic effect.

4.3.5 Concluding Remarks

The uniaxial tensile stress is applied to test coupons having three different stacking sequences to investigate the level of reduction in Poisson's ratio using in-situ AE signals acquired by an AE setup. The experimental results indicate that Poisson's ratio reveals a non-linear increase followed by a linear decrease for three different fiber lay-ups, namely, $[90/90/0]_s$, $[90/0/0]_s$, and $[0]_6$ during the static tensile testing. It is shown that the bigger the number of off-axis plies, the larger the reduction in Poisson's ratio. The factors behind the reduction in Poisson's ratio are investigated in terms of micro-damage evolution principles using the AE signals.

These signals are classified with respect to their weighted peak frequencies (f_{wp}), and three different clusters, corresponding to transverse cracks, delamination and fiber rupture, were observed. The following important conclusions are derived from this study:

a) The level of reduction in Poisson's ratio is a lay-up dependent quantity and rises with the increase in the number of off axis plies.

b) The number of AE hit associated with transverse cracks and delamination indicates notable rises with the increase in the number of off axis plies, implying an obvious relationship between the level of reduction in Poisson's ratio, and transverse cracks and delamination.

c) It is shown that transverse cracks trigger and facilitate the formation of delamination such that although $[90/90/0]_s$ stacking sequence is of a tendency to suppress the occurrence of delamination, it has the largest number of delamination signal.

d) Since the matrix material distributes the load across the fibers, if any micro-damage occurs within the matrix such as delamination or transverse crack, the applied axial load will not be smoothly transferred to transverse direction by matrix, hence causing a reduction in transverse strain which is the main reason responsible for reduction in Poisson's ratio.

Acknowledgments

The authors gratefully acknowledge the funding provided by The Scientific and Technological Research Council of Turkey (TUBITAK), and Ministry of Science, Industry and Technology of Turkey for the project, 112M357, and 01307.STZ.2012-1, respectively.

Chapter 5

A Hybrid Damage Assessment for E-and S-Glass Reinforced Laminated Composite Structures under In-Plane Shear Loading*

Abstract:

Micro-damage initiation and accumulation in two different Glass Fiber Reinforced - E-glass and S-glass- Laminated Composite Structures (LCS) subjected to in-plane shear stressing are monitored with Acoustic Emission (AE) and thermography methods. AE signals caused by micro-damage formation are graphed as a scatter plot of Weighted Peak Frequency (WPF) versus Partial Power 2 (PP2) features and clustered using the K-means algorithm with Bray Curtis dissimilarity function thus resulting in three different well-separated clusters. Each of these clusters corresponds to different micro damages, i.e., transverse cracks, delaminations, or fiber ruptures. It is observed that the E-glass reinforced LCS has higher numbers of AE hits. Thus, the total amount of micro-damage incurred as well as the average temperature change measured by thermography is higher for the E-glass reinforced LCS. It is shown that due to the curing induced residual tensile stress in E-glass reinforced LCS, the initial formation of delamination in E-glass reinforced LCS starts at higher load level. Under the applied shear load, a significant reduction

*Appears in: C. Yilmaz, C. Akalin, I. Gunal, H. Celik, Murat Buyuk, A. Suleman, M. Yildiz, A hybrid damage assessment for E-and S-glass reinforced laminated composite structures under in-plane shear loading, Composite Structures, Volume 186, 15 February 2018, Pages 347-354

in in-plane shear modulus is observed both for the E-glass and S-glass-reinforced LCS where the E-glass reinforced LCS shows greater reduction. The decrease in in-plane shear modulus is attributed to micro-damage accumulated in the LCS.

Keywords: Shear modulus; reduction; Iosipescu Test; laminated composites

5.1 Introduction

The usage of LCSs has increased in engineering applications over the past decade, such as wind turbine blades, aircraft and naval components. The reason behind this increase is due to their high specific strength and stiffness compared to metallic materials. LCSs help to reduce the total weight of vehicles hence enabling them to cover long distances given the same amount of fuel or create less green-house gases. To be able to use LCSs in structural applications reliably without any abrupt failure, a detailed study on the reduction in engineering elastic constants of LCSs associated with micro-damage initiation and accumulation must be carried out. In literature, one may find several important studies on the micro-damage induced reduction in mechanical properties of LCSs under axial loading such as axial modulus and Poissons ratio. For instance, Highsmith et al. [4] studied the effect of transverse crack on the axial stiffness reduction under the uniaxial quasi-static tension and tension-tension fatigue. The behavior of Poissons ratio under tensile loading was analyzed in references [5, 6, 11, 31, 32] wherein results indicated that formation of transverse crack causes apparent reduction in Poissons ratio. Different sensor systems were also utilized to measure strain from the surface and interior of LCSs with the aim of calculating Poisons ratio reduction and studying the effect of sensor types on the Poissons ratio measurement [26].

However, a few studies can be listed as to the reduction in in-plane shear modulus owing to the micro-damage initiation and accumulation under loading despite the fact that the in-plane shear modulus is among very important mechanical properties, which is needed for predicting the structural response of LCSs under mechanical loading. Given that in-plane shear modulus can be measured with special fixtures such as Iosipescu shear fixture (ASTM D5379/D5379M 12), in literature, research on shear loading mainly deals with addressing the drawbacks of the test fixture, the notch type of test specimens and the finite element analysis of test coupons [33–35]. Odegard et al. [36] compared the feasibility of Iosipescu test with

10° off-axis test for measuring the in-plane shear modulus of unidirectional carbon fiber reinforced LCS and concluded that both tests yield a very similar value. Han et al. [37] evaluated frame test with respect to the Iosipescu test, and deduced that the Iosipescu test delivers a more accurate result for shear properties of laminates than that of the frame test. Pierron et al. [38] addressed the reliability of in-plane shear strength measurement with the Iosipescu test and found out that the shear strength measured by the Iosipescu shear test is smaller than the one determined by 10o off-axis test. Sun et al. [39] investigated specimens with the V-notch and Round-notch in Iosipescu testing and arrived at a conclusion that Round-notch is more favorable. Tew et al. [34] studied the fixture and specimen interaction in the Iosipescu test and proposed two different types of fixtures, namely, pivoting and rounded load surface. Unlike the research in literature dedicated to determining optimum test specimen configuration, and to the investigation of test fixture and test type, there are limited number of studies which have addressed the evolution of the shear modulus reduction through using Iosipescu testing fixture. Salavatian et al. [40] considered the effect of transverse cracking on the reduction in in-plane shear modulus, excluding the possible effects of other micro-damage types such as delamination and fiber rupture among others. Salavatian et al. [41] also modeled the effect of internal frictions between the surfaces of transverse cracks on the reduction of in-plane shear modulus. Differently, Melin et al. [33] reported that the reduction in in-plane shear modulus is not due to the micro-damage (i.e., transverse cracking, delamination, or fiber rupture) accumulation, rather, it is due to the viscous deformation and creep in the matrix phase.

To be able to understand the effect of micro-damage formation on the in-plane shear modulus of LCSs, in this study, acoustic emission (AE) method is used since it provides useful outputs that can be readily processed to distinguish possible damage generation mechanisms (fiber rupture, delamination, transverse cracking), which are particularly important for failure assessment of composite materials. AE technique uses piezo-electric sensors which are sensitive to short and weak transient waves released by micro-damage formation. Several studies have employed AE method during the tensile test of LCSs where transient waves generated by micro damage formations are recorded and classified [42, 43]. A variety of classification procedures can be found in literature which use different features of waves such as rise time, peak amplitude, peak frequency and weighted peak frequency [44]. Among these features, the usage of weighted peak frequency (f_{wp}) with the unsupervised K-means algorithm is the most promising one.

In addition to AE method, due to the significance of the micro-damage formation on the mechanical properties of LCSs, several studies used the concept of thermography and measured surface temperature of composite specimens with an IR camera to evaluate the damage state of LCS under fatigue loading. For example, Genest et al.[45] employed IR camera for detecting the disbonding area between a composite repair patch and aluminum host material under tension-tension fatigue. Liu et al. [46] proved that the thermography can be an effective way to determine the damage evaluation of carbon-fiber/SiC-matrix composites under the tension-tension fatigue. Naderi et al. [47] also showed that the thermography can be used to reveal fatigue stages of glass/epoxy composite under bending fatigue. Montesano et al. [48] assessed the damage states of woven carbon fiber/epoxy composites with thermography subjected to uniaxial in-plane tensile quasi-static and fatigue loading. The thermography based damage monitoring and assessment is not limited to composites and have been used for metallic materials as well. For instance, Crupi [49] used IR camera to measure the surface temperature of steel and aluminum under high cycle fatigue and showed that the temperature increment as a result of the heat dissipation can be used as a life parameter. Fargione et al. [50] showed that temperature measured by the IR camera can reveal the damage state of steel and help the rapid determination of fatigue curve for steel.

Although, there are numerous studies on damage evaluation with AE method and thermography under different loading conditions (i.e., static and fatigue), and on the optimization of the shear testing of the composite, to the best of the authors knowledge, there is no combined damage assessment study using AE and thermography methods to study the reduction in in-plane shear modulus of LCS under the shear loading. In this study, we have monitored the initialization and accumulation of different micro-damage types in two different LCS under shear loading, and investigated the effect of micro-damage on the shear modulus reduction. The LCSs are composed of S-glass and E-glass reinforcements. The micro-damage monitoring is accomplished by piezo electric sensors connected to the AE streaming hardware. The stress waves released by the micro-damage are converted to AE signals by piezo electronic sensors. Thereafter, a comprehensive classification of AE data is achieved by K-means algorithm which uses the Bray-Curtis dissimilarity function for assigning data points to the relevant cluster. Three different clusters are formed, which corresponds to transverse cracks, delaminations, and fiber ruptures. The temperature change on the surface of the specimens is monitored by the IR camera to associate the damage type and accumulation with

temperature increase. The combined usage of AE and thermography in studying the behavior of LCSs under in plane shear loading enables us to elucidate the effect of micro-damage initiation and accumulation on the shear properties as well as shear modulus reduction.

5.2 Methodology

5.2.1 Materials and Sample Preparation

Two different glass-fiber reinforcements (S-glass and E-glass woven rowing fabric with 600 gsm areal weight with epoxy vinyl ester compatible sizing agent) are purchased from Metyx, Turkey, and then used to manufacture composite plates through using vacuum infusion method. As a matrix material, a room temperature curing epoxy vinyl ester resin (Derakane 8084, Ashland Inc.) is chosen. Curing process lasts 12 hours at room temperature without post curing. The curing process of epoxy vinyl ester resin is exothermic, leading to a temperature increase up to 135°C. The produced composite plates comprise 8 layers of glass-fabrics. The plates are cut with a water-cooled diamond saw in dimensions given in Figure 5.1 in accordance with ASTM D 5379 standard. Specimens have thickness in the range of 4.2 - 4.7 mm. The V-notch grooves are machined with vertical milling machine. Thereafter, sides of specimens are grinded and rosette type strain gages acquired from Micro Measurement with a code of CEA-06-187UV-350 are applied to the front surface of test specimens as seen in Figure 5.1. The fiber volume fraction for S-glass and E-glass reinforced LCS are measured to be %40 and %42, respectively.

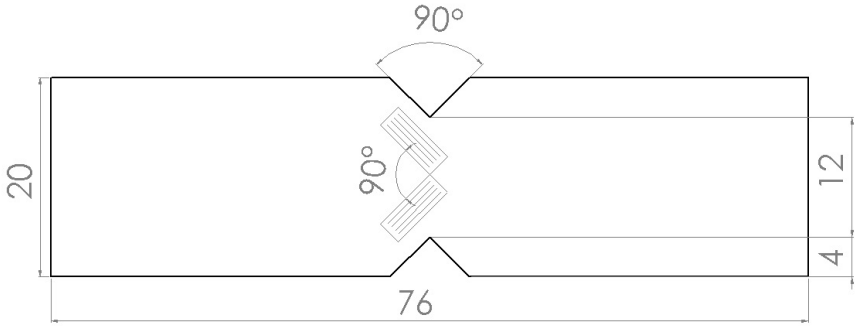

FIGURE 5.1: Dimensions of Iosipescu test specimen in mm.

5.2.2 Mechanical Testing

All in-plane shear tests are performed by using Instron 8801 UTM (Universal Testing Machine) combined with 8800MT digital controller. Instron 8801 UTM is equipped with a Dynacell load cell of ± 100 kN. Specimens are installed into the Iosipescu test fixture installed on the lower jaws of the UTM. Thereafter, point contacts are attached to the test fixture to prevent the twisting and bending of test specimens. An Iosipescu fixture with V-notch shear specimen can be seen in Figure 5.2(a). Strain-gage leads are mounted on electrical adapters connected to the strain channel on the test machine. A preload of 40 N is applied to all specimens to enable the proper contact of test apparatus with the load frame. In-plane shear test is performed under the constant crosshead-displacement of 2 mm/min. Bluehill 3 software is used to control the test machine as well as stress-strain data acquisition. Specimens are divided into two groups, namely, with and without a strain gage, because strain gage covers whole V-notch region thereby concealing the view of the IR camera. From each of two different LCSs, six specimens are tested, three of them are used in IR imaging and AE measurement, and remaining three are used in shear modulus measurement. To prevent Iosipescu shear fixture from getting damaged, all tests are terminated when the strain level of $2x10^4\mu\epsilon$ is reached.

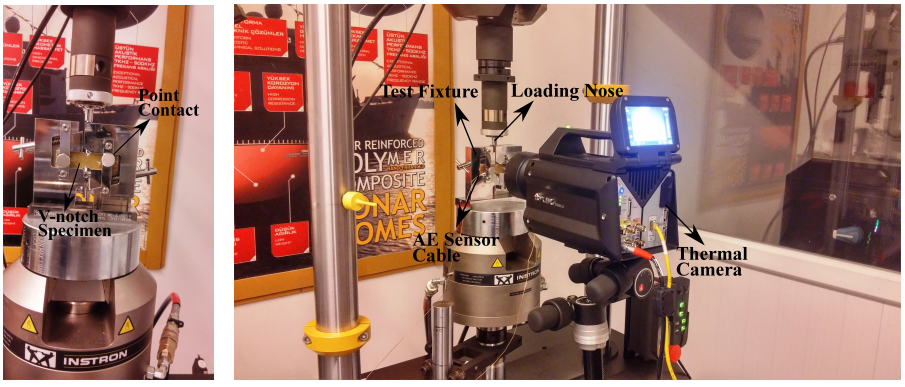

(a) (b)

FIGURE 5.2: (a) A close-up view of Iosipescu test fixtures with V-notch specimen, (b) picture of experimental set-up.

5.2.3 Acoustic Emission and Thermography

Once AE signals are recorded and post-precessed according to Section 2.3.2.1 and Section 2.5, respectively, the $PP2$ and f_{wp} are used in the K-mean clustering to associate the waveforms with micro-damage types, namely, transverse crack, delamination or fiber rupture. In Figure 5.3(a) and (b) are given representative power spectra of three microscopic damage mechanism namely, transverse crack (tr), delamination (d), and fiber rupture (fr) in S-glass and E-glass reinforced LCSs, respectively. It is seen that spectrum of each micro-damage mechanisms reveals different patterns. When $PP2$ and f_{wp} are graphed as a scatter plot, three data groups are formed as seen in Figure 5.4, where each group corresponds a different micro-damage type (transverse crack, delamination, and fiber rupture). An appropriate and reliable clustering algorithm is required to associate data points on transition zones or boundaries of data scatters to these groups correctly.

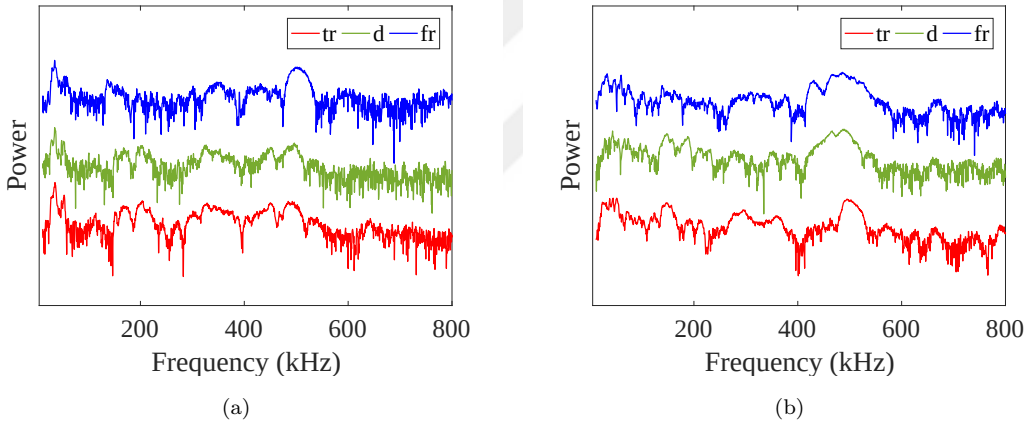

FIGURE 5.3: Power spectra of matrix cracking, delamination, and fiber rupture in; a) S-glass, and b) E-glass laminated composite structure.

For the classification, the hits (AE signals created by stress waves) only originated between two sensors are utilized. The classification of hits is performed by using an open-source software, Elki [51]. K-means algorithm is chosen to classify and relate the hits to the micro-damage types, i.e., a transverse crack, delamination, or fiber rupture. In K-means algorithm, the cluster number (k) is a user defined variable based on the visual inspection of scatter plot of f_{wp} versus PP2 as seen in Figure 5.4, and equal to three in this study. K-means clustering algorithm starts with three randomly chosen initial centroids in the $f_{wp} - PP2$ data sets. As the algorithm runs, the distance between these three clusters and a given data point is computed, and then, the given data point is assigned to the one of these three

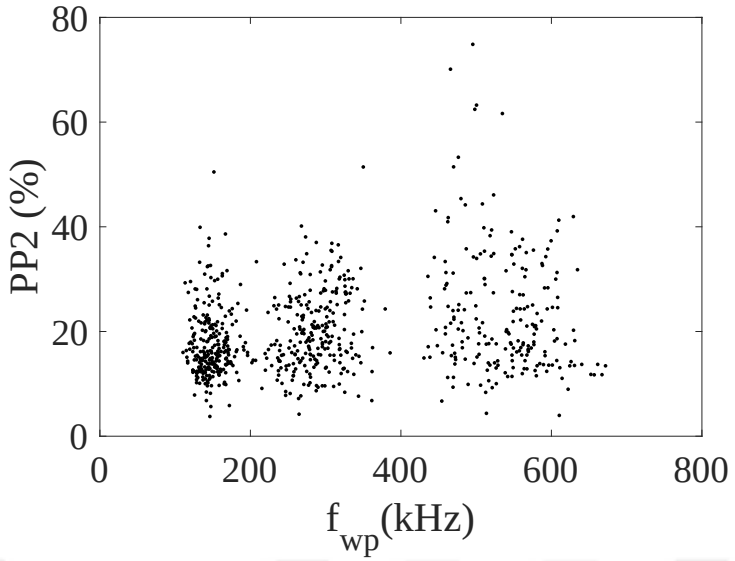

FIGURE 5.4: A representative f_{wp} versus PP2 scatter of a E-glass sample.

clusters with the smallest distance. The centroid of the data point added cluster is updated. This process continues until propping all the remaining data points. Clustering with K-means algorithm is an iterative process and continues until the centroids of three different clusters are converged. For a standard K-means clustering, Euclidean distance between the cluster centroid and data point is used to determine the similarity of features, namely, f_{wp} and $PP2$ [17, 52]. However, since Euclidean distance (d_E) is a metric measure, it is sensitive to the numerical magnitudes of features due to the square root of the sum of squared differences $d_E = \sqrt{(x_j - x_i)^2 + (y_j - y_i)^2}$ where the variables x and y correspond to f_{wp} and $PP2$ in the given order, and the subscripts i and j indicate the centroid of cluster and data points, respectively. For a successful K-means clustering, numerical magnitudes of features need to be normalized or an appropriate dissimilarity function should be used to eliminate the effect of the numerical magnitudes of features on the reliable association of data points to the predefined clusters. To this end, a non-Euclidean distance known as Bray-Curtis dissimilarity function (d_B) is used, $d_B = (|x_j - x_i| + |y_j - y_i|)/(x_j + x_i + y_j + y_i)$. This dissimilarity function is one of the most well-known ways for quantifying the similarity or difference between samples due to being less sensitive to the numerical magnitudes of features.

Surface temperatures of Iosipescu specimens are measured with an Infrared (IR) Camera with a model of FLIR X6580sc. The IR camera with 50-mm lens is placed at approximately 40 cm away from the test specimens as shown Figure 5.2(b) to obtain clear images. The IR camera is used in this study can measure temperature

from 20°C to 3000°C with the reading accuracy of 1 %. The resolution of camera is $640x512$ pixels. The sampling rate of 10 frame/s is chosen to obtain images which are then analyzed using a software, FLIR ResearchIR Max.

5.3 Results and Discussion

5.3.1 Reduction in In-Plane Shear Modulus

Iosipescu shear test can provide the shear strength, shear modulus and shear strain of composite materials in different planes of interest. In this study, it is mainly used to monitor the variation of in-plane shear modulus of two different composite structures with E-glass and S-glass reinforcements under the shear loading. Figure 5.5(a) and (b) respectively give in-plane shear stress-strain curves and the variation of normalized shear modulus for E-glass and S-glass reinforced LCS where G_{12}^0 in the figure is the maximum value of shear modulus calculated from entire stress-strain data set.

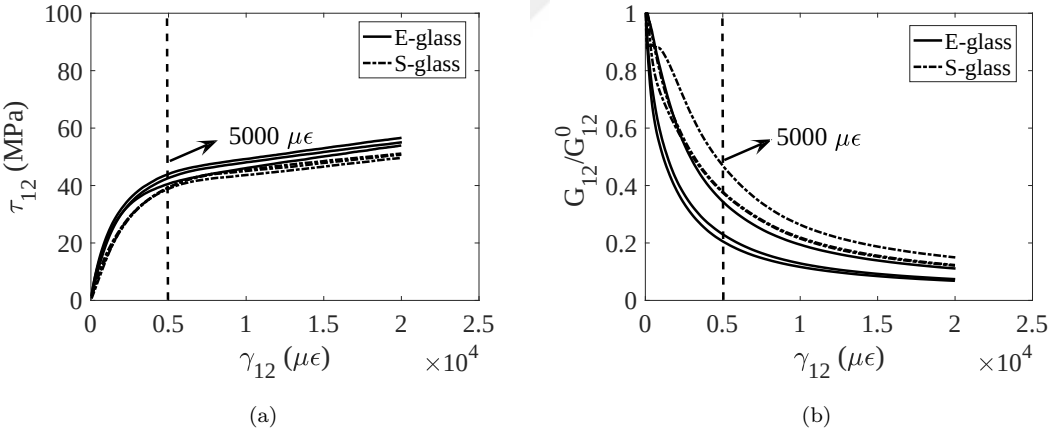

FIGURE 5.5: (a) In-plane shear stress-strain curves for E-glass and S-glass reinforced LCS, (b) The normalized behavior of shear modulus for E-glass and S-glass reinforced LCS.

The constituents of LCSs used in this study namely, fiber reinforcement (E-glass fibers and S-glass) and matrix (a thermosetting resin) materials have brittle failure mechanics. However, it is important to note that despite the brittle nature of the matrix and reinforcing materials, in-plane shear stress-strain diagrams of tested LCSs show a ductile-like behavior rather than a brittle-like one. The reason behind the ductile-like behavior is the high amount of deformation in the V-notch region

compared to rest of specimens. As the load on the test sample increases, the V-notch region is populated by micro-damages (transverse cracks, delamination, and fiber rupture), which grow in size and spread over the whole V-notch region. The formation and accumulation of micro-damages creates a macroscopically visible damage zone (white colored V-notch region) as shown in Figure 5.6 . Some cracks in this damage zone extend beyond V-notch region, which are marked by circles in Figure 5.6. When a micro-damage saturation point is reached (marked with the dashed vertical line in Figure 5.5(a)), which means that whole V-notch region is covered by micro-damages as shown in Figure 5.6, LCS loses its load carrying capacity as can be inferred from Figure 5 5.5(a) where the stress increases with a smaller slope after 5000 $\mu\epsilon$ for both types of LCSs. The decrease in the slope of stress-strain curve marks the beginning of larger deformation due to the high damage density in the V-notch region where the material starts revealing a ductile-like behavior. The concentration of damage in a small area where the in-plane shear modulus is measured causes a significant amount of reduction in the in-plane shear modulus as can be seen in Figure 5.5(b). Although both laminates show nearly similar linear in-plane shear stress-strain behavior up to the 5000 $\mu\epsilon$ (which is evident in Figure 5.5(a)), the decrease in the shear modulus for the E-glass and S-glass reinforced LCS up to 5000 $\mu\epsilon$ is notably different. The average reduction in in-plane shear modulus for S-glass and E-glass reinforced LCS is 60 % and 74 %, respectively as seen in Figure 5.5(b). Besides, the shear modulus of E-glass reinforced LCSs reduces notably faster than that of S-glass reinforced LCSs, hence indicating that damage formation and accumulation is much easier in E-glass reinforced LCSs.

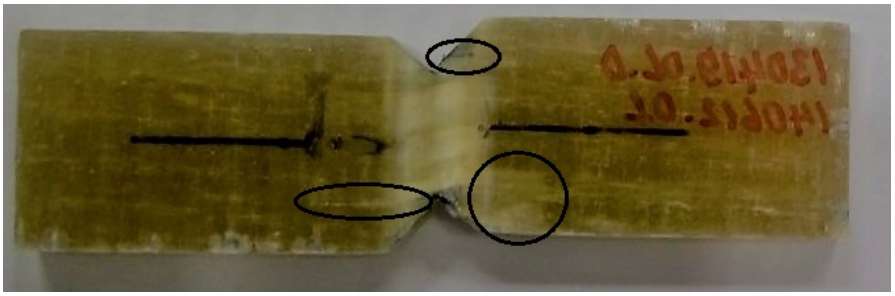

FIGURE 5.6: A tested Iosipescu shear specimen.

5.3.2 Acoustic Emission of Laminates

Here, we have presented the results of AE emission study on identifying and quantifying micro-damage initiation, total micro-damage accumulations, and the effect of different micro-damage types on the in-plane shear modulus of E-glass and S-glass fiber reinforced polymeric composites under the in-plane shear stress. The AE signals for two different laminates are clustered with K-means algorithm and representative results from each of the laminates are presented in Figure 5.7(a) and (b). Knowing that each micro-damage type causes a signal with different f_{wp} such that low, moderate and high values of f_{wp} represent respectively transverse crack, delamination, and fiber rupture [16, 53], the results given in Figure 5.7(a) and (b) indicate three well-distributed signal clusters which can be associated with transverse crack, delamination, and fiber rupture. Clustering the data sets reliably is very critical to be able to correctly analyze the effect of accumulation of different micro-damage on LCSs. Small standard deviation in means of f_{wp} features given in Table 5.1 indicates that the K-means algorithm with Bray-Curtis dissimilarity function can accurately cluster the signals.

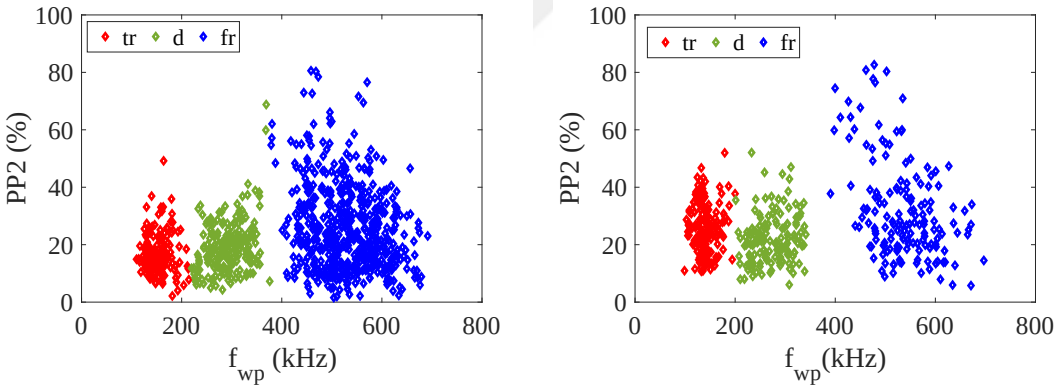

FIGURE 5.7: Representative K-means result for laminates, (a) E-glass reinforced, (b) S-glass reinforced.

TABLE 5.1: Mean and standard deviation (Stdev %) of centroids in f_{wp} axis for E-glass and S-glass reinforced LCS.

Reinforcement type	E-glass centroids			S-glass centroids		
Micro-damage type	tr	d	fr	tr	d	fr
Mean of 3 samples	168.1	276.7	532.6	155.8	267.7	521.4
Stdev (%)	4.3	3.1	1.8	5.8	1.1	0.9

To compare the average number of different hits in the S-glass and E-glass reinforced LCS, Equation 5.1 is considered and results are presented in Figure 5.8 as a bar chart.

$$\hat{H}_t^s = \sum_{j=1}^{j=N} H_{t,j}^s / N \tag{5.1}$$

where $H_{t,j}^s$is the cumulative hit number of j th specimen that is calculated through summing all hits for the t th micro-damage type (micro-damage types are transverse crack, $t = tr$, delamination, $t = d$, and fiber rupture, $t = fr$) and $N = 3$ is the total number of specimens considered. Here, the superscript s corresponds to reinforcement types in that $s = E - glassorS - glass$. The average numbers of different hits in S-glass reinforced LCS are very close to each other with a minor difference with the following order of $\hat{H}_{tc}^E > \hat{H}_d^E > \hat{H}_{fr}^E$ (Figure 5.8). Figure 5.8 also indicates that the total amount of AE hit in the E-glass reinforced LCS is higher than that of S-glass for all damage types thereby revealing that E-glass reinforced LCS is more prone to micro-damage accumulation. This result explains the reason behind larger drop in shear modulus of E-glass reinforced LCS in comparison to that of S-glass reinforced LCS under the in-plane shear loading. The accumulation of all micro-damage such as fiber rupture, delamination, and transverse crack preclude the load transfer in the shear plane hence leading to the reduction in in-plane shear modulus.

Another important parameter analyzed in this study is the damage initiation in LCSs under in-plane shear loading. The damage initiation is characterized by an onset ratio, which is defined as the ratio of stress at which the first micro-damage signal appears to the final stress at which test is stopped (the strain level of $2x10^4$ $\mu\epsilon$). The onset ratios for different micro-damage types are tabulated in Table 5.2.

TABLE 5.2: Onset ratio of micro-damage for E-glass and S-glass reinforced LCS.

Type of LCS	σ_{otr}	σ_{od}	σ_{ofr}
S-glass reinforced	0.055	0.055	0.234
E-glass reinforced	0.055	0.072	0.083

The onset ratio of transverse crack ((σ_{otr})) and fiber rupture ((σ_{ofr})) for the E-glass reinforced LCS is smaller than that for the S-glass reinforced LCS whereas the onset ratio of delamination ((σ_{od})) for the S-glass reinforced LCS is bigger than that for E-glass-reinforced LCS. The lower values of (σ_{otr}) and (σ_{ofr}) for

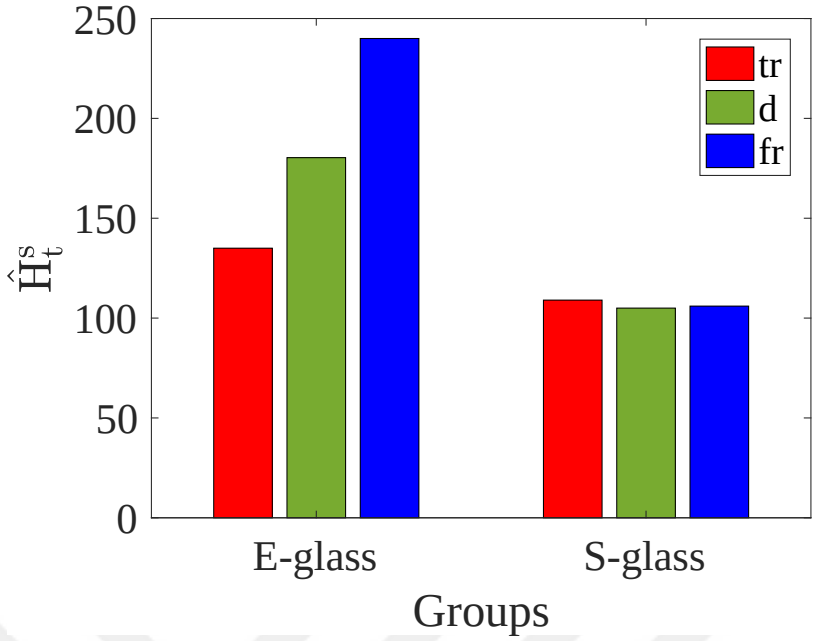

FIGURE 5.8: Average number of different signal types recorded in S-glass and E-glass reinforced LCS analyzed by AE-setup.

E-glass reinforced LCS clearly suggests that the E-glass reinforced LCS is more vulnerable to transverse crack and fiber rupture formation than S-glass under in-plane shear stress loading, but less prone to delamination in comparison to S-glass reinforced LCS. Table 5.2 evidently shows that in the E-glass reinforced LCS, the deformation starts with the formation of transverse cracks which are perpendicular to loading direction. The transverse cracks in a small V-notch region coalesce hence leading to the occurrence of delamination and subsequently fiber rupture due to the fact that the load carrying capacity of the matrix is lessened owing to the transverse crack and delamination, as depicted in Figure 5.9(a). On the other hand, as for the S-glass reinforced LCS, the deformation in V-notch region begins with the creation of transverse crack and delamination simultaneously under the same stress level, which is followed by fiber ruptures, as schematically described in Figure 5.9(b). The relatively higher micro-damage onset ratios (transverse crack and fiber rupture) for the S-glass compared to the E-glass reinforced LCS make it a suitable reinforcement material for a structural component subjected to in-plane shear loading during its service life.

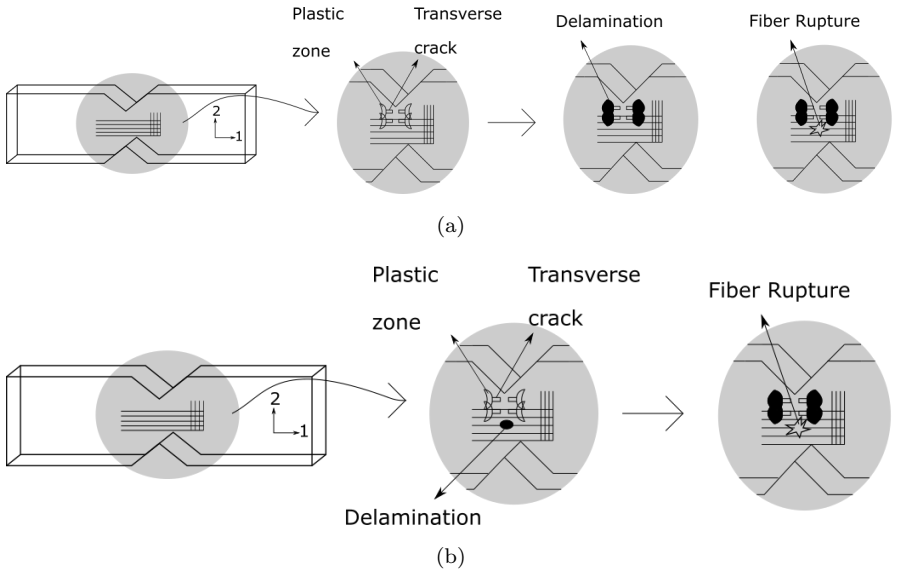

FIGURE 5.9: A schematic illustration of distinct types of micro-crack initiation for a) E-glass and b) S-glass reinforced LCS.

5.3.3 Surface Temperature Monitoring

Figure 5.10 shows temperature map of a specimen attached to the Iosipescu fixture during the shear test. Before loading the specimen, there is a significant temperature gradient on the surface of the specimen as seen in Figure 5.10 (a). This temperature gradient is due to the fact that the lower part of the specimen directly touches the metal surface of the Iosipescu test fixture which is in contact with the rest of the UTM machine that acts like heat sink, thereby causing low temperature profile at the bottom portion of the specimen. Upon loading the specimen, micro-damage predominantly occurs in the V-notch region due to the stress concentration, leading to a temperature rise. The temperature rise can be related to several combined reasons such as heating generation due to the plastic deformation at the end of the crack tips that are formed and the friction between the internal surfaces of the cracks [54]. Referring to temperature variation in Figure 5.10 one can observe that the micro-damage starts in the upper V-notch as a thin spike and extends across the lower V-notch in a direction parallel to the applied load. As more micro-damage accumulates, the temperature of the mid-section of the specimen raises. To be able to monitor the evaluation of average temperature in the vicinity of V-notch region for each specimen, a rectangular domain with the dimensions of $4x10$ mm is considered on the recorded images as shown in Figure 5.10. The calculated average temperatures for all specimens are plotted as a function of shear stress in Figure 5.11. The S-glass reinforced

LCS shows negligible temperature change up to 45 MPa (Figure 5.10 and Fig-ure 5.11), after which a significant rise is observed until fracture. On the other hand, temperature monotonically increases for the E-glass reinforced LCS and, at the end of the test, E-glass reinforced LCS has higher values of temperature than the S-glass reinforced LCS, attributable to larger micro-damage accumulation in E-glass reinforced LCS. This observation is in mesh with the results of AE for E-glass reinforced LCS.

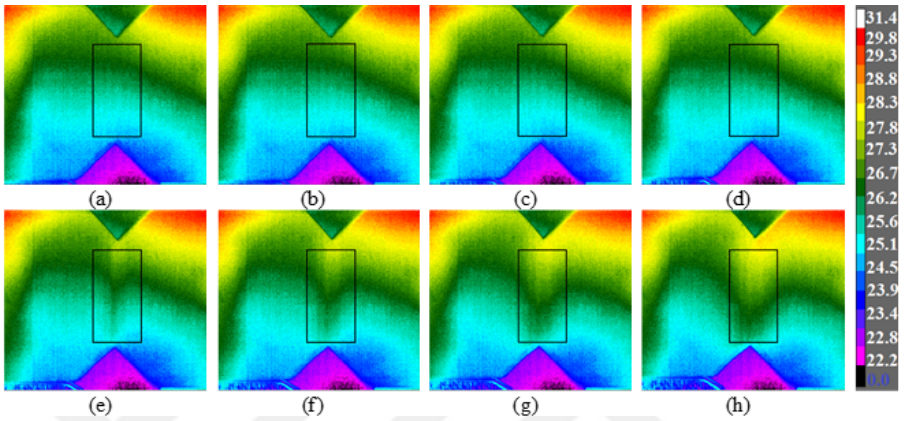

FIGURE 5.10: Temperature (given in °C) map of a S-glass reinforced Iosipescu specimen in the V-notch region during the shear test. Images are taken at the following stress levels; a) 0 MPA, b) 15 MPa, c)30 MPa, d) 43 MPa, e) 47 MPa, f) 50 MPa, g)52 MPa, h) 55 MPa .

The inset figures (a), (b) and (c) in Figure 5.11 indicate the cumulative number of hits corresponding to shear stress ranges of 0-20 MPa, 20-40 MPa and after 40 MPa where the letters E and S, respectively, shows the results for E-and S-glass reinforced laminates for three different damage types, transverse crack, delamination, and fiber rupture. It is seen that at the initial state of the loading between 0-20 MPa, the occurrence of transverse crack and delamination for S-glass LCS is higher than that for E-glass. There might be two possible physical reasons that can be referred to for explaining why transverse cracks and delamination in S-glass reinforced LCS is higher than that in E-glass reinforced LCS. The first one is related to the strength of the S-glass while the second one is associated with the residual stress. Knowing that S-glass is of a notably higher tensile and modules values than E-glass [55], it is logical to expect that the S-glass reinforced LCS is much more stiffer or has a brittle nature, which is expected to be much prone to transverse crack formation and delamination promoted by the coalescence of transverse cracks. Therefore, at initial loading state up to 20 MPa, the cumulative number of hits for both transverse cracks and delamination in S-glass fiber reinforced LCS is larger than that in E-glass fiber reinforced LCS. In relation to the

second reasoning, the coefficient of thermal expansion (CTE) of E-glass is nearly 3.5 times larger than that of S-glass [55]. In the curing process of composites, naturally, E-glass will expand more in comparison to S-glass, and upon curing of the epoxy resin which locks the expanded length of the fibers, E-glass reinforced LCS will experience a larger residual tensile stress than that of S-glass reinforced LCS. The residual tensile stress will act as a crack inhibitor force since it is in the length direction of transverse cracks. As result, the crack coalescence in E-glass reinforced LCS is expected to be more difficult than that in S-glass reinforced LCS. Therefore, transverse cracks formed in S-glass reinforced LCS can relatively easily coalesce thereby promoting the occurrence of delamination, which explains why at initial loading the cumulative number of hit pertaining to delamination for S-glass reinforced LCS is higher than that of E-glass reinforced LCS.

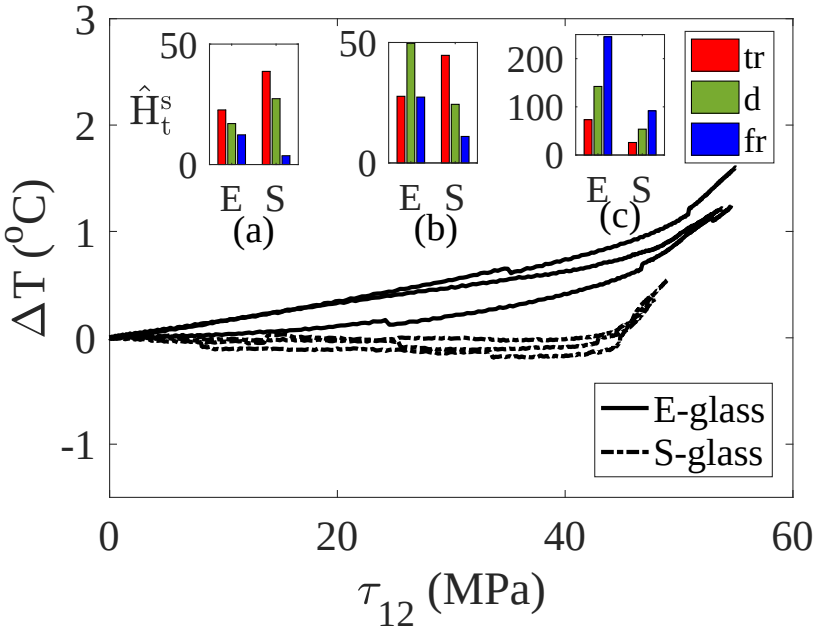

FIGURE 5.11: The average temperature change of LCSs from the region of interest with respect to the in-plane shear stress.

In comparing results for E-glass reinforced LCS in inset figures a, b and c, one can see that as the applied shear stress increases referring to the inset figure b, naturally, existing damages coalesce thereby promoting delamination and facilitate the formation of new transverse cracks and delaminations. Since the load carrying capacity of matrix is lessened due to matrix damages with the increase of the applied shear stress, E-glass fibers in the LCS will be carrying the larger portion of the applied load with its lower fiber strength and modulus compared to S-glass, hence experiencing more rupture than S-glass.

Upon comparing inset figures, a and b, for S-glass fiber reinforced LCS, it is seen that the transverse cracks and delamination are not intensified with the increase in applied shear stress in comparison to E-glass reinforced LCS. This is due to the fact that S-glass fiber does not rupture easily and in turn carries larger portion of the applied load. With the increase in applied shear stress, the load carrying capacity of matrix material is lessened due to matrix damage formation, and naturally S-glass fibers carry larger portion of the applied load, hence leading to an increase in the fiber rupture. After 40 MPa, since the matrix is weakened totally, the applied load is embraced mainly by the fibers. Therefore, there is obvious increase in the cumulative number of hits relevant to fiber rupture.

The thermal conductivity of S-glass is higher than that of E-glass, being respectively, 1.45 W/mK, and 1.3 W/mK at room temperature [55]. Therefore, the heat generated by transverse cracks and delamination in S-glass reinforced CLS can be transferred to ambient environment as well as Iosipescu test fixture faster than E-glass reinforced LCS. Therefore, the temperature rise in S-glass reinforced LCS is smaller than that in E-glass reinforced LCS. It is seen from the inset figure c that after nearly 40 MPa, the fiber fracture becomes dominantly higher than both transverse cracks and delamination for both E-and S-glass reinforced LCSs. The sudden rise in temperature clearly indicates that fiber rupture generates more heat than what transverse cracks and delamination leads to.

5.4 Conclusion

The aim of this study is to compare to damage initiation and accumulation behavior of E-glass and S-glass reinforced LCS under the shear loading. For this purpose, the surface temperature and AE hits of the S-glass and E-glass reinforced LCS specimens are recorded under in-plane shear loading. The in-plane shear stress is applied to V-notch specimens with the Iosipescu test fixture. AE signals are clustered with K-means algorithm and three well-separated clusters are obtained. Each of clusters contain AE signal belong to different micro-damage types namely, transverse crack, delamination, and fiber rupture. Following conclusions are drawn in this study:

1. AE signals can be successfully clustered with K-means algorithm by using Bray-Curtis dissimilarity function.

2. The tensile residual stress in E-glass reinforced LCS delay the coalescence of transverse crack and in turn delamination. Hence, the onset ratio of delamination in S-glass reinforced LCS is smaller than in E-glass reinforced LCS.

3. In total, a larger amount of micro-damage occurs in the E-glass reinforced LCS than S-glass reinforced LCS.

4. It is shown that there is an obvious connection between the total number of AE hits, rise in temperature and decrease in in-plane shear modulus. The larger the drop in in-plane shear modulus, the higher the number of AE hit and temperature rise of the tested specimen.

Acknowledgments

The authors gratefully acknowledge the funding provided by Ministry of Science, Industry and Technology of Turkey for the projects with the contract number of 01307.STZ.2012-1. The first author also gratefully acknowledges the funding provided by The Scientific and Technological Research Council of Turkey (TUBITAK) under the 2214-A International Research Fellowship Program for PhD Students.

Chapter 6

Determination of Stiffness Matrix with Lamb Wave Velocity Measurement

Abstract:

In this study, we present a numerical study of a novel test method in order to calculate the full stiffness matrix and elastic constants of a transversely isotropic thin-laminated composite structure (LCS). The novel test method is based on the group velocity measurement of the $A0$ and $S0$ mode of Lamb waves which propagate in the LCS. The group velocities of $S0$ and $A0$ mode of Lamb wave are measured in different directions, in turn they are used in Christoffel's Equation to calculate the components of stiffness matrix. Thereafter, the components of stiffness matrix are used to calculate elastic constants of LCSs. Result indicate that five independent components of stiffness matrix and laminate elastic constants can be successfully calculated with the method proposed in this study.

Keywords: Lamb wave; velocity; $A0$ and $S0$ modes; laminated composites

6.1 Introduction

To develop a new vehicle such as plane, car, or ship, engineers have to follow a number of certain steps. These steps include 3-D modeling of a vehicle, choice of

candidate materials for the vehicle, and stress analysis with finite element (or finite difference) model. While 3-D model enables us to see final geometry, stress analysis (SA) helps us to understand that whether the 3-D model of vehicle can bear the operational loads or not. For the SA, the candidate materials properties, such as components of stiffness matrix, should be determined experimentally, then needs to be assigned to the 3-D model. If the vehicle is built out of laminated composites, the determination of components of stiffness matrix becomes troublesome due to their anisotropic nature.

The components of stiffness matrix can be calculated if elastic constants such as Young's modulus, Poisson's ratio or shear modulus in certain directions are known. The measurement of these elastic constants can be carried out in laboratories and requires expensive Universal Testing Machine (UTM), sophisticated test fixtures, long coupon processing times and significant personal effort. To overcome these issues, the usage of the ultrasonic bulk wave has been considered to determine the components of stiffness matrix [56]. Several experimental works have shown that the components of stiffness matrix can be measured by immersion ultrasonic testing. In this test, LCS specimens are immersed in a water-filled tank between a piezoelectric transmitter and receiver couple. An ultrasonic wave is excited by a transmitter and the wave propagates through water, specimen, again water and finally hits the receiver. Then, the velocities of the ultrasonic wave in different planes of interest are measured to calculate the components of stiffness matrix. Stijnman [57] used immersion ultrasonic testing to measure the components of stiffness matrix of E-glass and Kevlar reinforced LCSs. Karabutov et al. [58] proposed an immersion ultrasonic test to determine the stiffness matrix of uni-directional graphite reinforced LCS with a laser source and piezo-electric sensor employed as transmitter and receiver, respectively. Marguères et al. [59] used transmitted ultrasonic bulk waves to calculate the elastic constants of LCS immersed in a water-filled tank. Apart from LCSs, Goldman et al. [60] determined the stiffness matrix of the bovina cortival bone of human skeleton with immersion ultrasonic method. On the other hand, Kriz et al. [56] demonstrated that the complete set of the elastic constant of transversely isotropic LCS at any fiber volume fraction can be calculated by measuring the ultrasound velocities in different directions without the water-filled tank. Datta et al. [61] calculated the elastic constants of graphite fiber reinforcement used in a metal matrix with an inverse methodology. For that purpose, Datta et al. [61] calculated the complete sets of elastic constants of metal matrix and graphite fiber reinforced metal matrix with

ultrasound velocity measurement. Then, by an inverse-modeling, fiber's elastic constants are extracted.

In addition to the determination of the stiffness matrix of LCSs with immersion ultrasonic test, several studies reports the usage of pulse-echo technique to determine components of stiffness matrix without a water-filled tank. For, pulse-echo technique, tested materials are assumed isotropic and only one sensor is used to trigger and capture the ultrasonic wave. The ultrasonic wave propagates through the material and reflects backs to the sensor from the rear edge of the material. Wang et al. [62] used longitudinal and transversal ultrasonic bulk wave velocities to measure elastic constants (i.e., Young's modulus, bulk modulus, and Poisson's ratio) of single crystal diamond, $LiNbO_3$, $LiTaO_3$, silicon, and various polycrystalline hard materials. Dodd et al. [63] used the pulse-echo technique to measure the velocity of the ultrasonic wave. They used this technique to determine the elastic constants of transition-metal carbide ceramics as a function of temperature and hydrostatic pressure. Phani et al. [64] establish a correlation between Poisson's ratio and ultrasonic longitudinal wave velocity for porous materials such as Uranium dioxide, which is extremely fragile thus hard to test mechanically (with a destructive test).

Although in literature a number of experimental studies can be found for the determination of the stiffness matrix of thick-LCSs and for different materials by performing ultrasonic wave velocity measurement, no emphases are put on the determination of the stiffness matrix of thin-LCSs, in particular with the A0 and S0 modes of Lamb wave. Lamb waves are ultrasonic waves that propagate on the plate-like structures (ie., thin-LCS). Lamb waves propagate with a number of symmetric and antisymmetric modes according to its frequency range. These modes have great significance in calculating stiffness matrix. Lamb waves propagation in plate-like structures is complex and a number of different modes can propagate together, which might cause errors in performing velocity measurement. The errors in velocity measurements influence the accurate calculation of stiffness matrix. Therefore, to understand the nature of Lamb wave propagation in LCSs, we perform a numerical simulation study with finite element method (FEM). Numerical simulation provides valuable information on the nature of the problem and it also enables us to omit experimental variables such as temperature, humidity, heterogeneity of LCS. Omitting these experimental variables makes the problem simple and enables us to concentrate only on the interaction of Lamb

wave with LCS. In addition to these, to the best of the authors' knowledge, the numerical simulation of Lamb wave with FEM to determine the stiffness matrix of thin-LCSs is not reported previously. On the other hand, a number of different studies can be found to address varying purposes such as Structural Health Monitoring (SHM) and Non-destructive Evolution and Testing (NDE/NDT) [65] of LCSs with FEM. Ramadas et al.[66] studied the ultrasound wave attenuation due to material properties with FEM. Samaratunga et al. [67] investigated the detection of delamination with Lamb wave propagation by both using Finite Element Analysis (FEA) and experimental work. They correlated their FEA results with experiment. Jha et al.[68] studied excitation signal parameters to detect the delamination in LCSs with FEM. Three different frequencies (15, 18 and 20 kHz) and two different pulse widths (3.5 and 5.5 cycles) were studied. They found out that 5.5 cycles with 18 kHz frequency reveals delamination more clearly than the other frequencies and pulse widths used. Singh et al. [69] carried out FEA and experimental investigations on the propagation of Lamb waves and their interaction with the front edge of delaminations in a cross-ply and unidirectional LCSs. Wan et al. [70] studied the interaction of Lamb waves with micro-cracks of various lengths and widths buried in a thin metallic plate through FEA. Luca et al. [71] investigated the effect of various damage variables such as the shape, size, and extent of damage on reflected signals from the damage by FEA. Hosseini et al. [72] presented an FEA on the Lamb waves propagation behavior on the metallic foam sandwich plate with a parametric study. The loading frequencies and geometrical properties of the plate such as relative density, structural irregularity, and the cover plate thickness were the subjects of this study. Agostini et al. [73] analyzed the interaction of Lamb waves with notches, delamination, and complex structures with FEA. They observed a time-shift delay in the received signal for a plate with delamination comparing to sound (undamaged) plate. Ramadas et al. [74] numerically (with FEA) investigated the Lamb waves attenuation by using Rayleigh damping model. They showed that even for small distances (50 mm), Lamb waves undergo an attenuation as big as 40% and confirmed the result of FEA with experiments.

In this study, we attempt to numerically simulate Lamb wave propagation in transversely isotropic thin-LCSs by using a commercial FEM code, Abaqus. Two modes of Lamb waves, zero-order symmetric (S0) and zero-order antisymmetric (A0) modes, are excited and their propagation is numerically investigated in a thin-LCS. This research aims at calculating stiffness matrix and elastic constants

of transversely isotropic thin-LCS by a quick, non-destructive, and inexpensive test method. This objective is achieved by exciting Lamb waves with a broad band source and measuring the group velocity of Lamb waves with numerical simulation (using FEA) in different directions. Then, these group velocities are used in the calculation of the components of stiffness matrix. Thereafter, the components of stiffness matrix are used to calculate laminate elastic constants.

6.2 Stiffness Matrix and Elastic Constants

The relationship between the stress and strain is defined with generalized Hooke's law for linear-elastic material as follows:

$$\sigma_{ij} = c_{ijkl}\epsilon_{kl} \tag{6.1}$$

where σ_{ij} is the stress tensor, ϵ_{kl} is the strain tensor, and c_{ijkl} is the general $9x9$ stiffness tensor of anisotropic materials. The open form of Equation 6.1 is as follows:

$$\begin{Bmatrix} \sigma_{11} \\ \sigma_{22} \\ \sigma_{33} \\ \sigma_{23} \\ \sigma_{13} \\ \sigma_{12} \\ \sigma_{32} \\ \sigma_{31} \\ \sigma_{21} \end{Bmatrix} = \begin{bmatrix} c_{1111} & c_{1122} & c_{1133} & c_{1123} & c_{1113} & c_{1112} & c_{1132} & c_{1131} & c_{1121} \\ c_{2211} & c_{2222} & c_{2233} & c_{2223} & c_{2213} & c_{2212} & c_{2232} & c_{2231} & c_{2221} \\ c_{3311} & c_{3322} & c_{3333} & c_{3323} & c_{3313} & c_{3312} & c_{3332} & c_{3331} & c_{3321} \\ c_{2311} & c_{2322} & c_{2333} & c_{2323} & c_{2313} & c_{2312} & c_{2332} & c_{2331} & c_{2321} \\ c_{1311} & c_{1322} & c_{1333} & c_{1323} & c_{1313} & c_{1312} & c_{1332} & c_{1331} & c_{1321} \\ c_{1211} & c_{1222} & c_{1233} & c_{1223} & c_{1213} & c_{1212} & c_{1232} & c_{1231} & c_{1221} \\ c_{3211} & c_{3222} & c_{3233} & c_{3223} & c_{3213} & c_{3212} & c_{3232} & c_{3231} & c_{3221} \\ c_{3111} & c_{3122} & c_{3133} & c_{3123} & c_{3113} & c_{3112} & c_{3132} & c_{3131} & c_{3121} \\ c_{2111} & c_{2122} & c_{2133} & c_{2123} & c_{2113} & c_{2112} & c_{2132} & c_{2131} & c_{2121} \end{bmatrix} \begin{Bmatrix} \epsilon_{11} \\ \epsilon_{22} \\ \epsilon_{33} \\ \epsilon_{23} \\ \epsilon_{13} \\ \epsilon_{12} \\ \epsilon_{32} \\ \epsilon_{31} \\ \epsilon_{21} \end{Bmatrix} \tag{6.2}$$

The stress, stiffness, and strain tensors of a general anisotropic material are symmetric and can be expressed by the following expressions [75]:

$$\sigma_{ij} = \sigma_{ji}, c_{ijkl} = c_{jikl} = c_{ijlk} = c_{klij}, \epsilon_{ij} = \epsilon_{ji} \tag{6.3}$$

By considering the symmetries in above stress, stiffness, and strain tensors, the Equation 6.2 can be rearranged accordingly:

$$\begin{Bmatrix} \sigma_{11} \\ \sigma_{22} \\ \sigma_{33} \\ \sigma_{23} \\ \sigma_{13} \\ \sigma_{12} \end{Bmatrix} = \begin{bmatrix} c_{1111} & c_{1122} & c_{1133} & c_{1123} & c_{1113} & c_{1112} \\ & c_{2222} & c_{2233} & c_{2223} & c_{2213} & c_{2212} \\ & & c_{3333} & c_{3323} & c_{3313} & c_{3312} \\ & & & c_{2323} & c_{2313} & c_{2312} \\ & & & & c_{1313} & c_{1312} \\ symm & & & & & c_{1212} \end{bmatrix} \begin{Bmatrix} \epsilon_{11} \\ \epsilon_{22} \\ \epsilon_{33} \\ \epsilon_{23} \\ \epsilon_{13} \\ \epsilon_{12} \end{Bmatrix} \tag{6.4}$$

Therefore, the number of independent components of stiffness tensor reduces to twenty one from eighty one. To make the Equation 6.4 more convenient for readers, it can be rearranged with Voigt notion with two indices instead of four. We will define stiffness tensor with Voigt notion as C_{mn} instead of c_{ijkl}; here m corresponds to ij pair and n corresponds to kl pair. The conversion from stiffness tensor to Voigt form is performed according to the relation given in Table 6.1.

TABLE 6.1: Conversion of stiffness tensor to Voigt form

Tensor indices	Voigt indices
i=j=1, k=l=1	m=n=1
i=j=2, k=l=2	m=n=2
i=j=3, k=l=3	m=n=3
i=k=2, j=l=3 or i=k=3, j=l=2	m=n=4
i=k=1, j=l=3 or i=k=3, j=l=1	m=n=5
i=k=1, j=l=2 or i=k=2, j=l=1	m=n=6

Now the fourth-order stiffness tensor (c_{ijkl}) becomes second-order stiffness tensor (C_{mn}). To prevent the confusion with the word "tensor", second-order stiffness tensor (C_{mn}) will be called the elastic stiffness matrix or elasticity matrix in the rest of this thesis due to fact that a second-order tensor can be represented by a matrix. Therefore, the elasticity matrix for a general anisotropic medium is given as follows:

$$C_{mn} = \begin{bmatrix} C_{11} & C_{12} & C_{13} & C_{14} & C_{15} & C_{16} \\ & C_{22} & C_{23} & C_{24} & C_{25} & C_{26} \\ & & C_{33} & C_{34} & C_{35} & C_{36} \\ & & & C_{44} & C_{45} & C_{46} \\ & & & & C_{55} & C_{56} \\ symm & & & & & C_{66} \end{bmatrix} \tag{6.5}$$

As indicated in Equation 6.5, the elasticity matrix is symmetric, $C_{mn} = C_{nm}$. A number of hierarchies in the level of anisotropy can be found among the variety of material systems. This thesis focuses on the LCSs, which generally speaking are transversely isotropic mediums due to the unidirectional fiber reinforcement used. Therefore, we will derive the elasticity matrix for transversely isotropic mediums. Before reducing the elasticity matrix for transversely isotropic medium, it is necessary to consider orthotropic symmetry. In orthotropic mediums, three mutually perpendicular twofold axes of symmetry exist. On each of the three mutually perpendicular axes, mechanical properties are independent of direction (ie., $x_1 = -x_1$, $x_2 = -x_2$, and $x_3 = -x_3$) [76]. Therefore, the total number of independent components of elasticity matrix reduces to 9 from 21 and the elasticity matrix (C_{mn}) reads:

$$C_{mn} = \begin{bmatrix} C_{11} & C_{12} & C_{13} & 0 & 0 & 0 \\ & C_{22} & C_{23} & 0 & 0 & 0 \\ & & C_{33} & 0 & 0 & 0 \\ & & & C_{44} & 0 & 0 \\ & & & & C_{55} & 0 \\ symm & & & & & C_{66} \end{bmatrix} \tag{6.6}$$

Now it is easy to derive the elasticity matrix of transversely isotropic medium by using orthotropic symmetry. In transversely isotropic medium, the total number of independent constants reduces to five from nine. For transversely isotropic medium, in addition to the three mutually perpendicular twofold axes of symmetry, material properties on two out of three axes are same, whilst the other axis has different material properties. The elasticity matrix for transversely isotropic mediums read:

$$C_{mn} = \begin{bmatrix} C_{11} & C_{12} & C_{12} & 0 & 0 & 0 \\ & C_{22} & C_{23} & 0 & 0 & 0 \\ & & C_{22} & 0 & 0 & 0 \\ & & & C_{44} & 0 & 0 \\ & & & & C_{66} & 0 \\ symm & & & & & C_{66} \end{bmatrix} \tag{6.7}$$

and

$$C_{44} = (C_{22} - C_{23})/2 \tag{6.8}$$

Each of the components of elasticity matrix can be expressed by material elastic constants with following relations:

$$C_{11} = E_1(1 - \nu_{23}\nu_{32})\Psi \tag{6.9}$$
$$C_{12} = E_1(\nu_{21} + \nu_{31}\nu_{23})\Psi = E_2(\nu_{12} + \nu_{32}\nu_{13})\Psi \tag{6.10}$$
$$C_{13} = E_1(\nu_{31} + \nu_{21}\nu_{32})\psi = E_3(\nu_{13} + \nu_{12}\nu_{23})\Psi \tag{6.11}$$
$$C_{22} = E_2(1 - \nu_{13}\nu_{31})\Psi \tag{6.12}$$
$$C_{23} = E_2(\nu_{32} + \nu_{12}\nu_{31})\Psi = E_3(\nu_{23} + \nu_{21}\nu_{13})\Psi \tag{6.13}$$
$$C_{33} = E_3(1 - \nu_{12}\nu_{21})\Psi \tag{6.14}$$
$$C_{44} = G_{23} \tag{6.15}$$
$$C_{55} = G_{13} \tag{6.16}$$
$$C_{66} = G_{12} \tag{6.17}$$

and

$$\Psi = \frac{1}{1 - \nu_{12}\nu_{21} - \nu_{23}\nu_{32} - \nu_{31}\nu_{13} - 2\nu_{21}\nu_{32}\nu_{13}} \tag{6.18}$$

where E_i is the Young's modulus in the direction of i, ν_{ij} is the Poisson's ratio which corresponds to the contraction along the j-axis when an expansion is applied in i-axis. Also, G_{ij} is the shear modulus in j-axis on the plane whose normal is in the direction of i. For a transversely isotropic medium, the following relations also exist among the young moduli, Poisson's ratios and shear moduli.

$$E_2 = E_3, \nu_{12} = \nu_{13}, G_{12} = G_{13} \tag{6.19}$$

Up to now, the components of the stiffness matrix for specially orthotropic, namely transversely isotropic materials, are derived. Furthermore, it is shown that by using material elastic constants such as E_i, G_{ij} and ν_{ij}, the components of elastic stiffness matrix can be calculated. On the other hand, we can also approximate the elastic constants of given transversely isotropic material with inverse formulations derived by Hashin et al. [77]. The formulation for the elastic constants, derived

by Hashin et al. [77], are given as follows:

$$K_{23} = \frac{1}{2}(C_{22} + C_{23}) \tag{6.20}$$

$$G_{23} = \frac{1}{2}(C_{22} - C_{23}) \tag{6.21}$$

$$G_{12} = G_{13} = C_{55} = C_{66} \tag{6.22}$$

$$E_1 = C_{11} - \frac{2C_{12}^2}{C_{22} + C_{23}} \tag{6.23}$$

$$\nu_{21} = \nu_{31} = \frac{1}{2}\left(\frac{C_{11} - E_1}{K_{23}}\right)^{1/2} \tag{6.24}$$

$$E_2 = E_3 = \frac{4G_{23}K_{23}}{K_{23} + \psi G_{23}} \tag{6.25}$$

$$\nu_{23} = \frac{K_{23} - \psi G_{23}}{K_{23} + \psi G_{23}} \tag{6.26}$$

$$\tag{6.27}$$

and

$$\psi = 1 + \frac{4K_{23}\nu_{21}^2}{E_1} \tag{6.28}$$

6.3 Relation Between Lamb Waves and Stiffness Matrix

In thin plates, ultrasonic waves are guided by the bottom and top boundaries (faces) of plates through the thickness and are called Lamb waves. Lamb waves propagate as symmetric (S) and anti symmetric (A) modes (symmetric, $d : s$ and antisymmetric, $d : as$) as per the mid plane of the plate as shown in Figure 6.1.

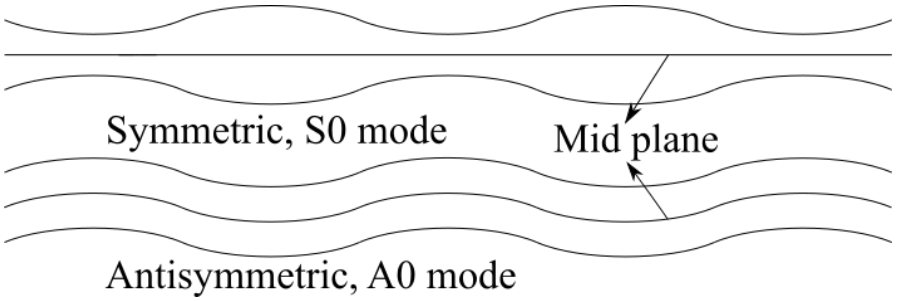

FIGURE 6.1: Modes of Lamb waves, symmetric and antisymmetric waves.

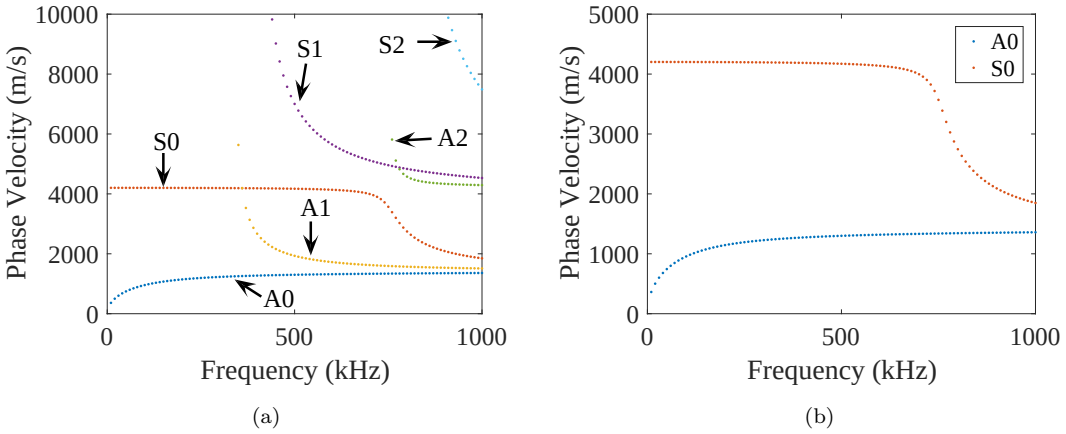

FIGURE 6.2: Lamb wave dispersion curves(a) first four modes, (b)zero order symmetric and anti symmetric modes. Dispersion curves of Lamb wave modes are calculated by GUIGUW software [2]

Lamb waves might have a number of orders (ie., zero order (S0, A0), first order (S1, A1), second order (S2, A2) etc...) for symmetric and antisymmetric modes regarding given frequency interval as shown in Figure 6.2(a). However, we only consider zero-order symmetric (S0) and antisymmetric (A0)Lamb wave modes for the calculation of stiffness matrix in this study. There are several significant reasons for this interest. First of all, zero-order Lamb wave modes as clearly seen in Figure 6.2(b) show no sign of dispersion up to 700 kHz. This eliminates the frequency dependence of phase velocity and leaves only the density and stiffness of the medium as variables. Second, we are interested in low band frequency region (0-400 kHz) where only two modes, S0 and A0, are active. Therefore we can eliminate the contribution of other modes and makes the analysis simple. Third, in this study, we use the group velocity (C_g) of Lamb wave, which relates the phase velocity (C_p) with Equation 6.29. Since the phase velocity is not dispersive in the range of 0-400 kHz, C_g is also not dispersive and $C_p = C_g$ according to Equation 6.29.

$$C_g = \frac{C_p^2}{C_p - (fd)\frac{dC_p}{d(fd)}} \tag{6.29}$$

The relationship between ultrasonic group velocity and the stiffness matrix (C_{mn}) for a general anisotropic material is given by the Christoffel equation as follows [2]:

$$C_{mn} = \rho {V_d}^2 \tag{6.30}$$

where V_d is the ultrasonic group velocity measured in the direction of corresponding component of stiffness matrix, ρ is the material density, and subscript d denotes the modes of ultrasonic wave. Since we are interested in thin-LCSs, also referred to as plate-like structures, we will use Lamb waves to predict the stiffness matrix of LCS. First of all, to create a relationship between Lamb wave velocities and LCS, an orthogonal coordinate system is adapted as shown in Figure 6.3. Here x_1 axis is

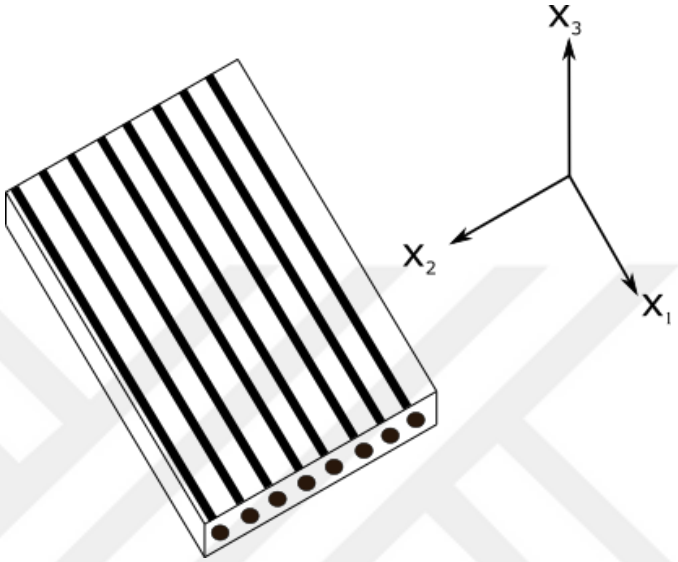

FIGURE 6.3: Assumed Cartesian coordinate system with respect to fiber direction (for the convenience, please keep in mind that following relations also exit among directions: $x = x_1 = 1$, $y = x_2 = 2$, and $z = x_3 = 3$)

.

in the direction of fibers, x_2 axis is through the width and x_3 axis is perpendicular to x_1-x_2 plane. The chosen LCS is composed of laminas containing uni-directional fiber, which have a transversely isotropic symmetry. For the transverse isotropy, there are nine components for stiffness matrix and five of these components are independent as indicated previously. Once the five independent components of stiffness matrix are found, the other four components can also be calculated. The relation between the zero-order symmetric Lamb wave mode and the components of stiffness matrix, C_{11} and C_{22}, are given as follows [78]:

$$C_{11} = \rho V_s^2 \tag{6.31}$$

$$C_{22} = \rho V_s^2 \tag{6.32}$$

where V_s is the group velocity of zero-order symmetric ($S0$) Lamb wave measured in the x_1 and x_2 directions for the Equations 6.31 and 6.32, respectively. However,

the components of stiffness matrix, C_{44} and C_{66}, may be calculated solely by zero-order anti symmetric Lamb wave mode and represented by the following equations:

$$C_{66} = \rho V_{as}^2 \tag{6.33}$$

$$C_{44} = \rho V_{as}^2 \tag{6.34}$$

where V_{as} is the group velocity of zero-order anti symmetric ($A0$) Lamb wave mode measured in the x_1 and x_2 directions for the Equations 6.33 and 6.34, respectively. For the last independent component, C_{12}, the following relation can be considered [79]:

$$\rho V^2 = \frac{1}{2}\left\{C_{22} + C_{11} \pm [(C_{22} - C_{11})^2 + 4(C_{12} + C_{66})^2]^{\frac{1}{2}}\right\} + C_{66} \tag{6.35}$$

where V_s is the group velocity of zero-order symmetric wave propagating in a diagonal direction on the x_1x_2 plane. Once components of stiffness matrix such as C_{11}, C_{22}, C_{44} and C_{66} are known, C_{12} can also be calculated.

6.4 Numerical Simulation of Lamb Wave

A commercial Finite Element Code, Abaqus, is used to numerically model Lamb wave propagation in a transversely isotropic LCS. Abaqus/Implicit solver with 3-D solid composite element is employed for the numerical simulation. Abaqus/Implicit solver requires a number of carefully chosen FEA variables, such as time step, total time, element size, and element type. These variables control the accuracy and cost of computation. Below are given the circumstances under which these variables are chosen.

6.4.1 Numerical Simulation Variables

For the numerical simulation of Lamb wave, Courant-Friedrichs-Lewy (CFL) and Blakes criteria should be satisfied for time step and element size, respectively. According to the CFL criterion, the time step should be chosen small enough to meet the accuracy of solution. Therefore, the following formula is considered:

$$\delta t < \frac{1}{20 * f_{max}} \tag{6.36}$$

where δt is the time step and f_{max} is the max frequency ($\sim 200kHz$) of input load in simulation to excite Lamb wave. For the minimum element size, the Blakes criterion which is given by the following formula is considered:

$$L_{max} < \frac{\lambda_{min}}{n_{min}} = \frac{C}{n_{min} * f_{max}} \tag{6.37}$$

where L_{max} is the maximum element size, C is the dilatational wave speed (4000 m/s) and n_{min} is the number of element per wavelength. For this study, eight elements are considered per wavelength.

According to Equation 6.36, the time step of $3x10^{-7}$ s is chosen. For the element size, Equation 6.37 is considered and two different element sizes in the direction of length and thickness are chosen as 2 and 1 mm, respectively.

A total time of $5x10^{-4}$ s is chosen for all simulations. Although the chosen total time seems small, it ensures enough time to observe Lamb wave propagation in the modelled LCS. As a element type, a general purpose quadratic brick element, C3D20R, is chosen.

All numerical simulations are computed in an eight-core processors desktop computer. For each simulation, parallelization of processors with GPGPU acceleration is utilized. This option reduces the computational time to the one third of the single processor usage.

6.4.2 Damping Constants

Another variable that should be considered in FEA of Lamb wave is attenuation. Attenuation is the reduction of amplitude of wave with the distance of propagation. In wave mechanics, the attenuation of a wave can be due to the viscoeleastic or geometrical properties of the medium. Rayleigh (or proportional) damping model

(Equation 6.38) enable us to consider damping property of medium in the FEA by using material damping constants for Lamb wave attenuation.

$$\xi = \frac{1}{2}\left(\frac{\alpha}{\omega} + \beta\omega\right) \tag{6.38}$$

where ξ is the damping ratio, β and α are stiffness and mass proportional constants, respectively, and ω is the circular frequency which is equal to $2\pi f$ and f is the frequency.

These constants (β and α) need to be calculated experimentally to insert the FEA. The calculation of these constants can be found in [74] in detail. In brief, four AE sensors, aligned in length direction with 50 mm separation distance, are placed on top surface of the laminate (the laminate has same properties with the one used in FEA) and a stress wave is created with Hsu-Nielson source. The stress wave propagates along the plate and hits the sensors. Then, the amplitudes of signal are measured to calculate constants (β and α). The constants, β and α, are found to be $1.1903x10^{-8}$ (s/rad) and 29369 (rad/s) for the LCS under investigation.

6.4.3 LCS and Lamb Wave

As a solid model, a $600x300x1.8$ mm LCS structure is considered. An arbitrarily chosen node on the solid model is used as a load application point. The second, third, fourth and fifth nodes away (15, 65, 115 and 165 mm, respectively) from the load application point are chosen as sensor points(Figure 6.4(a)). The solid model is composed of six individual plies having transversely isotropic symmetry. Each ply has a thickness of 0.3 mm and is reinforced by unidirectional fibers shown in Figure 6.4(b). After the solid model is created, material properties such as density and material elastic constants are assigned to each ply. These material properties are given in Table 6.2. E_1, ν_{12}, G_{12}, and ρ are experimentally measured values, whereas other constants in Table 6.2 are assumed based on literature.

Table 6.2: Material properties assigned to each ply.

E_1 (GPa)	E_2 (GPa)	E_3 (GPa)	ν_{12}	ν_{13}	ν_{23}	G_{12} (GPa)	G_{13} (GPa)	G_{23} (GPa)	ρ (kg/m^3)
29	9	9	0.23	0.23	0.3	3.4	3.4	2.5	1682

To excite two Lamb wave modes, $S0$ and $A0$, two excitation cases are considered. For the A0 mode, plate is only loaded from the top surface whereas for the S0 mode, plate is loaded from the top and bottom surfaces at the same time.

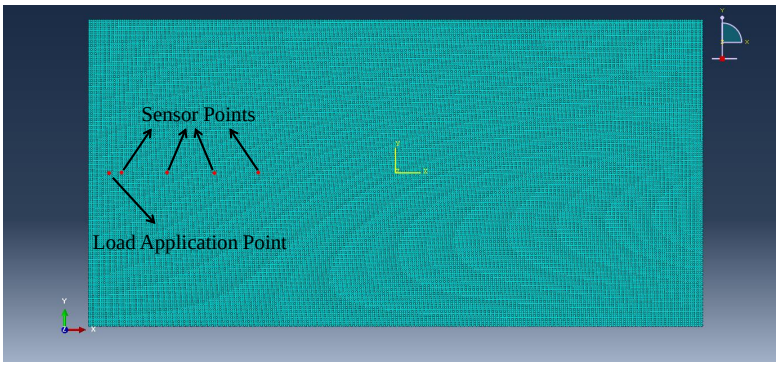

(a)

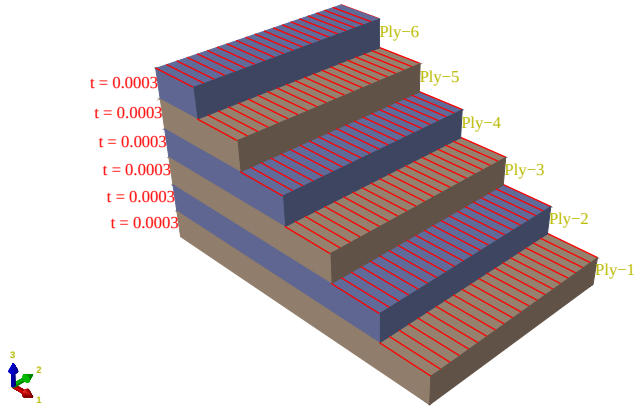

(b)

FIGURE 6.4: (a) Composite plate used in the modelling with load application and sensor points, (b) stack plot of composite plate (red lines indicates direction of fibers, and thickness of plies (t) are given in meter)

As an excitation load, a replica of Hsu-Nielsen source is used. Hsu-Nielsen is a reproducible and broad-band source. A representative wave excitation load in time and frequency domain can be seen in Figure 6.5(a) and (b), respectively. As seen from Figure 6.5(b), frequency range of excitation load is confined between 0 and 400 kHz, which meets the criteria discussed in Section 6.3.

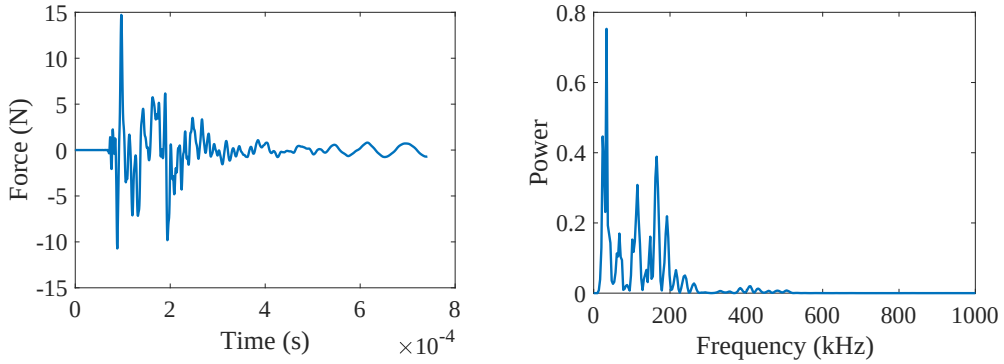

(a) (b)

FIGURE 6.5: A representative load excitation signal (a) in time domain, (b) in frequency domain

6.5 Result and Discussion

6.5.1 Excitation of Lamb Wave Modes

$A0$ and $S0$ modes of Lamb wave are excited on LCS and their propagation in three different directions, through x_1, x_2, and diagonal, are considered for the calculation of stiffness matrix. Once, Lamb waves are excited, enough time is given to Lamb waves to propagate through the plate. A symbolic deformation of LCS by $S0$ and $A0$ modes can be seen in Figure 6.6(a)-(f) and Figure 6.7(a)-(f), respectively. The deformation of LCS by $S0$ Lamb wave mode is symmetric, whereas for the $A0$ mode it is antisymmetric. In Figure 6.6(a)-(f) and Figure 6.7(a)-(f) symbolic deformations take place on the z-direction (the direction that Lamb wave bounded by bottom and top surfaces) while wave propagates in x-direction.

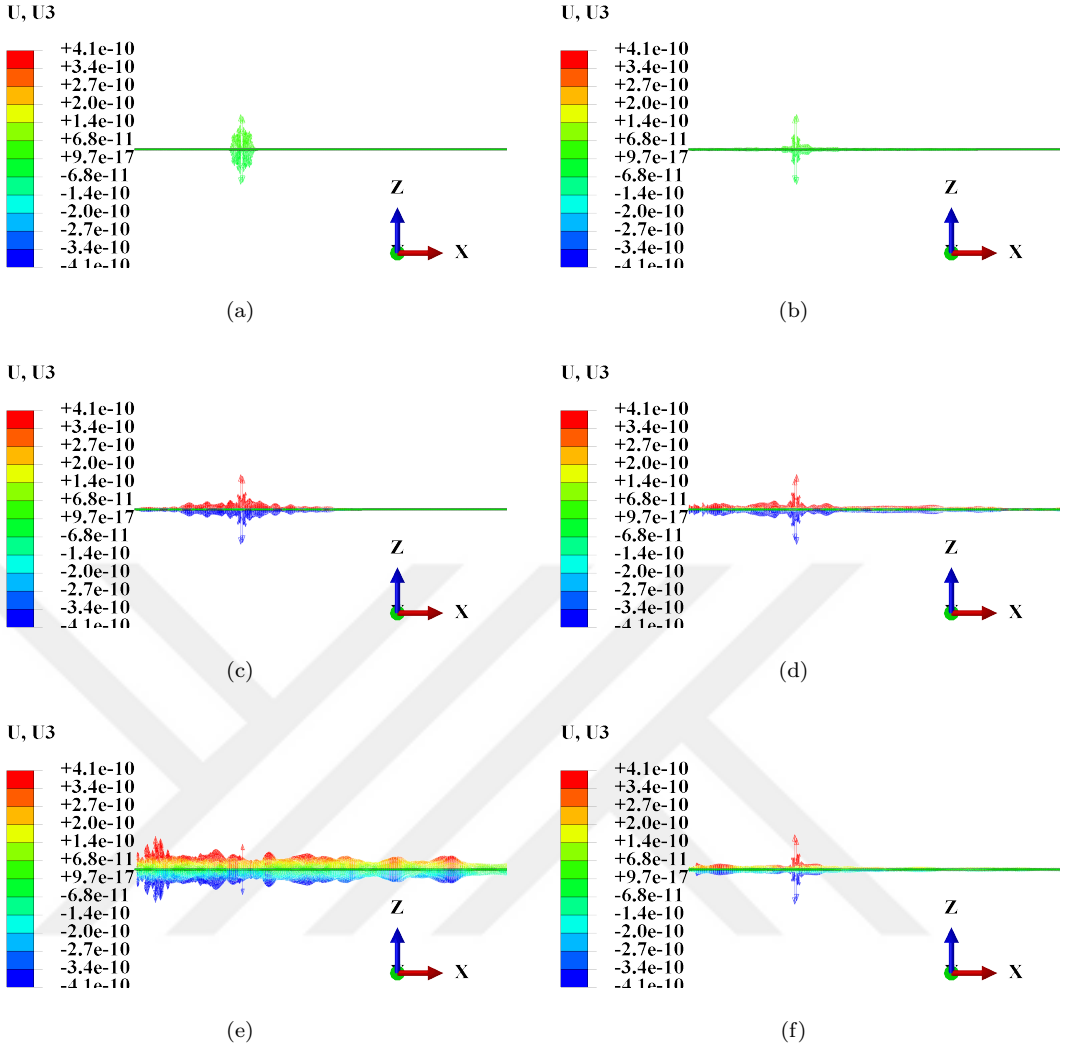

FIGURE 6.6: A symbolic deformation of the plate by S0 Lamb wave mode at different times after excitation by a point force, (a) 3 μs, (b) 42 μs, (c) 84 μs, (d) 126 μs, (e) 168 μs, (f) 210 μs

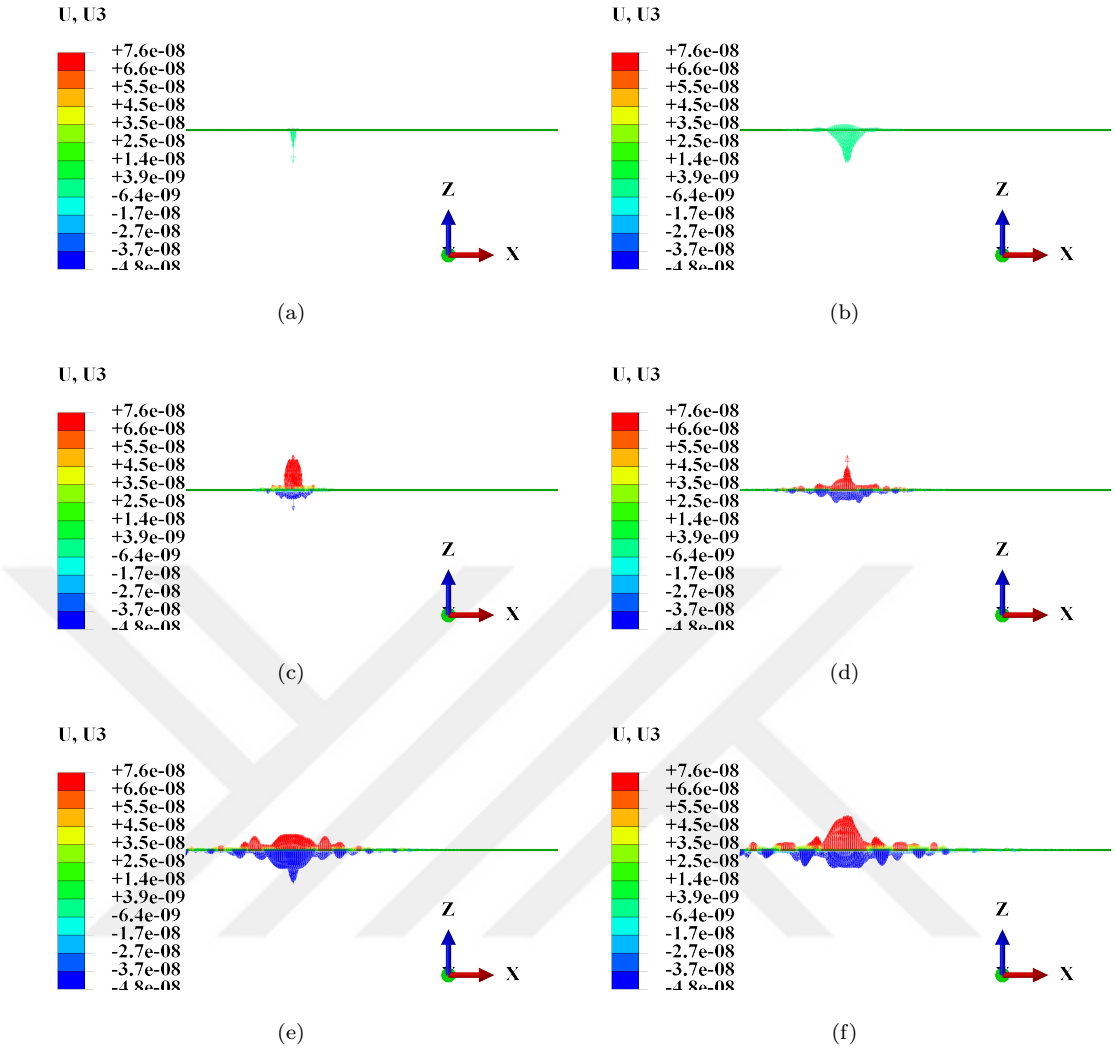

FIGURE 6.7: A symbolic deformation of the plate by A0 Lamb wave mode at different times after excitation by a point force, (a) 3 μs, (b) 42 μs, (c) 84 μs, (d) 126 μs, (e) 168 μs, (f) 210 μs

In Figure 6.8(a)-(f), $S0$ mode of Lamb wave, propagating on x-y plane, can be seen at different times. Furthermore, in Figure 6.9(a)-(f), $A0$ mode of Lamb wave, propagating on x-y plane, can also be seen in different times. Both modes propagate with an elliptical trajectory due to differences in velocities in different directions. The velocity difference stems from the different material properties in different directions. Since LCS is reinforced by high modulus unidirectional fibers along the x-direction, it has higher modulus along x-direction compared to y-direction. Another important point that can be obtained at a glance from Figure 6.8(a)-(f) and Figure 6.9(a)-(f) is the difference between the velocities of $S0$ mode and $A0$ modes. Although the wavefront of $S0$ mode already arrives to the end of the plate, the wavefront of $A0$ mode is still in the middle of the plate at 210 μs.

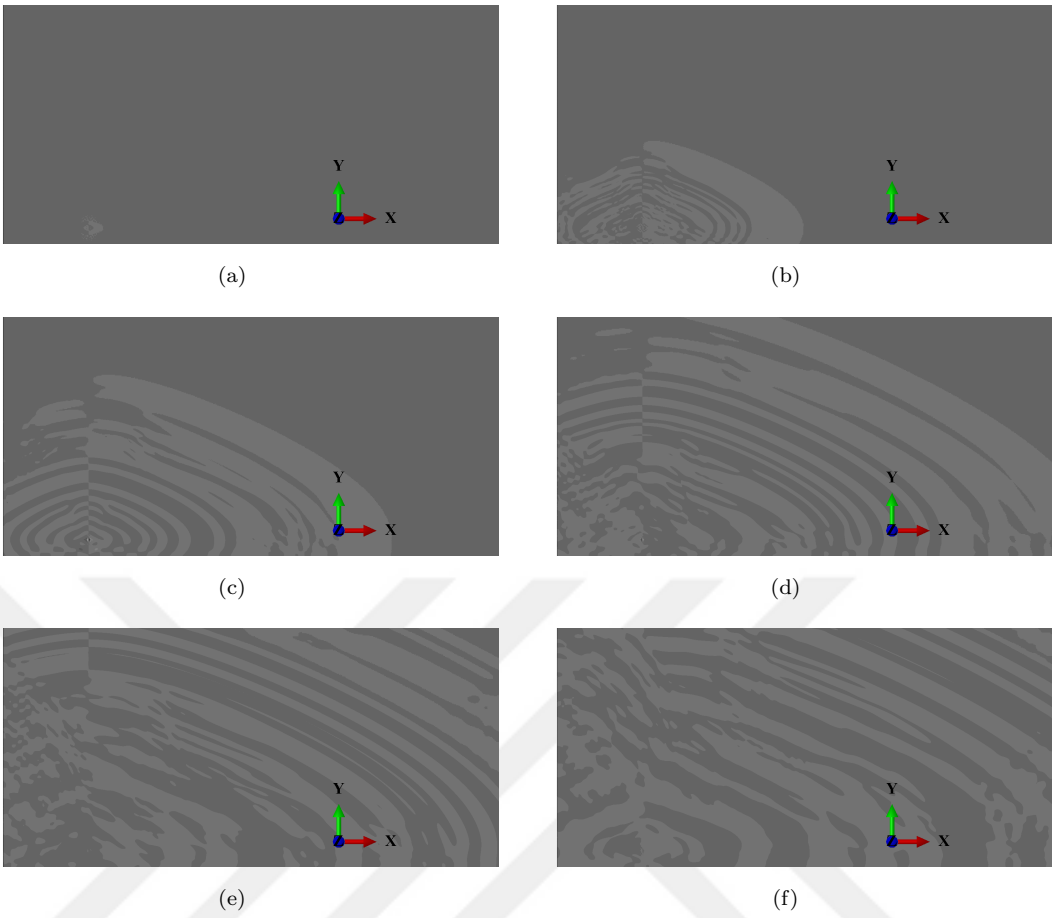

FIGURE 6.8: S0 Lamb wave mode propagating in the LCS captured different times, (a) 3 μs, (b) 42 μs, (c) 84 μs, (d) 126 μs, (e) 168 μs, (f) 210 μs

Representative S0 and A0 Lamb wave modes, captured in four sensor points along x-direction as a time versus displacement in z-direction, can be seen in Figure 6.10(a) and (b), respectively. When Figure 6.10(a) and (b) are investigated, an important difference between the S0 mode and A0 mode can be seen. One can see that S0 mode is compact, which has lots of peaks and valleys in the given time interval. On the other hand, A0 mode is loose and has less numbers of peaks and valleys in the given time interval.

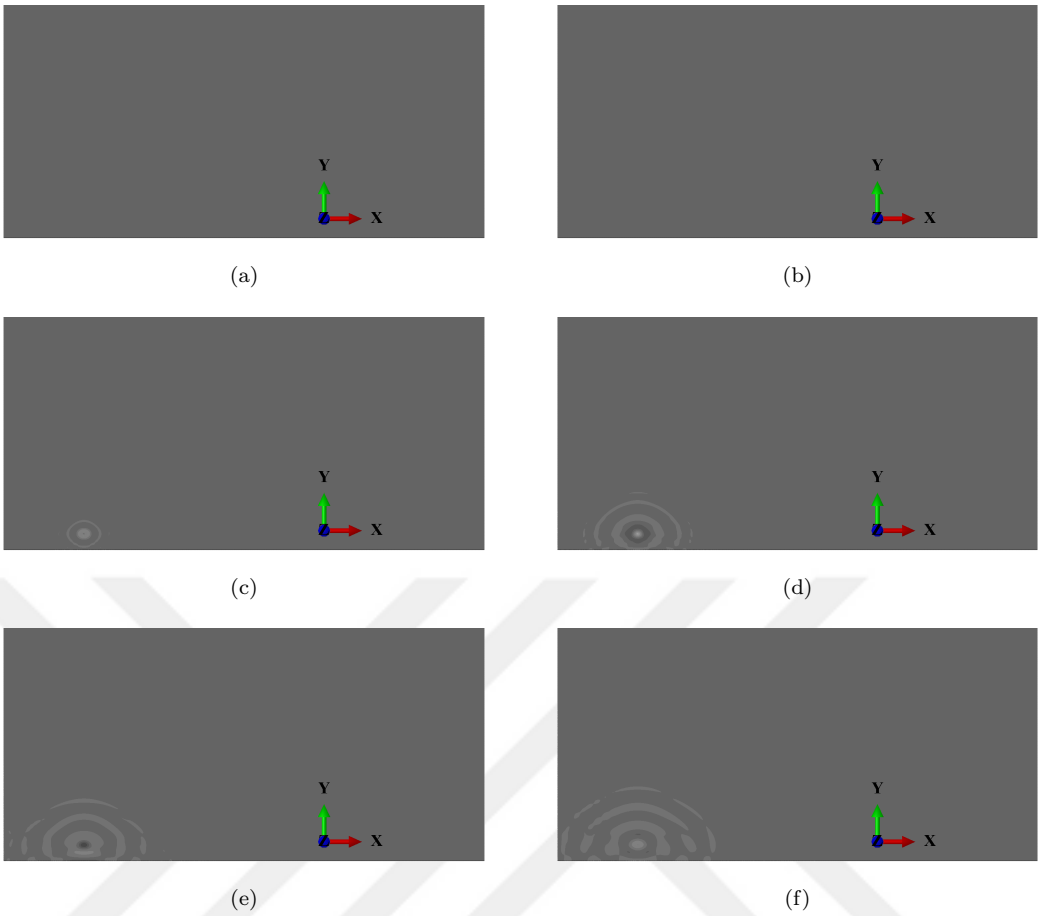

FIGURE 6.9: A0 Lamb wave mode propagating in the LCS captured different times, (a) 3 μs, (b) 42 μs, (c) 84 μs, (d) 126 μs, (e) 168 μs, (f) 210 μs

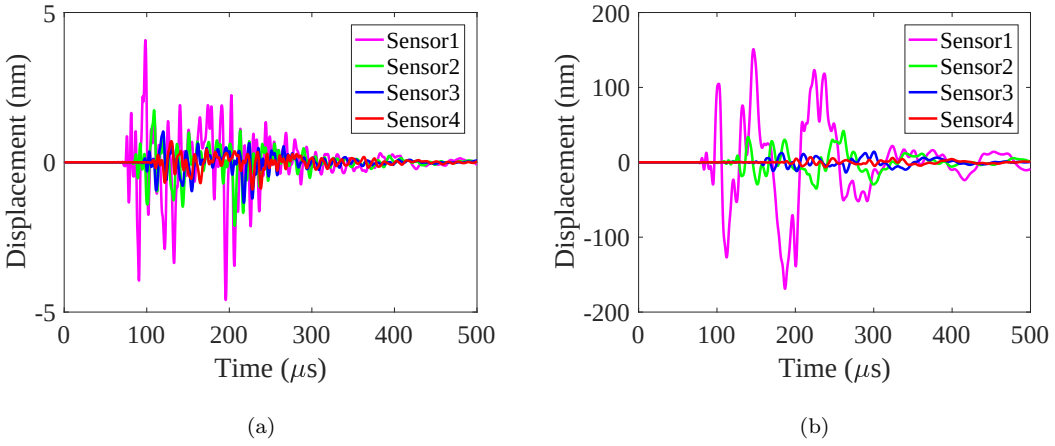

FIGURE 6.10: (a) S0 Lamb wave mode propagating on a plate is captured four sensor points in the x_1 direction, (b) A0 Lamb wave mode propagating on a plate is captured four sensor points in the x_1 direction.

6.5.2 Laminate Stiffness Matrix

To calculate stiffness matrix of LCS, the velocities of Lamb wave are needed to measure in different directions. The velocity measurement of Lamb wave can be performed by using the distance (X) and time of flight (ToF) of the wave (the time that wave needs to travel a certain distance) between the sensor points (Equation 6.39). The distance between the sensor points are pre-defined values but the ToF needs to be calculated by using the Figure 6.10(a) or (b). ToF can be calculated according to the difference in hit times (the time that wave first hit the sensor point) of the wave at certain sensor points.

$$X = V * ToF \tag{6.39}$$

The velocities of two Lamb wave modes ($S0$ and $A0$) in the different directions, through x_1, x_2, and diagonal, are calculated according to Equation 6.39 and tabulated in Table 6.3.

TABLE 6.3: The velocities (m/s) of S0 and A0 modes in different directions.

Directions / Modes	x_1	x_2	Diagonal
S0	4208	2311	2486
A0	1398	1365	–

By using the velocities in Table 6.3 and density of LCS (1682 kg/m^3) with corresponding equations given in Section 6.3, we calculate the components of stiffness matrix and tabulate the results in Table 6.4 under the heading, "Lamb wave". Furthermore, to compare the results obtained by Lamb wave velocity measurement, a second FEA with same LCS is performed. The latter FEA is a numerical simulation of a tensile test of a composite coupon. The dimensions of tensile test coupon are chosen as per the ASTM D3039 standard. All material elastic constants (E_1, E_2, E_3, ν_{12}, ν_{13}, ν_{23}, G_{12}, G_{13}, G_{23}) are calculated by fitting a curve passing through the strain points of 1000 $\mu\epsilon$ and 3000 $\mu\epsilon$ on the corresponding stress-strain curves. Once material elastic constants are calculated, the Equations 6.9-6.17 are used to calculate the components of stiffness matrix. The results are tabulated in Table 6.4 under the heading, "Mechanical". In addition to the results of FEA, the components of stiffness matrix, used (assigned to geometry) in the former and latter FEA, are also is given in the Table 6.4 under the heading, "Assumed". To make a clear comparison, errors (%) between Lamb wave calculated

and "Assumed" components of stiffness matrix are also tabulated in Table 6.4 under the heading, "Error". Although the results are given in Table 6.4 indicates a good correlation between assigned and Lamb wave calculated components of stiffness matrix, only C_{44} shows a considerable deviation. C_{44} corresponds to out of plane shear modulus G_{23}, which is calculated by using the $A0$ mode of lamb wave. A0 mode of Lamb wave, as indicated in Figure 6.2(b), is not stable as much as the S0 mode. The rise of velocity in the low-frequency regime might cause this important error.

TABLE 6.4: Components of stiffness matrix for transversely isotropic laminate.

Components	Assumed	Mechanical	Lamb Wave	Error (%)
C_{11}	30.42	30.42	29.8	2
C_{12}	3.1	3.1	2.9	6.5
C_{13}	3.1	3.1	2.9	6.5
C_{22}	10.2	10.2	9	11.8
C_{23}	2.8	2.8	2.8	0
C_{33}	10.2	10.2	9	11.8
C_{44}	2.5	2.5	3.1	24
C_{55}	3.4	3.4	3.3	3
C_{66}	3.4	3.4	3.3	3

6.5.3 Laminate Elastic Constants

Once the components of stiffness matrix are calculated by Lamb wave propagation, Equations 6.20-6.28 derived by Hashin et al. [77] are used to calculate laminate elastic constants. These laminate elastic constants can be seen in Table 6.5 under the heading, "Lamb Wave-Hashin". In addition to Hashin-Lamb wave calculated elastic constants, those calculated by composite coupon testing with FEA is also tabulated in Table 6.5 under the heading, "Mechanical". Furthermore, to calculate the Poisson's ratios ν_{12} and ν_{13}, the Equation 6.40 is used, once Poisson's ratios ν_{21} and ν_{31} are calculated by using the Equation 6.24.

$$\frac{\nu_{ij}}{E_i} = \frac{\nu_{ji}}{E_j} \tag{6.40}$$

One can see from Table 6.5 that Hashin's [77] approximation works well with the Lamb wave calculated components of stiffness matrix except for the out of

TABLE 6.5: Elastic constants for transversely isotropic laminate.

Constant	Mechanical	Lamb Wave-Hashin	Error (%)
E_1	29	28.35	2.25
E_2	9	8	11.1
E_3	9	8	11.1
ν_{12}	0.23	0.87	250
ν_{13}	0.23	0.87	250
ν_{23}	0.3	0.28	6.6
G_{12}	3.4	3.29	3.3
G_{13}	3.4	3.29	3.3
G_{23}	2.5	3.13	25

plane shear modulus G_{23} and Poisson's ratios ν_{12} and ν_{13}. Even, these Poisson's ratios exceed the limit of a realistic upper bound ($-1 < \nu < 0.5$). The significant error in Hashin's [77] formulation calculated Poisson's ratios ν_{12} and ν_{13} could be attributed to the assumption he made. His assumption involves bounds on strain energy, which also put bounds on the elastic stiffness matrix. These bounds eliminate some components of stiffness matrix in the strain energy calculation and enable us to derive Equations 6.20-6.28. Nevertheless, the Equation 6.41, derived by Kriz et al.[56], led us to recalculate these unrealistic Poisson's ratios.

$$\nu_{12} = \frac{C_{12}C_{22} - C_{23}C_{12}}{C_{22}^2 - C_{23}^2} \tag{6.41}$$

Once, Poisson's ratios $\nu_{12} = \nu_{13}$ are recalculated by using the Equation 6.41, they are found out to be 0.225, which is compare reasonable well with the actual value of 0.23

6.6 Conclusion

This study aims at reaching a non-time-consuming, non-destructive, and inexpensive test method to calculate the components of stiffness matrix and elastic constants of a transversely isotropic LCS. Before initiating an experimental study, we herein numerically simulated a possible test method that relies on the Lamb wave propagation on a transversely isotropic thin-LCS. Numerical simulation enables us to visualize Lamb wave propagation on a LCS, which is impossible with

the experimental method. In the numerical simulation, $S0$ and $A0$ modes of Lamb waves are used due to their non-dispersive nature in a certain frequency interval. The velocities of $S0$ and $A0$ modes of Lamb waves are measured in different directions. These velocities in turn are used in Christoffel's equation to calculate the components of stiffness matrix. Then, components of stiffness matrix calculated by Lamb wave are used in Hashin's equations to calculate elastic constants of the laminate. Following conclusions are obtained in this study:

1. Usage of $S0$ and $A0$ Lamb wave modes are numerically investigated for non-destructive evaluation purposes

2. Lamb wave velocity measurement led us to determine five independent components of stiffness matrix.

3. Although the component C_{44} of stiffness matrix, which is out-of-plane shear modulus G_{23}, indicate a considerable deviation, the other components show reasonably acceptable values.

4. The elastic constants of the laminate are calculated by following an inverse approximation derived by Hashin et al. [77] using component of stiffness matrix calculated by Lamb wave.

5. As a conclusion, this study reveals a quick, non-destructive, and inexpensive test method to calculate elastic stiffness matrix of thin- LCSs by using Lamb wave velocities.

Acknowledgments

The first author gratefully acknowledges the funding provided by The Scientific and Technological Research Council of Turkey (TUBITAK) under the 2214-A International Research Fellowship Program for Ph.D. Students.

Chapter 7

Conclusion

This work has focused on an interdisciplinary research in the field of LCSs, which includes the production of LCSs, coupon processing for mechanical tests with and without FBG sensors, adaptation of some advanced tools such as Acoustic Emission and thermography for mechanical testing, signal processing and signal clustering, and finally the numerical simulation of Lamb waves to determine the stiffness matrix of LCS. In chapters, three, four, and five, all the emphasis is on the reduction of material elastic constants such as Poisson's ratio and shear modulus during mechanical tests. It is shown that reduction in Poisson's ratio is independent of the sensors used. A novel embedded-biaxial FBG sensor to measure Poisson's ratio is developed where both the axial and transversal FBG sensors are on the same fiber optic cable. Possible micro-damage mechanisms that cause the reduction in Poisson's ratio are discussed in details. Acoustic emission is used to monitor micro-cracks along with Poisson's ratio reduction, and it is concluded that transverse cracks and delamination play a key role in the reduction of Poisson's ratio. Damage accumulation behavior of the S-glass and E-glass reinforced LCS under shear loading is investigated by using acoustic emission and thermography. AE signals, generated by micro-damages, are clustered using K-means clustering algorithm with Bray-Curtis dissimilarity function. It is shown that the Bray-Curtis dissimilarity function is robust and accurate for damage-induced AE signal classification. It is demonstrated that the S-glass reinforced LCS indicates less reduction in in-plane shear modulus during the shear test. Furthermore, it has a lower number of damage-induced AE signals, as well as it indicates a lower amount of temperature increase during the shear test.

In addition to these experimental works herein, a numerical simulation study is carried out to simulate Lamb wave propagation with FEM in an arbitrarily transversely isotropic thin-LCS. The numerical simulation shows that the velocity of zero order symmetric and antisymmetric modes can be used to calculate elastic stiffness matrix of transversely isotropic LCSs. Therefore, the elastic stiffness matrix of LCSs can be calculated non-destructively through Lamb waves rather than destructive mechanical tests, which requires expensive testing tools as well as time and labor force commitment.

To sum up, we herein show the reduction in Poisson's ratio and shear modulus for different LCSs (ie., different stacking sequences and fiber reinforcements) is a result of the micro-damage formation during the static tests. This reduction, as a conclusion, has led to the usage of the laminate elastic constant as a damage index with embedded-FBG sensors for LCS. Furthermore, it enables us to understand micro-damage accumulation behavior in LCS. In addition to these, we develop a novel method to non-destructively determine the elastic stiffness matrix of LCSs.

7.1 Future Direction

The outputs of this thesis can provide two valuable results for the future research directions. First of all, this work demonstrates that the reduction in engineering constants is due to the different micro-damage types, not only being limited to transverse cracks as indicated in the literature. In the literature, a number of studies can be found, which take only transverse cracks into account when performing an analytical or numerical study for the reduction in Poisson's ratio or shear modulus. On the other hand, this study implies that it is a necessity to consider delaminations or fiber ruptures when a reduction in Poisson's ratio or shear modulus is modeled. Therefore, a future modeling (numerical simulations or analytical approaches) study, which also considers delaminations or fiber ruptures on the reduction in Poisson's ratio or shear modulus, can be performed. Secondly, this research has initiated an FEA of Lamb Waves to calculate the elastic stiffness matrix of LCSs. A future study (includes both numeric and experiment) can be carried out on the calculation of the viscoelastic-stiffness matrix of LCSs by considering the attenuation of suitable Lamb wave modes.

Bibliography

[1] Matthew J Nicolas, Rani W Sullivan, and W Lance Richards. Large scale applications using fbg sensors: Determination of in-flight loads and shape of a composite aircraft wing. *Aerospace*, 3(3):18, 2016.

[2] HM Ledbetter. Orthotropic elastic stiffnesses of a boron-aluminum composite. *Journal of Applied Physics*, 50(12):8247–8248, 1979.

[3] Christian U Grosse and Lindsay M Linzer. Signal-based ae analysis. *Acoustic emission testing*, pages 53–99, 2008.

[4] Alton L Highsmith and Kenneth L Reifsnider. Stiffness-reduction mechanisms in composite laminates. In *Damage in Composite Materials: Basic Mechanisms, Accumulation, Tolerance, and Characterization*. ASTM International, 1982.

[5] F Gao, L Boniface, SL Ogin, PA Smith, and RP Greaves. Damage accumulation in woven-fabric cfrp laminates under tensile loading: Part 1. observations of damage accumulation. *Composites science and technology*, 59(1):123–136, 1999.

[6] E Vanswijgenhoven, Martine Wevers, and Omer Van der Biest. Transverse cracking and poisson's ratio reduction in cross-ply carbon fibre-reinforced polymers. *Journal of materials science*, 34(22):5513–5517, 1999.

[7] Wim Van Paepegem, Ives De Baere, Ebrahim Lamkanfi, and Joris Degrieck. Poisson's ratio as a sensitive indicator of (fatigue) damage in fibre-reinforced plastics. *Fatigue & Fracture of Engineering Materials & Structures*, 30(4): 269–276, 2007.

[8] Ives De Baere, Wim Van Paepegem, and Joris Degrieck. On the nonlinear evolution of the poisson's ratio under quasi-static loading for a carbon fabric-reinforced thermoplastic. part i: Influence of the transverse strain sensor. *Polymer Testing*, 28(2):196–203, 2009.

[9] Wim Van Paepegem, Ives De Baere, Ebrahim Lamkanfi, and Joris Degrieck. Monitoring quasi-static and cyclic fatigue damage in fibre-reinforced plastics by poissons ratio evolution. *International journal of fatigue*, 32(1):184–196, 2010.

[10] RM Pidaparti and A Vogt. Experimental investigation of poisson's ratio as a damage parameter for bone fatigue. *Journal of Biomedical Materials Research Part A*, 59(2):282–287, 2002.

[11] PA Smith and JR Wood. Poisson's ratio as a damage parameter in the static tensile loading of simple crossply laminates. *Composites Science and Technology*, 38(1):85–93, 1990.

[12] Mehmet Yildiz, Nazli G Ozdemir, Gokhan Bektas, Casey J Keulen, Talha Boz, Ege F Sengun, Cem Ozturk, Yusuf Z Menceloglu, and Afzal Suleman. An experimental study on the process monitoring of resin transfer molded composite structures using fiber optic sensors. *Journal of Manufacturing Science and Engineering*, 134(4):044502, 2012.

[13] Casey J Keulen, Erdem Akay, Fatih F Melemez, Esat S Kocaman, Ataman Deniz, Cagatay Yilmaz, Talha Boz, Mehmet Yildiz, Halit S Turkmen, and Afzal Suleman. Prediction of fatigue response of composite structures by monitoring the strain energy release rate with embedded fiber bragg gratings. *Journal of Intelligent Material Systems and Structures*, 27(1):17–27, 2016.

[14] Esat S Kocaman, Casey J Keulen, Erdem Akay, Mehmet Yildiz, Halit S Turkmen, and Afzal Suleman. An experimental study on the effect of length and orientation of embedded fbg sensors on the signal properties under fatigue loading. *Science and Engineering of Composite Materials*, 23(6):711–719, 2016.

[15] Casey J Keulen, Mehmet Yildiz, and Afzal Suleman. Multiplexed fbg and etched fiber sensors for process and health monitoring of 2-&3-d rtm components. *Journal of Reinforced Plastics and Composites*, 30(12):1055–1064, 2011.

[16] M Kempf, O Skrabala, and V Altstädt. Acoustic emission analysis for characterisation of damage mechanisms in fibre reinforced thermosetting polyurethane and epoxy. *Composites Part B: Engineering*, 56:477–483, 2014.

[17] R Gutkin, CJ Green, S Vangrattanachai, ST Pinho, P Robinson, and PT Curtis. On acoustic emission for failure investigation in cfrp: Pattern recognition and peak frequency analyses. *Mechanical Systems and Signal Processing*, 25 (4):1393–1407, 2011.

[18] John C Brewer and Paul A Lagace. Quadratic stress criterion for initiation of delamination. *Journal of composite materials*, 22(12):1141–1155, 1988.

[19] Th Lorriot, G Marion, R Harry, and H Wargnier. Onset of free-edge delamination in composite laminates under tensile loading. *Composites Part B: Engineering*, 34(5):459–471, 2003.

[20] Nobuhide Uda and Kazuo Kunoo. Edge delamination of composite laminates under low cycle fatigue. In *Proc. of 12th Int. Conf. on Composite Materials, paper312*, 1999.

[21] CR Ramirez-Jimenez, N Papadakis, N Reynolds, TH Gan, P Purnell, and M Pharaoh. Identification of failure modes in glass/polypropylene composites by means of the primary frequency content of the acoustic emission event. *Composites Science and Technology*, 64(12):1819–1827, 2004.

[22] C Barile, C Casavola, G Pappalettera, and C Pappalettere. Hybrid thermography and acoustic emission testing of fatigue crack propagation in aluminum samples. In *Fracture, Fatigue, Failure, and Damage Evolution, Volume 5*, pages 247–252. Springer, 2015.

[23] VR Skalskii, EM Stankevich, and Yu Ya Matviiv. A study of the features of the macrofracturing of composite materials. *Russian Journal of Nondestructive Testing*, 49(10):562–571, 2013.

[24] Christopher Baker, Gregory N Morscher, Vijay V Pujar, and Joseph R Lemanski. Transverse cracking in carbon fiber reinforced polymer composites: Modal acoustic emission and peak frequency analysis. *Composites Science and Technology*, 116:26–32, 2015.

[25] MGR Sause, T Müller, A Horoschenkoff, and S Horn. Quantification of failure mechanisms in mode-i loading of fiber reinforced plastics utilizing acoustic emission analysis. *Composites science and technology*, 72(2):167–174, 2012.

[26] C Yilmaz, C Akalin, Esat Selim Kocaman, A Suleman, and M Yildiz. Monitoring poissons ratio of glass fiber reinforced composites as damage index using biaxial fiber bragg grating sensors. *Polymer Testing*, 53:98–107, 2016.

[27] NN Hsu. Characterization and calibration of acoustic emission sensors. *Mater. Eval.*, 39:60–68, 1981.

[28] O Rubenis, E Spārniņš, J Andersons, and Roberts Joffe. The effect of crack spacing distribution on stiffness reduction of cross-ply laminates. *Applied Composite Materials*, 14(1):59–66, 2007.

[29] J Lindemann and W Becker. The tendency for free-edge delamination in laminates and its minimization. *Composites Science and Technology*, 62(2): 233–242, 2002.

[30] Pongsak Nimdum and Jacques Renard. Non local approach for prediction of delamination onset. In *18th international conference of composite materials*, pages 6–p, 2011.

[31] Erdem Akay, Cagatay Yilmaz, Esat S Kocaman, Halit S Turkmen, and Mehmet Yildiz. Monitoring poissons ratio degradation of frp composites under fatigue loading using biaxially embedded fbg sensors. *Materials*, 9(9):781, 2016.

[32] KH Amara, A Tounsi, and A Benzair. Transverse cracking and elastic properties reduction in hygrothermal aged cross-ply laminates. *Materials Science and Engineering: A*, 396(1):369–375, 2005.

[33] L Niklas Melin and Jonas M Neumeister. Measuring constitutive shear behavior of orthotropic composites and evaluation of the modified iosipescu test. *Composite structures*, 76(1):106–115, 2006.

[34] BW Tew, EM Odom, and JD Teel. Composite specimen bearing failure reduction in iosipescu shear tests. *Experimental mechanics*, 41(3):218–224, 2001.

[35] Fabrice Pierron and Alain Vautrin. Measurement of the in-plane shear strengths of unidirectional composites with the iosipescu test. *Composites Science and technology*, 57(12):1653–1660, 1998.

[36] G Odegard and M Kumosa. Determination of shear strength of unidirectional composite materials with the iosipescu and 10 off-axis shear tests. *Composites Science and Technology*, 60(16):2917–2943, 2000.

[37] L Han and MR Piggott. Tension–compression and iosipescu tests on laminates. *Composites Part A: Applied Science and Manufacturing*, 33(1):35–42, 2002.

[38] Fabrice Pierron and Alain Vautrin. Measurement of the in-plane shear strengths of unidirectional composites with the iosipescu test. *Composites Science and technology*, 57(12):1653–1660, 1998.

[39] YT Sun, DQ Shi, XG Yang, CH Mi, J Feng, and YG Jiang. Stress state analysis of iosipescu shear specimens for aerogel composite with different properties in tension and compression. *Procedia Engineering*, 67:517–524, 2013.

[40] M Salavatian and LV Smith. The effect of transverse damage on the shear response of fiber reinforced laminates. *Composites Science and Technology*, 95:44–49, 2014.

[41] Mohammedmahdi Salavatian and Lloyd Smith. An improved analytical model for shear modulus of fiber reinforced laminates with damage. *Composites Science and Technology*, 105:9–14, 2014.

[42] Li Li, Stepan V Lomov, and Xiong Yan. Correlation of acoustic emission with optically observed damage in a glass/epoxy woven laminate under tensile loading. *Composite structures*, 123:45–53, 2015.

[43] Li Li, Stepan V Lomov, Xiong Yan, and Valter Carvelli. Cluster analysis of acoustic emission signals for 2d and 3d woven glass/epoxy composites. *Composite Structures*, 116:286–299, 2014.

[44] Valter Carvelli, Alessandro D'Ettorre, and Stepan V Lomov. Acoustic emission and damage mode correlation in textile reinforced pps composites. *Composite Structures*, 163:399–409, 2017.

[45] M Genest, M Martinez, N Mrad, G Renaud, and A Fahr. Pulsed thermography for non-destructive evaluation and damage growth monitoring of bonded repairs. *Composite Structures*, 88(1):112–120, 2009.

[46] Chidong Liu, Laifei Cheng, Xingang Luan, Bin Li, and Jun Zhou. Damage evolution and real-time non-destructive evaluation of 2d carbon-fiber/sic-matrix composites under fatigue loading. *Materials Letters*, 62(24):3922–3924, 2008.

[47] M Naderi, A Kahirdeh, and MM Khonsari. Dissipated thermal energy and damage evolution of glass/epoxy using infrared thermography and acoustic emission. *Composites Part B: Engineering*, 43(3):1613–1620, 2012.

[48] John Montesano, Zouheir Fawaz, and Habiba Bougherara. Non-destructive assessment of the fatigue strength and damage progression of satin woven fiber reinforced polymer matrix composites. *Composites Part B: Engineering*, 71: 122–130, 2015.

[49] V Crupi. An unifying approach to assess the structural strength. *International Journal of Fatigue*, 30(7):1150–1159, 2008.

[50] G Fargione, A Geraci, G La Rosa, and A Risitano. Rapid determination of the fatigue curve by the thermographic method. *International Journal of Fatigue*, 24(1):11–19, 2002.

[51] Erich Schubert, Alexander Koos, Tobias Emrich, Andreas Züfle, Klaus Arthur Schmid, and Arthur Zimek. A framework for clustering uncertain data. *Proceedings of the VLDB Endowment*, 8(12):1976–1979, 2015.

[52] Nathalie Godin, Stéphane Huguet, Roger Gaertner, and L Salmon. Clustering of acoustic emission signals collected during tensile tests on unidirectional glass/polyester composite using supervised and unsupervised classifiers. *Ndt & E International*, 37(4):253–264, 2004.

[53] C Yilmaz and M Yildiz. A study on correlating reduction in poisson's ratio with transverse crack and delamination through acoustic emission signals. *Polymer Testing*, 63:47–53, 2017.

[54] Esat Selim Kocaman, Erdem Akay, Cagatay Yilmaz, Halit Suleyman Turkmen, Ibrahim Burc Misirlioglu, Afzal Suleman, and Mehmet Yildiz. Monitoring the damage state of fiber reinforced composites using an fbg network for failure prediction. *Materials*, 10(1):32, 2017.

[55] Robert L Hausrath and Anthony V Longobardo. High-strength glass fibers and markets. In *Fiberglass and Glass Technology*, pages 197–225. Springer, 2010.

[56] RD Kriz and WW Stinchcomb. Elastic moduli of transversely isotropic graphite fibers and their composites. *Experimental Mechanics*, 19(2):41–49, 1979.

[57] PWA Stijnman. Determination of the elastic constants of some composites by using ultrasonic velocity measurements. *Composites*, 26(8):597–604, 1995.

[58] AA Karabutov, IM Kershtein, IM Pelivanov, and NB Podymova. Laser ultrasonic investigation of the elastic properties of unidirectional graphite-epoxy composites. *Mechanics of composite materials*, 34(6):575–582, 1998.

[59] Philippe Marguères and Fodil Meraghni. Damage induced anisotropy and stiffness reduction evaluation in composite materials using ultrasonic wave transmission. *Composites Part A: Applied Science and Manufacturing*, 45: 134–144, 2013.

[60] Tomáš Goldmann, Hanuš Seiner, and Michal Landa. Determination of elastic coefficients of bone and composite materials by acoustic immersion technique. *Technology and Health Care*, 14(4, 5):219–232, 2006.

[61] Subhendu Datta, Hassel Ledbetter, and Tetsuyuki Kyono. Graphite-fiber elastic constants: determination from ultrasonic measurements on composite materials. In *Review of Progress in Quantitative Nondestructive Evaluation*, pages 1481–1488. Springer, 1989.

[62] Sea-Fue Wang, Yung-Fu Hsu, Jui-Chen Pu, James C Sung, and LG Hwa. Determination of acoustic wave velocities and elastic properties for diamond and other hard materials. *Materials Chemistry and Physics*, 85(2):432–437, 2004.

[63] SP Dodd, M Cankurtaran, and B James. Ultrasonic determination of the elastic and nonlinear acoustic properties of transition-metal carbide ceramics: Tic and tac. *Journal of materials science*, 38(6):1107–1115, 2003.

[64] Kalyan Kumar Phani and Dipayan Sanyal. A new approach for estimation of poissons ratio of porous powder compacts. *Journal of materials science*, 42 (19):8120–8125, 2007.

[65] Ajay Raghavan and Carlos ES Cesnik. Review of guided-wave structural health monitoring. *Shock and Vibration Digest*, 39(2):91–116, 2007.

[66] C Ramadas. Three-dimensional modeling of lamb wave attenuation due to material and geometry in composite laminates. *Journal of Reinforced Plastics and Composites*, 33(9):824–835, 2014.

[67] Dulip Samaratunga and Ratneshwar Jha. Simulation. In *2012 SIMULIA Community Conference*, 2012.

[68] Ratneshwar Jha, Inho Kim, and Dulip Widana-Gamage. Investigation of incident lamb wave parameters on detection of composite delamination. In *ASME Conference Proceedings*, pages 675–683, 2010.

[69] Rakesh Kumar Singh and Ramadas Chennamsetti. Propagation of ao mode through the front edge of a delamination: Numerical and experimental studies. *International journal of precision engineering and manufacturing*, 15(8): 1639–1645, 2014.

[70] Xiang Wan, Qing Zhang, Guanghua Xu, and Peter W Tse. Numerical simulation of nonlinear lamb waves used in a thin plate for detecting buried micro-cracks. *Sensors*, 14(5):8528–8546, 2014.

[71] A De Luca, Z Sharif-Khodaei, MH Aliabadi, and F Caputo. Numerical simulation of the lamb wave propagation in impacted cfrp laminate. *Procedia Engineering*, 167:109–115, 2016.

[72] Seyed Mohammad Hossein Hosseini, Abdolreza Kharaghani, Christoph Kirsch, and Ulrich Gabbert. Numerical simulation of lamb wave propagation in metallic foam sandwich structures: a parametric study. *Composite Structures*, 97:387–400, 2013.

[73] Valentina Agostini, Pier Paolo Delsanto, Ivan Genesio, and Dimitri Olivero. Simulation of lamb wave propagation for the characterization of complex structures. *IEEE transactions on ultrasonics, ferroelectrics, and frequency control*, 50(4):441–448, 2003.

[74] C Ramadas, Krishnan Balasubramaniam, Avinash Hood, Makarand Joshi, and CV Krishnamurthy. Modelling of attenuation of lamb waves using rayleigh damping: Numerical and experimental studies. *Composite Structures*, 93(8):2020–2025, 2011.

[75] Vlastislav Cerveny. *Seismic ray theory*. Cambridge university press, 2005.

[76] Tianyou Fan. *Mathematical theory of elasticity of quasicrystals and its applications*. Springer, 2011.

[77] Zvi Hashin and B Walter Rosen. The elastic moduli of fiber-reinforced materials. *Journal of applied mechanics*, 31(2):223–232, 1964.

[78] B Tang and EG Henneke. Long wavelength approximation for lamb wave characterization of composite laminates. *Research in Nondestructive Evaluation*, 1(1):51–64, 1989.

[79] HM Ledbetter and DT Read. Orthorhombic elastic constants of an nbti/cu composite superconductor. *Journal of Applied Physics*, 48(5):1874–1879, 1977.